Interaction between the mitral and aortic heart valve : an experimental and computational study

Interaction between the mitral and aortic heart valve

an experimental and computational study

CIP-DATA LIBRARY TECHNISCHE UNIVERSITEIT EINDHOVEN

Stijnen, Johannes M.A.

Interaction between the mitral and aortic heart valve: an experimental and computational study. / by Johannes M.A. Stijnen. – Eindhoven : Technische Universiteit Eindhoven, 2004.
Proefschrift. – ISBN 90-386-2566-9
NUR 954
Subject headings: heart valve prostheses / valve motion / ventricular flow / mitral valve orientation / fluid-structure interaction / interaction between mitral and aortic valves / fictitious domain method / finite element method / cardiovascular bloodflow / particle image velocimetry

Printed by Universiteitsdrukkerij TU Eindhoven, Eindhoven, The Netherlands.

The publication of this thesis was financially supported by Medtronic.

Interaction between the mitral and aortic heart valve

an experimental and computational study

PROEFSCHRIFT

ter verkrijging van de graad van doctor
aan de Technische Universiteit Eindhoven,
op gezag van de Rector Magnificus, prof.dr. R.A. van Santen,
voor een commissie aangewezen door het College voor Promoties
in het openbaar te verdedigen op
donderdag 8 juli 2004 om 16.00 uur

door

Johannes Martinus Anna Stijnen

geboren te Geleen

Dit proefschrift is goedgekeurd door de promotoren:

prof.dr.ir. F.N. van de Vosse
en
prof.dr.ir. F.P.T. Baaijens

Copromotor:
dr.ir. P.H.M. Bovendeerd

Contents

Summary

In cardiac surgery, a failing native heart valve can be replaced by a mechanical prosthesis, the design and orientation of implantation of which can be chosen deliberately by the surgeon. Due to the geometrical differences, the flow downstream a prosthetic valve could differ significantly from that downstream the native valve. Besides geometrical influences, also the orientation in which a non axi-symmetrical valve is implanted in mitral position largely influences the ventricular flow patterns downstream. It is hypothesized that the left ventricular flow field can influence the timing of opening and closing of the aortic valve. In this way, the efficiency of the heart as a pump would depend partly on the geometry and orientation of implantation of a prosthetic mitral valve. Understanding this relation from basic physical principles would contribute to optimization of the choice of valve geometry and alignment in a specific patient.

A computational model that describes the relation between mitral valve orientation and the efficiency of the heart as a pump can be of major importance to predict a preferred valve orientation pre-operatively and patient specifically. The results of such a computational model must be assessed in a quantitative manner, by comparison to experimental measurements in equal circumstances. An experimental setup featuring a deforming rubber model ventricle was designed in which velocity fields were obtained using digital particle image velocimetry (DPIV). The geometry of the rubber ventricle model is based on MRI images of the heart of a healthy volunteer. In the setup, both the mitral and aortic orifices were equipped with Carbomedics bi-leaflet valves, and flow fields were obtained for two mutually perpendicular orientations of the mitral valve. A computational model is developed of the experimental setup, where simplifications were made to the geometry of the ventricular cavity and the mitral valve, and the timing of opening and closing of the valves was prescribed. The valve leaflets are represented by regions of increased viscosity. For both valve orientations, the flow fields predicted by the computational method are comparable to the experimental data. It is shown by both methods that the orientation of the mitral valve largely influences the global interaction of the valve with the ventricular flow patterns. However, a quantitative comparison between computations and experimental results shows that the measured velocities differ significantly from the computationally predicted velocities. These differences are attributed to simplified description of the geometry of the valves and the ventricular cavity in the computational model.

In light of the complex nature of the three dimensional flow in the ventricular cavity, a two dimensional setting was chosen to study the exact interaction between valve motion and local fluid flow. Valve motion and fluid flow was studied in a model of a stiff valve. The fluid velocity fields and the valve motion predicted by the computational method match with DPIV measurements in an *in-vitro* setup. It is concluded that the fictitious domain method used to model the fluid-structure interaction is a suitable method for describing the dynamic response of stiff heart valves. Furthermore, it is concluded that the regurgitant volume that is necessary to close the valve, is depending on the stroke volume and the frequency of the flow pulses applied.

Since in the left ventricle the aortic and mitral valve are located side by side, an interdependence of the dynamic behavior of the valves is expected. To study this interdependence, the model previously used to study the fluid-structure interaction of a single valve leaflet is extended to accommodate a second valve. Thus, the fictitious domain method was applied to a two dimensional finite element model of a ventricle with a mitral and an aortic valve. Results show that the sum of the regurgitant volumes changes for variations in the flow conditions, realized by changing stroke volume or heart rate. Cycle-to-cycle variations in valve motion and regurgitant volumes were found to exist, depending on the characteristics of the flow applied, in terms of the Reynolds and Strouhal number. This finding is of major importance to studies involving bi-valve systems and to medical applications like heart valve replacements; investigation of only one cycle is no longer adequate. Using the same computational model, a change in rotation direction of the mitral valve was shown to cause significantly different ventricular flow patters under the same flow conditions. The pump efficiency of the ventricle and the cycle-to-cycle variation of valve motion and regurgitant volumes were found to depend on valve orientation.

Based on simulations using the two dimensional ventricle model with two valves the hypothesis that the efficiency of the ventricle as a pump is depending on the orientation of the mitral valve is considered valid. Application of the method used to a three dimensional model ventricle with moving heart valves can lead to realistic predictions of actual loss of stroke volume due to valve regurgitation, for several orientations of both mitral and aortic valve prostheses as well as give directions for improvement of prosthetic valve design.

In conclusion, the three dimensional ventricular flow patterns were found to be largely dependent on the orientation of the mitral valve. The fictitious domain method was found a suitable method for predicting the dynamic response of stiff valves. An interdependence between aortic and mitral valve motion was found to exist and depend both on the applied flow and mitral valve orientation. This interdependence is reflected in the pump efficiency of the model ventricle.

Samenvatting

In de hartchirurgie heeft de chirurg, bij het vervangen van een natuurlijke hartklep door een mechanische hartklep, de keuze uit verschillende klepontwerpen en kan een prothese in elke gewenste oriëntatie in de klepopening vastgezet worden. Door het verschil in geometrie zou bij een mechanische klep in mitraal positie de stroming in de linkerventrikel aanzienlijk anders kunnen zijn ten opzichte van de stroming achter de natuurlijke klep. Afgezien van de geometrie van de klepprothese geldt voor elke niet axi-symmetrische prothese dat het stromingsveld dat in de ventrikel ontstaat sterk afhankelijk is van de oriëntatie waarin de mitraalklep prothese bevestigd wordt. De hypothese, die in dit werk gesteld wordt, is dat het stromingsveld in de linkerventrikel van invloed kan zijn op de timing van openen en sluiten van de aortaklep waardoor ook het terugstroomvolume, dat nodig is om de klep te sluiten, van beide kleppen anders zal zijn. Hierdoor zou de efficiëntie waarmee het hart bloed door het lichaam pompt kunnen afhangen van de oriëntatie waarin een mechanische hartklep prothese geïmplanteerd wordt. Het is interessant voor de hartchirurgie om dit fenomeen te bestuderen omdat een beslissing omtrent de oriëntatie van een te implanteren hartklep dan op basis van begrepen fysica genomen kan worden.

Een numeriek model, dat de relatie beschrijft tussen kleporiëntatie en de efficiëntie waarmee het hart bloed pompt, zou van groot belang kunnen zijn bij het patiëntspecifiek en pre-operatief voorspellen van een voorkeursoriëntatie van een te implanteren klepprothese. De kwaliteit van de voorspelling van zo'n numeriek model moet echter wel getoetst zijn aan de hand van metingen in een vergelijkbare situatie. Daartoe is een experimentele opstelling ontworpen waarin snelheidsvelden gemeten zijn in een gestyleerd rubberen model van een linker hartkamer. De gekozen geometrie van het hartkamermodel is gebaseerd op MRI beelden van het hart van een gezond proefpersoon. In het experimentele model zijn zogenaamde bi-leaflet klepprothesen gebruikt waarbij twee onderling loodrechte oriëntaties van de mitralisklep bestudeerd zijn. Een eerste stap in de richting van een numeriek model om de pompfunctie van de linker hartkamer te voorspellen bij een gegeven mitraliskleporiëntatie is gebaseerd op het experimentele model, waarbij vereenvoudigingen gemaakt zijn in de geometrie van de hartkamer en de mitralisklep, en de dynamiek van de kleppen wordt voorgeschreven. De stromingspatronen die het numerieke model voorspelt zijn vergelijkbaar met de metingen uit de experimenten, voor beide oriëntaties van de mitralisklep. Ook wordt aangetoond dat de oriëntatie van de mitralisklep grote invloed heeft op de globale interactie met de stroming in de ventrikel. Echter, uit een kwan-

titatief vergelijk tussen beide modellen blijkt dat de snelheden voorspeld door het numeriek model verschillen van de gemeten snelheden in de experimenten. De verschillen in de resultaten kunnen worden toegewezen aan de geometrische verschillen tussen de modellen.

Gezien de complexe aard van de drie dimensionale stroming in het hartkamermodel is het moeilijk om de exacte interactie tussen klepbeweging en vloeistofstroming te bestuderen aan de hand van dit model. Daarom is gekozen voor een studie van deze interactie in een twee dimensionaal model van een starre hartklep. Er wordt gekeken naar de geschiktheid van de fictitious domain methode voor het voorspellen van de dynamica van een starre klep. Een range van verschillende pulsatiele stromingscondities wordt opgelegd, welke gevariëerd zijn in termen van het Reynoldsgetal (slagvolume) en het Strouhalgetal (hartslagfrequentie) om de gevoeligheid van de methode te bestuderen. De berekende snelheidsvelden rondom de klep komen overeen met PIV-metingen in een experimentele opstelling, en de klepdynamica wordt door het numeriek model goed voorspeld. Op basis van deze studie wordt geconcludeerd dat de ontwikkelde methode geschikt is voor het beschrijven van de dynamica van een starre hartklep. Tevens blijkt dat het terugstoomvolume in het klepmodel, dat nodig is om de klep te sluiten, afhankelijk was van de variatie in de aangeboden stroming, in termen van het Reynolds en Strouhal getal.

Aangezien het terugstroomvolume van een starre klep beïnvloed wordt door de aangeboden stroming, is het van belang om de interactie tussen twee kleppen in een hartkamer te bestuderen onder verschillende stromingscondities. Hiertoe is dezelfde fictitious domain methode gebruikt in combinatie met een twee dimensionaal eindige elementen model van een hartkamer met een mitralis- en een aortaklep. Uit de simulaties met dit model blijkt dat de som van de terugstroomvolumes van beide kleppen verandert bij variaties in de stromingscondities. Ook werd gevonden dat het lekkagevolume en de beweging van beide kleppen variëren in opeenvolgende slagen, en dat deze variaties afhankelijk zijn is van de aangeboden stroming, gekarakteriseerd in termen van het Reynolds en het Strouhal getal. Dit is van groot belang voor experimentele en numerieke studies naar twee-klep systemen, maar ook voor medische toepassingen zoals hartklep implantaties; het bestuderen van een enkele cyclus is niet afdoende om conclusies op te baseren.

Vervolgens is aangetoond dat het veranderen van de draairichting van de mitralisklep significant verschillende stromingspatronen in de hartkamer oplevert onder gelijke stromingscondities. Ook de efficiëntie van het rondpompen van vloeistof en de variatie in de terugstroomvolumes bleken afhankelijk te zijn van de oriëntatie van de mitralisklep.

De hypothese dat de efficiëntie waarmee het hart bloed kan pompen afhangt van de onderlinge oriëntatie van de hartkleppen kan op basis van het twee dimensionale hartkamermodel met twee kleppen worden bevestigd. Toepassen van de gebruikte methodiek op een drie dimensionale versie van een hartkamer met bewegende kleppen zal realistische voorspellingen kunnen opleveren voor het daadwerkelijk verlies in slagvolume voor verschillende oriëntaties van zowel mitraliskleppen als aortakleppen, en aanwijzigingen voor verbeteringen aan het ontwerp van klepprothesen.

Chapter 1

General Introduction

1.1 Introduction

The human heart is a double pump enabling the pulmonary and systemic circulation of blood. Each pump consists of a receiving and a pumping chamber, called atrium and ventricle, respectively. To ensure the unidirectional flow through the heart and consequently through the body, each ventricle is equipped with two valves, one at the inlet and one at the outlet, as shown in Figure 1.1. The inlet valves are the bicuspid valve at the right side and the mitral valve at the left side. The outlet valves are the pulmonary valve and the aortic valve, respectively.

The cardiac cycle can be divided in four parts; the diastolic phase, the isovolumetric contraction phase, the systolic phase and the isovolumetric relaxation phase. During the systolic phase, blood from the body and lungs accumulates in the left and right atria. During isovolumetric relaxation, the cardiac muscle relaxes causing the ventricular pressures to drop below the atrial pressures. At that instant the diastolic phase begins, the bicuspid and mitral valves open and blood flows into the right and left ventricles, respectively. At the end of the diastolic phase the atria contract, squeezing some extra blood into the ventricles. After that, the ventricular muscle starts to contract and the mitral and bicuspid valves close. During the isovolumetric contraction phase, the valves are closed and the ventricular contraction causes the pressure to rise above the pulmonary and aortic pressures. Then the systolic phase starts, during which the ventricular blood volume is ejected into the pulmonary and aortic arteries. The role of the heart valves is to allow blood flow in the desired direction with a minimal resistance, while obstructing blood flow in an undesired direction with as little back flow as possible.

1.2 The natural valves

The native valves of the heart normally consist of three leaflets, except for the mitral valve which has two leaflets. As shown in Figure 1.1, the valves are all attached

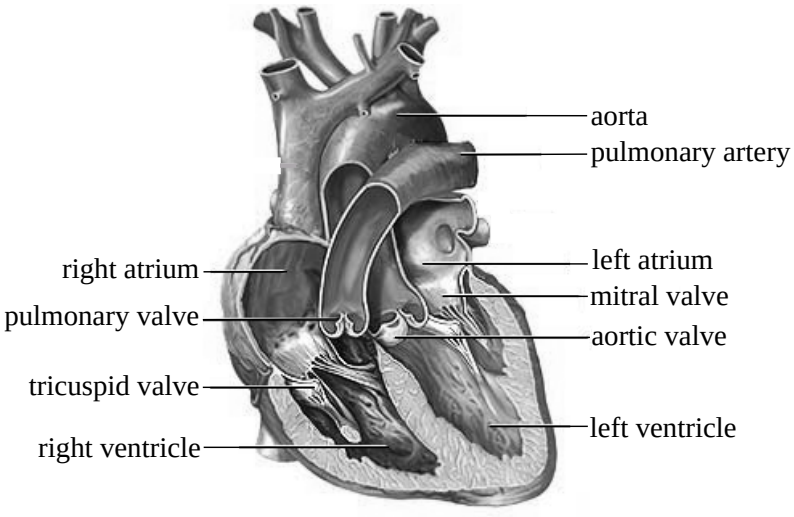

Figure 1.1: Anatomy of the heart.

to the circumference of the valve orifices, through which blood enters or leaves the ventricular chambers. When blood starts to flow through the valves, their low bending stiffness allows them to be pushed aside without much resistance. Due to the high pressure in the ejection phase the compliant wall of the pulmonary and aortic arteries dilates, which prevents the valve leaflets from fluttering and also increases the valve orifice.

The aortic and pulmonary arteries are equipped with cavities downstream each leaflet of their respective valves, called sinusses of Valsalva. As the blood that is expelled from the ventricles decelerates at the end of the ejection phase, vortices develop in the sinus cavities which helps in closing the valve leaflets. The closed aortic and pulmonary valves have enough structural stiffness to withstand the load applied by the blood pressure; the valve leaflets have a relatively high in-plane stiffness and the pressure loading is carried in that direction. The mitral and tricuspid valve need some extra help to carry the pressure load in closed state. To this end they are equipped with ”chordae tendinae”; strings that are attached to the tip of the valve leaflets which are held in place by the papillary muscles that stem from the ventricular wall. In this way the mitral and tricuspid valves are kept from protruding into the atria during the ejection phase, which allows them to prevent blood flow into the atria.

1.3 Valvular disease

Valvular disease can cause damage to valve leaflets, leading to a stenotic or an insufficient valve. In the first case, the motion of the valve leaflet is limited causing an obstruction to forward flow. In the second case the valve will not be able to close completely which results in back flow, i.e. leakage or regurgitation. In 2001, of all valve diseases in the left ventricle, aortic stenosis was the most frequent with 43.1%, followed by mitral regurgitation (31.5%) (Iung *et al.*, 2003). Aortic regurgitation and mitral stenosis were less frequent (13.3% and 12.1% respectively). When the valvular disease becomes significant, the condition of the patient may deteriorate to an extent that valve replacement is desired. Worldwide, approximately 250,000 patients a year undergo heart valve replacements (Butany *et al.*, 2003). This huge number indicates that optimization of prosthetic heart valve design, assessment of valve function and surgical planning with respect to valve orientation is of great importance.

1.4 Valve prostheses

For replacement of a diseased native valve with a prosthesis, two types of artificial heart valves are mainly used today: mechanical valves and biological valves. A biological prosthesis is generally made of porcine aortic valve tissue or bovine pericardial tissue, while a mechanical valve prosthesis is usually made of carbon with a pyrolitic coating. The haemodynamic performance of a bio-prosthetic valve is generally much better than that of its mechanical counterpart. The shape, material properties, flow and trans-valvular pressure gradients closely match those of the native valve. However, during the life of a bio-prosthesis, gradual degeneration will take place and as a result re-operation will be necessary. The average life time of a bio-prosthetic valve is between 10 and 15 years, whereas a mechanical prosthesis is expected not to fail. Although mechanical prostheses are generally very durable, they are prone to thrombus deposition and subsequent complications resulting from emboli. Therefore, application of a mechanical valve prosthesis in patients calls for life-long anti-coagulation medication. For this reason, bio-prostheses are mainly used in elderly patients or patients that can not adhere to the anti-coagulation therapy, such as women who may wish to bear children. Worldwide, over 55% of the implanted prosthetic valves are mechanical, while almost 45% are biological (Butany *et al.*, 2003).

The first implanted mechanical valve prosthesis was a caged ball (such as the Starr-Edwards valve in Figure 1.2 (a)), engineered by Dr. Charles Hufnagel in 1952 (Hufnagel *et al.*, 1954). The strength of this design was the low leakage of the closed valve. In opened state, the occluder ball was in the main flow area, causing high shear stresses and high trans-valvular pressure gradients. An other disadvantage was its size, because of which it could not always be used.

In order to improve on this prosthesis, many different shapes were designed and some of those designs were approved for implantation. One of the approved designs was the tilting disc, such as the Bjork-Shiley prosthesis (Figure 1.2(b)). The dimensions of the prosthesis were greatly reduced with respect to the caged ball design,

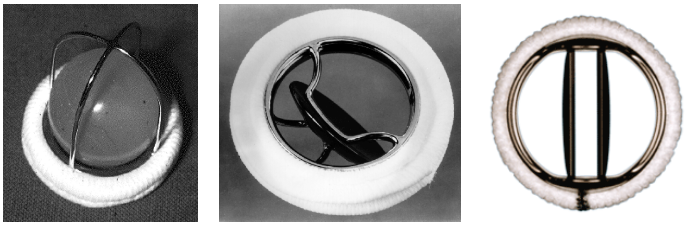

(a) (b) (c)

Figure 1.2: Three types of mechanical valves, increasingly in use from left to right: caged ball (Starr-Edwards), mono-leaflet tilting disc (Bjork-Shiley) and bi-leaflet valve (St. Jude Medical).

and as such it was applicable in any position. Furthermore, as the disc tilted aside, it would move out of the main flow, thus minimizing the flow disturbance. The first bi-leaflet valve was introduced by St. Jude Medical Inc. in 1978 (Figure 1.2(c)). This design consists of two semicircular carbon discs, which in the opened position are intended to provide minimum disturbance to flow. The three types of prostheses described above are currently in clinical use. In the UK, in the year 2000 91.8% of the implanted mechanical valves were bi-leaflet, 6.5% were single leaflet and 1.7% were caged ball out of a total of 4049 implants (Murday *et al.*, 2003).

1.5 Assessment of valve function

The haemodynamic behavior of the native heart valves is not matched by that of mechanical valve prostheses. In attempts to improve the functionality of mechanical valve prostheses, many studies have addressed different aspects related to characterizing valve performance, such as back flow, trans valvular pressure gradients for the opened valve, valve surface area, shear rate at the leaflet surface but also the (disturbance of) flow patterns developing downstream the prostheses (see Chandran *et al.* (1989)). In more detail, flow patterns and thrombus formation in the hinges of the valve leaflets have become areas of interest. As a result several designs are adopted, where each design is superior to another design in one or more of the areas mentioned above.

1.6 Impact of valve design and orientation on ventricular function

Not only the design of the valve determines its effectiveness but also the alignment of its implantation with respect to the anatomic structures; in mitral position a rotation of a valve may result in significantly different ventricular flow fields. Several experimental studies of ventricular flow fields downstream prosthetic heart valves are reported in literature. Initially, flow fields were visualized in rigid *in-vitro* ventricle models for several valve designs (Reul *et al.*, 1981; Chandran *et al.*, 1989). More recently developed measurement techniques have enabled quantitative *in-vitro* measurements of flow patterns in deforming ventricle models. Such measurements were performed using Ultrasound (Garitey *et al.*, 1995) and digital particle image velocimetry (DPIV) (Vlachos *et al.*, 2001) techniques.

As the motion of a valve leaflet is the result of its interaction with the surrounding blood, changed ventricular flow patterns due to a change in mitral valve orientation may influence the motion of the (prosthetic) valve leaflets. The interaction between the aortic and mitral valves could also be changed. In turn, this might lead to a change in regurgitant flow and time of valve closure, which may influence the efficiency with which the heart pumps blood through the body. In this light, each valve design may have an optimum orientation for implantation. It would be valuable if the optimal valve orientation with respect to ventricular function could be predicted, patient-specifically and pre-operatively. Since the optimal orientation could be patient specific, experimental studies are impractical due to the inflexibility regarding geometrical variations. Computational models are more easily adapted and as such are suitable for such studies. In order to predict an optimum for mitral valve orientation using a computational model, such a model should simulate the full three dimensional ventricular flow during the entire cardiac cycle.

Computational models of ventricular flow are published in literature. However, many of these models are two dimensional, simulate only the ejection or the filling phase and most do not incorporate valve dynamics (Taylor and Yamaguchi, 1995; Redaelli and Montevecchi, 1996; Shortland *et al.*, 1996; Lemmon and Yoganathan, 2000; Vierendeels *et al.*, 2000; Saber *et al.*, 2001; Baccani *et al.*, 2003). The most advanced ventricular flow model presented in literature is that by Peskin and McQueen (1996), based on the immersed boundary method (Peskin, 1972). That model simulates three dimensional flow patterns in the left ventricle throughout the cardiac cycle, for native heart valves. However, the method is not reported to be applicable for physiologically relevant flow conditions. While many studies addressed valve properties and ventricular flow patterns, none of them focused on the role of valve orientation regarding the efficiency of the ventricle as a pump.

1.7 Aim of the study

The aim of this study is (1) to develop a computational model of the relation between mitral valve orientation and ventricular flow that can simulate the entire cardiac cy-

cle, and (2) to use that model to investigate to what extent the efficiency depends on the mutual orientation of the mitral and the aortic valve and the flow conditions. Such a model would be applicable for selecting optimal valve orientation and design for a patient specific ventricular geometry and loading condition. It may also be useful for surgical planning and as a design tool for artificial valves.

1.8 Outline of the thesis and methods used

Before studying the interaction of the valve with the local flow patterns, we first focus on understanding the complex three dimensional ventricular flow patterns themselves. Since the majority of implanted mechanical prostheses are bi-leaflet valves, this type of prosthesis is selected as the subject of study. In *Chapter 2*, a finite element method was used as a basis for developing a computational model of the relation between mitral valve orientation and ventricular flow patterns, and ultimately ventricular pump function. An Arbitrary Lagrangian-Eulerian (ALE) technique is applied to account for the deformation of the ventricular cavity. The obstruction caused by the mitral valve leaflets was accounted for by locally increasing the viscosity of the fluid. Ventricular flow was simulated for two mutually perpendicular orientations of a fixed mitral valve. In order to assess the quality of the computational results an *in-vitro* setup was built, incorporating a deforming rubber ventricle model and bi-leaflet valve prostheses in both the aortic and mitral positions. The DPIV method, also used by Vlachos *et al.* (2001), was selected to measure instantaneous velocity fields in cross sections of the flexible rubber model ventricle as it provides a high level of spatial and temporal detail at a high measurement rate.

In *Chapter 3*, the simplified description of the opened and closed valve is replaced by a description in which motion of geometrically realistic valve leaflets is governed by the interaction between the leaflets and the surrounding blood. The fictitious domain method was selected to account for the fluid-structure interaction between the valves and the blood. Application of the fictitious domain method for predicting the time dependent response of mechanical heart valve leaflet motion is evaluated for several pulsatile flow conditions in a two dimensional model of the aortic root including a sinus cavity. Particle image velocimetry data is gathered in a quasi two dimensional experimental setup and used for validation of the computational results.

In *Chapter 4* the fictitious domain method is applied to a two dimensional model with an inlet and an outlet valve, representing the left ventricular cavity with its mitral and aortic valve. At the apex of the cavity, flow pulses were applied of which the stroke volume and the frequency were varied to account for changes in the Reynolds and Strouhal number. A series of 9 different flow pulses is applied at the apex of the ventricle to study the effect of flow conditions on the regurgitant volumes of and the interaction between the mitral and aortic valves.

In *Chapter 5*, the two dimensional computational model presented in the previous chapter is used to study the effect of changing the rotation point of the mitral valve, i.e. valve orientation, on ventricular flow phenomena and the associated interaction between the two valves, when the same flow conditions are applied.

In *Chapter 6* a general discussion is presented as well as conclusions that are made based on this thesis.

Bibliography

Baccani, B., Domenichini, F., and Pedrizzetti, G. (2003). Model and influence of mitral valve opening during the left ventricular filling. *Journal of Biomechanics*, **36**, 355–361.

Butany, J., Fayet, C., Ahluwalia, M. S., Blit, P., Ahn, C., Munroe, C., Israel, N., Cusimano, R. J., and Leask, R. L. (2003). Biological replacement heart valves identification and evaluation. *Cardiovascular Pathology*, **12**, 119–139.

Chandran, K. B., Shoephoerster, R., and Dellsperger, K. C. (1989). Effect of prosthetic mitral valve geometry and orientation on flow dynamics in a model human left ventricle. *Journal of Biomechanics*, **22**, 51–65.

Garitey, V., Gandelheid, T., Fusezi, J., Pelissier, R., and Rieu, R. (1995). Ventricular flow dynamic past bileaflet prosthetic heart valves. *Int. J. Artificial Organs*, **18**, 380–391.

Hufnagel, C. A., Harvey, W. P., Rabil, P. J., and McDermott, T. F. (1954). Surgical correction of aortic insufficiency. *Surgery*, **35**, 673–683.

Iung, B., Baron, G., Butchard, E. G., Delahaye, F., Gohlke-B arwolf, C., Levang, O. W., Tornos, P., Vanoverschelde, J., Vermeer, F., Boersma, E., Ravaud, P., and Vahanian, A. (2003). A prospective survey of patients with valvular heart disease in europe: The euro heart survey on valvular heart disease. *European Heart Journal*, **24**, 1231–1243.

Lemmon, J. D. and Yoganathan, A. P. (2000). Three-dimensional computational model of left heart diastolic function with fluid-structure interaction. *Journal of Biomechanical Engineering*, **122**, 109–117.

Murday, A. J., Hochstitzky, A., Mansfield, J., Miles, J., Taylor, B., Whitley, E., and Treasure, T. (2003). A prospective controlled trial of St. Jude versus Starr Edwards aortic and mitral valve prostheses. *The Annals of Thoracic Surgery*, **76**, 66–74.

Peskin, C. S. (1972). Flow patterns around heart valves: a numerical method. *Journal of Computational Physics*, **10**, 252–271.

Peskin, C. S. and McQueen, D. M. (1996). *Fluid dynamics of the heart and its valves*. Prentice-Hall Inc., New Jersey.

Redaelli, A. and Montevecchi, F. M. (1996). Computational evaluation of intraventricular pressure gradients based on a fluid-structure approach. *Journal of Biomechanical Engineering, transactions of the ASME*, **118 (4)**, 529–537.

Reul, H., Talukder, N., and Muller, E. W. (1981). Fluid mechanics of the natural mitral valve. *Journal of Biomechanics*, **14(5)**, 361–372.

Saber, N. R., Gosman, A. D., Wood, N. B., Kilner, P. J., Charrier, C. L., and Firmin, D. N. (2001). Computational flow modeling of the left ventricle based on in vivo mri data: initial experience. *Annals of Biomedical Engineering*, **29**, 275–283.

Shortland, A. P., Black, R. A., Jarvis, J. C., Henry, F. S., Iudicello, I., Collins, M. W., and Salmons, S. (1996). Formation and travel of vortices in model ventricle: application to the design of skeletal muscle ventricles. *Journal of Biomechanics*, **29**, 503–511.

Taylor, T. W. and Yamaguchi, T. (1995). Realistic three-dimensional left ventricular ejection determined from computational fluid dynamics. *Med. Eng. Phys.*, **17 (8)**, 602–608.

Vierendeels, J. A., Riemslagh, K., Dick, E., and Verdonck, P. R. (2000). Computer simulation of intraventricular flow and pressure gradients during diastole. *Journal of Biomechanical Engineering*, **122**, 667–674.

Vlachos, P. P., Pierrakkos, O., Phillips, A., and Telionis, D. P. (2001). Vorticity and turbulence characteristics inside a transparent flexible left ventricle. *Proceedings of the 2001 ASME Bioengineering Conference*, **BED-Vol.50**, 493–495.

Chapter 2

Towards an experimentally validated 3D model of the relation between mitral valve orientation and left ventricular flow

Abstract

Geometrical properties of prosthetic mitral heart valves but also the alignment of their implantation are reported to significantly influence flow patterns in the left ventricle of the heart. The interaction between the mitral and aortic valve, thus the pump function of the heart, may be influenced hereby. Computational analyses to determine the effect of valve orientation on ventricular pump function pre-operatively and patient specifically would be valuable in selecting a preferred orientation of implantation. However, first the relation between mitral valve orientation and ventricular flow patterns would have to be predicted correctly by such a computational model. The aim of this work was to make a step towards an experimentally validated three dimensional computational model of the relation between prosthetic mitral valve orientation and left ventricular flow patterns, which can simulate the entire cardiac cycle under physiologically relevant conditions. In an in-vitro model of the left ventricle, fluid velocities were assessed quantitatively using digital particle image velocimetry, for two mitral valve orientations. The experiment was simulated with the CFD model at identical flow conditions, but slightly simplified geometric properties, for the entire cardiac cycle and both orientations of the mitral valve. For each valve orientation, both methods show similar a influence on the flow structures. As this study shows that a 90^o rotation of the mitral valve results in an almost completely reversed ventricular vortex structure during diastole, a significant impact on valve dynamics may be expected and further investigation that includes valve-valve interaction would be valuable.

2.1 Introduction

The four valves of the heart maintain the unidirectional flow of blood through the heart. Pathological changes may cause limitation of valve motion. The diseased valve may not be able to fully close, causing leakage (regurgitation), or it may not be able to open properly (stenosis), obstructing the blood to enter or leave the heart. In all cases the workload of the heart is increased. Often the condition of the native valve is such that valve replacement is desired. Two types of valve prostheses are commercially available; biological valves and mechanical valves. Although biological valve prostheses have better haemodynamic performances, a mechanical valve is commonly selected due to its high durability. Mechanical heart valve prostheses are available in several designs, one of which is the bi-leaflet mechanical valve which will be studied in this work. When a mitral valve is replaced, for example by a bi-leaflet mechanical prosthesis, the natural valve as shown in Figure 2.1(a) is taken out and a prosthesis is attached to the heart tissue in the mitral opening. However, since fixation is performed on a circular structure the prosthesis can be attached in any orientation. In Figure 2.1(b) the mitral prosthesis is shown in anatomical orientation (one leaflet proximal and one distal to the aortic valve) whereas in Figure 2.1(c) the anti-anatomical orientation is shown.

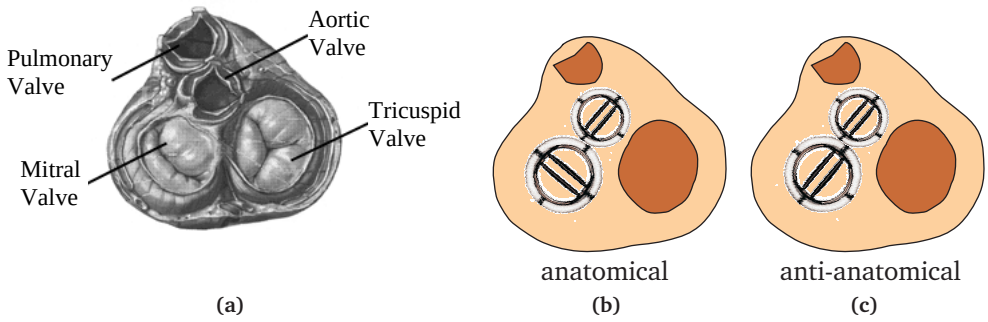

Figure 2.1: Schematic representation of the valve base of the heart with the four heart valves (a). A bi-leaflet mechanical valve prosthesis is shown in mitral position in anatomical (b) and anti-anatomical orientation (c) and also in the aortic position. The valve configurations in (b) and (c) are used both in the computations and the experiments.

The orientation and geometry of prosthetic heart valves in mitral position largely influence the flow pattern in the left ventricular cavity. Changing the orientation of the prosthetic mitral valve may influence the opening and closing behavior of the prosthesis and also the interaction with the aortic valve, compromising the amount of blood being pumped in the right direction (Pop *et al.*, 1989). Also the washout of the blood volume in the ventricle cavity may be affected. For these reasons, knowl-

edge of ventricular flow properties past a mitral valve prosthesis is of importance to the design of prosthetic valves and to the determination of the optimal orientation in which the prosthesis is to be implanted.

In the past, experimental studies of ventricular flow in the presence of a prosthetic valve have been performed using different techniques. Chandran *et al.* (1989) studied the pulsatile flow dynamics through bi-leaflet, tilting disc, caged ball, pericardial and porcine mitral valves in a rigid ventricle model by visualizing particle motion in the fluid. They found among other things that changing the orientation of the bi-leaflet valve prostheses results in different ventricular flow patterns. Garitey *et al.* (1995) used a flexible ventricle model to study ventricular flow by means of ultrasonic measurements and found that slight differences in valve design (Duromedics vs St. Jude) as well as valve orientation resulted in significant differences in ventricular flow. Digital Particle Image Velocimetry has been used by Vlachos *et al.* (2001) to study flow in a flexible ventricle model downstream a St. Jude Medical bi-leaflet heart valve. *In vivo* measurements using MR techniques (Walker *et al.*, 1996; Kilner *et al.*, 2000) showed the development of a large vortex in the ventricle downstream the natural mitral valve. While these experimental studies help to understand ventricular flow they are not flexible regarding variations in geometry, labor-intensive and expensive in constructing.

Numerical models are easily adapted for other geometries and help in reducing the amount of experiments necessary. They can also give information which is hard or impossible to measure. Computational modeling of the flow in the left ventricle is not trivial because of the complex geometry and large deformations of the cardiac wall, the motion of the heart valves, the high Reynolds number and the complexity of the in- and outflow boundary conditions. Only a few research groups have succeeded in developing a computational model in which some or all of these aspects have been incorporated. Many of these models are two dimensional, simulate only the ejection or the filling phase and most do not incorporate valve dynamics (Taylor and Yamaguchi, 1995; Redaelli and Montevecchi, 1996; Shortland *et al.*, 1996; Saber *et al.*, 2001; Lemmon and Yoganathan, 2000; Vierendeels *et al.*, 2000; Baccani *et al.*, 2003). The most advanced model is that by Peskin (Peskin, 1972; Peskin and McQueen, 1996) based on the Immersed Boundary Technique. This model includes the changing geometry of the ventricle and the motion of the valve leaflets. The forces exerted on the fluid by the cardiac muscle are applied to the fluid as local body forces at the location of the cardiac wall. These forces are empirical, thus no solid wall is present in the computational model. It is unclear how realistic wall material properties could be introduced. Furthermore the model was only applicable for relatively low, non-physiological Reynolds numbers. Lemmon and Yoganathan (2000) developed a model based on Peskin's Immersed Boundary Method, and added an algorithm described by Patankar (1983), which provided stability of the solutions for physiological Reynolds numbers. In this model, only the filling phase is simulated and valve motion is not taken into account.

The models referred to, either do not incorporate a valve structure but prescribe a mitral valve velocity profile (Vierendeels *et al.*, 2000; Saber *et al.*, 2001; Baccani *et al.*,

2003) or incorporate native mitral valves, either static (Lemmon and Yoganathan, 2000) or moving (Peskin and McQueen, 1989). In none of these models, influence of prosthetic valve orientation on ventricular flow patterns was studied. The aim of this work was to make a step towards a computational model which can describe the relation between the prosthetic mitral valve orientation and left ventricular flow patterns, in a three dimensional setting during the entire cardiac cycle under physiological flow conditions, and to assess the quality of the model by comparing the results to DPIV data obtained in an *in-vitro* setup. In order to be able to study the impact of the orientation and design of a prosthetic mitral valve on the pump function of the heart, the ultimate computational ventricle model should simulate the interaction between ventricular flow patterns, the valve dynamics and the heart muscle contraction.

This work represents a first step towards an experimentally validated three dimensional computational model of the flow in the left ventricle, which can simulate the entire cardiac cycle under physiologically relevant conditions. Presently, the model is driven by a three dimensional deformation of the cavity and simulates the flow in the cavity during the entire cardiac cycle. A simplified ventricular geometry is chosen, such that the essence of the geometry of the natural ventricle was captured. The model mitral valve is geometrically simplified to two parallel narrow plates located in the mitral inflow area. The open aortic valve is represented by a circular orifice. Valve dynamics were simplified such that the valve was modeled either in a fully opened or a fully closed configuration. In an *in-vitro* setup, experimental data on the ventricular flow fields was obtained using Digital Particle Image Velocimetry (DPIV) measurements, for two mutually perpendicular orientations of the mitral valve. The setup consisted of a deformable left ventricle with Carbomedics bi-leaflet valve prostheses both in the mitral and aortic position.

2.2 Methods

2.2.1 Experimental Method

Set-up

A transparent polyurethane model of the left ventricle was made (see Figure 2.3 (a)) by a dip-coating procedure inside a glass model of the left ventricle. The polyurethane has a high resistance to tear, and using the dip-coating procedure a wall thickness of approximately 0.5 mm was obtained. However, a uniform wall thickness is not guaranteed. The geometry, based on an MRI image of the systolic left ventricle of a young healthy volunteer (see Figure 2.2), was approximated by an ellipsoid, from mitral opening to apex, with a major axis of 65 mm and a minor axis of 18 mm. The ellipsoid was truncated at 11.5 mm above the equator. To the side of the mitral opening a straight tube with a diameter of 25 mm intersects the ellipsoid under an angle of 45 degrees. The end systolic volume of the model is 80 ml.

The polyurethane model was mounted in a transparent PMMA (Plexiglas) box at the location of the valves (see Figure 2.3 (b)). In both valve openings a Carbomedics bi-leaflet valve prosthesis - as shown in Figure 2.4 - was mounted.

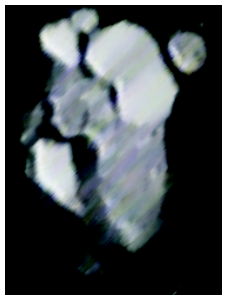

Figure 2.2: MRI image of a healthy human left ventricle at end systole.

The ventricle model was deformed by changing the volume of the Plexiglas box by a computer controlled excitation of a piston. Since the fluid volume outside the ventricle model is constant, the piston motion directly translates to the volume change of the ventricle.

Above the mitral opening a reservoir has the function of the atrium. A constant fluid level ensures a constant pressure upstream the mitral valve. A polyurethane tube connects the aortic opening to a system which represents the arterial impedance. This system, like a Windkessel model, incorporates an inertance, a resistance and a compliance. The inertance is determined by the mass of fluid that needs to be accelerated inside the tube connecting the aortic opening to the compliance tank.

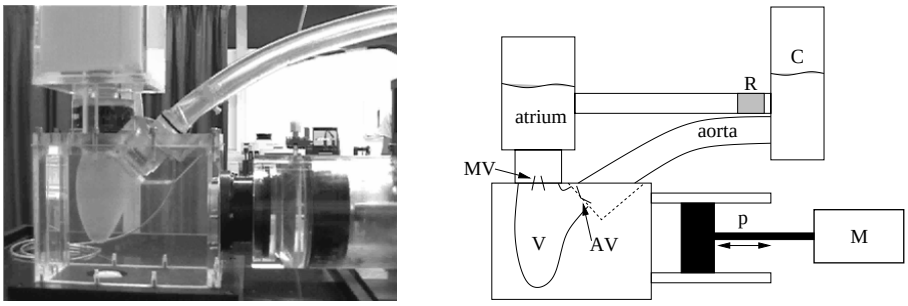

(a) **(b)**

Figure 2.3: Picture of the polyurethane ventricle mounted in a PMMA box (a) and a schematic representation of the entire setup (b), where V represents the ventricle, MV the mitral valve, AV the aortic valve, p the piston which is excited by a computer controlled linear motor M, C a compliance tank and R a resistance.

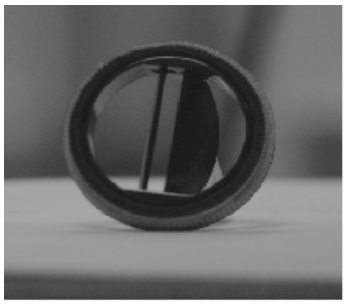

Figure 2.4: Image of the Carbomedics bi-leaflet valve prosthesis.

The compliance of this tank is realized by entrapment of an adjustable amount of air inside. In the outflow channel of the tank a porous foam represents the resistance, which can be varied by compressing the foam.

The fluid used was a solution of glycerol in water (55 % by weight of glycerol in water), which has a density of $\rho = 1.13{\cdot}10^3$ [kg/m^3] and a viscosity of $\eta = 8.0{\cdot}\ 10^{-3}$ [kg/m·s]. The piston motion was prescribed to be a sinus in time with a stroke length of 10 mm. With a piston diameter of 80 mm, this results in a stroke volume of 50 ml, such that cavity volume varied between 80 and 130 ml, and a cycle time of 1 second. The resulting flow is characterized by a Reynolds number in the order of $1.2{\cdot}10^3$ and a Strouhal number of 0.05, based on inner mitral diameter and average peak velocity.

Digital Particle Image Velocimetry

Fluid velocity fields were measured using a DPIV system (Dantec, PIV-1100). To this end the fluid was seeded with light reflecting particles (Hollow Glass Spheres) with a mean diameter of 20 μm and a density of 1010 kg/m^3.

The seeded fluid was illuminated twice at a short time interval Δt, with a double-pulsed laser sheet (New Wave Minilase II), as shown in Figure 2.5. A CCD camera (Kodak ES-1.0) was used to record the position of the seeding particles in two cross sections of the ventricle model; the cross section through the free (F) wall and the

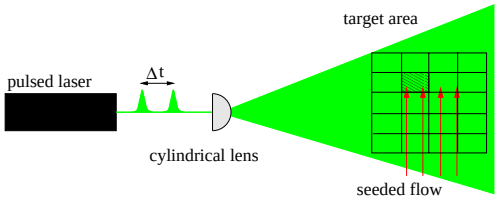

Figure 2.5: Schematic representation of the illumination of the seeded fluid flow by means of a double-pulsed Yag-laser.

septum (S), and the cross section through the anterior (A) and the posterior (P) wall as shown in Figure 2.6(a) (FS-plane) and (b) (AP-plane).

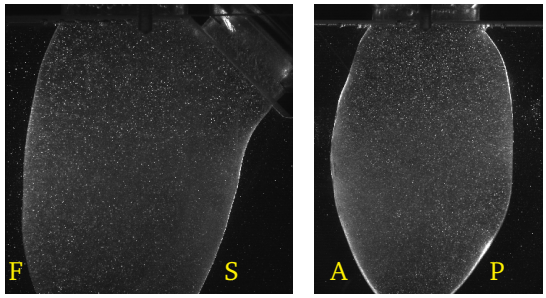

(a) **(b)**

Figure 2.6: Images of the PIV camera showing seeding particles in the cross-section of the ventricle through the Free (F) wall and the Septal (S) wall (FS-plane) (a) and in the cross-section through the Anterior (A) and Posterior (P) wall (AP-plane) (b) in diastole.

In the FS-plane the camera images were 1016 by 1008 pixels, whereas 800 by 1008 pixels were used for the AP-plane. The camera images were subdivided into interrogation areas of 32 by 32 pixels, corresponding to areas of 2.16 by 2.16 mm for the FS-plane and 2.56 by 2.56 mm for the AP-plane. A correlation technique was applied to the interrogation areas of subsequent camera images to determine the average displacement within the interrogation areas. The velocity field was derived by dividing the displacement field, obtained from the correlation technique, by the time between subsequent images.

In order to obtain good quality correlations, the maximum particle displacement should not exceed a quarter of the interrogation area size (Willert and Gharib, 1991). To this end, the time between two subsequent images (denoted by Δt in Figure 2.5) was set to 1000 microseconds at a maximum velocity estimated to be 0.5 m/s. The size of the seeding particles in the image was approximately three pixels which enabled sub-pixel accuracy of the position measurement up to 0.1 times the pixel pitch. Thus, the smallest resolvable velocity would be $7 \cdot 10^{-3}$ m/s. In order to obtain more detailed information on the velocity field, an overlap of 50% of the interrogation areas was applied. In the way described above, the whole velocity field in one plane is measured at one instant in the cycle.

Data acquisition

A series of such measurements was taken to obtain the velocity field during the entire cardiac cycle. With the DPIV system, a maximum of 7.5 image pairs per second could

be recorded, and subsequently stored. In order to increase the number of samples in a cycle, the frequency of the double-pulsed laser was set to 14.9 Hz and image pairs were recorded at each 15^{th} pulse, i.e. at time intervals of $\frac{15}{14.9}$ seconds, over a total time of 150 seconds. In this way the fluid velocity was sampled during the entire cycle at a time resolution of 6 ms, under the assumption that the flow patterns were periodical. To this end, the setup was run for 10 cycles during which the pressure and flow pulses became cyclic before the first measurement was performed. Three series of 150 measurements were taken for each cross-section of the ventricle and each valve orientation. The velocity fields were averaged over these three samples. Furthermore, three subsequent measurements were averaged such that 50 velocity fields result, each the average of 9 individual measurements.

2.2.2 Computational Method

A three dimensional computational model of the flow in the left ventricular cavity was developed. An Arbitrary Lagrangian-Eulerian (ALE) finite element method was used to compute the fluid velocity field in the cavity by solving the Navier-Stokes equation (eq. 2.1) and the continuity equation (eq. 2.2), which for a moving grid read (Donea *et al.*, 1982; Schreurs *et al.*, 1986):

$$\rho\left(\frac{\partial^* \mathbf{v}}{\partial t} + (\mathbf{v}-\mathbf{g})\cdot\boldsymbol{\nabla}\mathbf{v}\right) = \boldsymbol{\nabla}\cdot(-p\mathbf{I} + 2\eta\mathbf{D}) \tag{2.1}$$

$$\boldsymbol{\nabla}\cdot\mathbf{v} = \mathbf{0} \tag{2.2}$$

where ρ represents the density, $\frac{\partial^*}{\partial t}$ is a local time derivative with respect to the moving grid, $\mathbf{v}$ the fluid velocity , t the time, $\mathbf{g}$ the grid velocity (equation 2.3), p the pressure, η the dynamic viscosity and $\mathbf{D}$ the rate of deformation tensor $\mathbf{D} = \frac{1}{2}\left[(\boldsymbol{\nabla}\mathbf{v}) + (\boldsymbol{\nabla}\mathbf{v})^T\right]$.

Finite element computations were performed using the mesh shown in Figure 2.7 (a), which consists of 3598 quadratic Crouzeix-Raviart type 3D brick elements with 27 nodes per element. Figure 2.7 (a) shows the ventricle section of the mesh, including the mitral and aortic opening. Upstream the mitral opening, an inflow channel with a length of 8 times the mitral diameter was modeled, gradually increasing in diameter from 22 mm to 60 mm according to a circle with a radius of 50 cm, in order to obtain convergence for the entrance flow. Adaptation of the fluid elements inside the mesh to the varying geometry was obtained from solving a linear elastic problem, using the deformation of the outer surface as a Dirichlet boundary condition. This was done to ensure iso-parametric elements throughout the entire cardiac cycle. Deformation of the mesh leads to a new set of coordinates.The grid velocity $\mathbf{g}$ is then derived from the grid positions by:

$$\mathbf{g} = \frac{\mathbf{u}^{n+1} - \mathbf{u}^n}{\Delta t} \tag{2.3}$$

with $\mathbf{u}^n$ the coordinates of the grid points at time $t = t_n$. Constant time steps of 2 ms were applied.

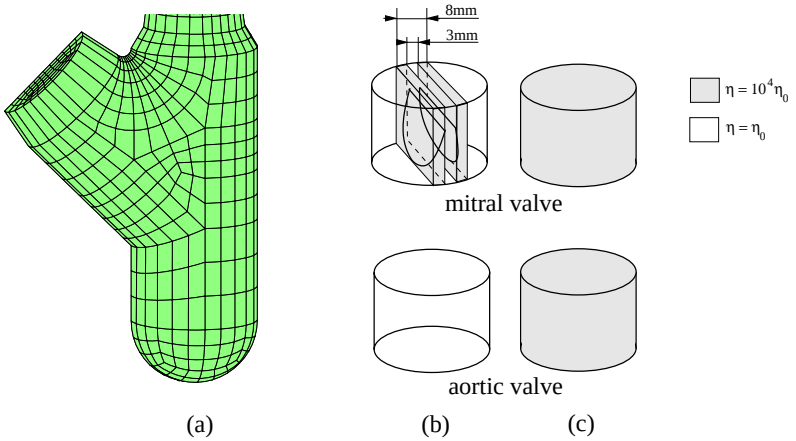

Figure 2.7: Mesh for the finite element computations (a), and drawings of the model mitral and aortic valves in opened (b) and closed (c) position; the high viscosity area ($10^4\eta_o$) is shaded. A schematic representation of a bi-leaflet valve prosthesis in opened configuration is drawn inside modeled open mitral valve (panel b).

In the model, the geometry of the *in-vitro* model was approximated by the geometry shown in Figure 2.7(a). The geometry consists of two intersecting tubes with a diameter of 3 centimeters and a 45 degree angle between the axial directions of the tubes. The apex is an ellipsoid. The geometry has a volume of 80 ml. The angle of 45 degrees between the axis of the outflow tract and the normal direction of the mitral valve, the outer mitral valve diameter and the distance between mitral valve and apex match the values in the experimental setup. The experimental wall motion was approximated by prescribing a radial motion of the surface nodes , which was varied sinusoidally over the height of the ventricle. At each time step, the amplitude of the radial displacement was chosen such that the associated volume matched the experimental volume.

In order to include the effect of mitral valve orientation the opened mitral valve was modeled as two plates with a thickness of 2.5 mm each, and 3 mm of space in between, spanning the entire diameter of the mitral opening, by locally increasing the viscosity of the fluid. From the mitral opening to the entrance of the inflow channel upstream the mitral valve, the viscosity in the shaded areas was lowered linearly from $10^4\eta_0$ to η_0, with η_0 equal to the fluid viscosity of $8{\cdot}10^{-3}$ [kg/m·s]. For the closed mitral valve the viscosity in the entire inflow region was raised to $10^4\eta_0$. Panels (b) and (c) of Figure 2.7 show a schematic representation of the valve structure in opened and closed configuration. The dimensions of the high viscosity areas in opened configuration were chosen such that the entire opened prosthetic valve leaflets fit inside each area, as shown by the schematic representation of the opened mitral valve prosthesis in Figure 2.7 (b). Similar to the closed mitral valve,

the viscosity in the aorta was raised for the closed aortic valve.

The valves were modeled either opened or closed, without transition. The timing of valve opening and closing was based on the direction of the wall movement. In this way the valve behaves ideally: no regurgitation occurs before valve closure. For an opened valve, the normal component of the stress vector $\mathbf{n} \cdot \sigma \cdot \mathbf{n}$ was prescribed to be zero, whereas for a closed valve the velocity was prescribed to be zero at the in- or outflow surface.

Temporal discretization of the Navier-Stokes equation was achieved using an implicit Euler scheme. Galerkin's method was used for the spatial discretization, while the linearization of the convective term was obtained using Newton's method. An iterative solver, based on a Bi-CGStab method (van der Vorst, 1992) was used to solve the linearized system equation.

2.3 Experimental results

The measured fluid velocity fields are presented in Figure 2.8. From top to bottom the cardiac cycle progresses from early diastole (T1) to mid diastole (T2) to end diastole (T3) to peak systole (T4). The size of the interrogation areas is represented by the space between two neighboring points in both directions.

anatomical mitral valve orientation
At the start of the cycle (T1 in Figure 2.8), the fluid velocity is low in the entire cavity. At mid diastole (T2), two jets (I and II) have entered the ventricle through the lateral orifices of the mitral valve. One of them (I) travels towards the apex along the free wall while the other (II) is directed towards the septal wall. As the latter jet (II) hits the septum, most of the fluid is directed towards the apex while a small amount of fluid is directed towards the aortic valve where it creates a vortex (3) in the outflow tract. A smaller jet (III) enters the ventricle through the central valve orifice and fills up the space between the two major jets. The central jet lags behind the two major ones. At the end of the filling phase (T3), the major jets have traveled towards the apex along the free and septal walls. In the apical area, reversed flow appears between the two major jets (I and II), creating two counter-rotating vortices (1 and 2). The vortex nearest to the free wall (1) is located slightly below the other (2). The vortex (3) that developed in the outflow tract has traveled in apical direction along the septal wall and has reached halfway into the ventricle. At peak systole (T4), the ventricular vortices have largely diminished and the fluid is directed in the direction of the aortic valve.

In the AP-plane (b, T1), fluid velocity is low at the start of the cycle. At mid diastole (T2), the central jet (III) is visible. Two counter-rotating vortices (4 and 5) are present alongside the central jet, with reversed flow to the anterior and posterior walls. At the end of ventricular filling (T3) the central jet has traveled halfway down the ventricle, the reversed flow has increased and reaches up to the mitral valve. At peak systole (T4), the flow in the entire cavity is directed upward, with the highest velocity to the upper part of the anterior and posterior walls.

anti-anatomical mitral valve orientation
In the FS-plane (Figure 2.8(d)), the fluid velocity at the start of the cycle (T1) is low in the entire ventricle. At mid diastole (T2), a jet (III') has entered the ventricle through the central mitral valve orifice. Two counter-rotating vortices (4' and 5') have developed to the sides of the jet. Through the second half of the diastolic phase, the jet front travels to the center of the cavity while it diminishes in strength as the ventricle reaches its maximum volume (T3). At peak systole (T4), the vortices have largely diminished and the fluid is directed towards the aorta in the entire ventricular cavity. In the central region of the ventricle the velocity is relatively low compared to the velocity at the free and septal wall.

Also in the AP-plane (Figure 2.8(e)), the fluid velocity is low in the entire cross section of the ventricle at the start of the cycle (T1). At mid diastole (T2), two jets (I' and II') enter the ventricle through the lateral orifices of the mitral valve. One of these jets (I') travels towards the apex along the anterior wall, the other (II') along the posterior wall. In the center of the mitral opening, a smaller third jet (III') enters through the central orifice of the valve. This jet lags behind and fills the space between the two major jets. At the end of the filling phase (T3), the fluid velocity has decreased and two counter rotating vortices (4' and 5') develop between the two major jets in the bottom half of the ventricle, below the small central jet. At peak systole (T4), the in-plane fluid velocity is relatively low compared to peak diastole as the fluid moves out of plane towards the aorta.

2.4 Computational results

CFD simulations were performed where a wall deformation of the ventricular cavity was prescribed such that the stroke volume amounted to 50 ml, matching the stroke volume in the experiments. To check the volume change applied to the model ventricle, the velocity in the mitral valve was integrated over the valve orifice area, thus obtaining momentary flow rates which are presented in Figure 2.10 (a). Multiplication of the momentary flow rates by the duration of the time steps, and summing them from the beginning to the end of the filling phase results in the fluid volume that entered the model ventricle and is shown in Figure 2.10 (b). The total volume change obtained in this way was 49.9 ml, confirming the computationally applied stroke volume.

Figure 2.9 shows the computed fluid velocity fields, from top to bottom at early diastole, mid diastole, end diastole and peak systole. Velocity components were interpolated from the computational nodes to a rectangular grid using the basis functions of the finite element method. The fluid flow structures in the computational results are largely similar to those obtained in the experiments, although towards the end of the filling phase the fluid velocity in the jets and in the areas of reversed flow resulting from the computations are significantly higher than obtained experimentally. In general, the fluid entering through the lateral orifices of the mitral valve sticks to the walls and as it travels towards the apex two counter-rotating vortices develop

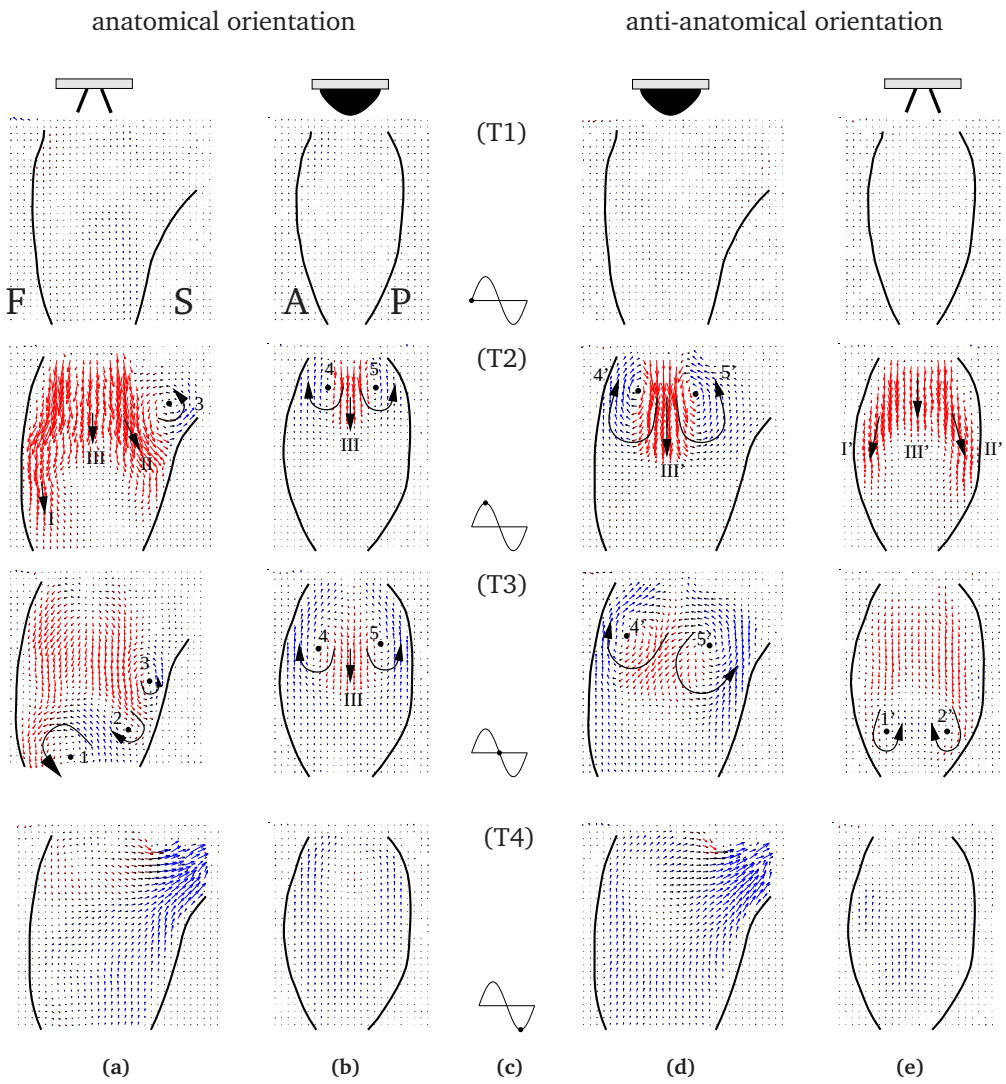

Figure 2.8: Measured (DPIV) fluid velocity fields in the FS-plane ((a) and (d)) and in the AP-plane ((b) and (e)) at four equidistant instants in the cardiac cycle, denoted by the dot in the flow curve (c). The orientation of the mitral valve is given at the top of each column. The velocity vectors directed downward are colored red while velocity vectors directed upward are colored blue. The ventricular wall is drawn in each vector plot.

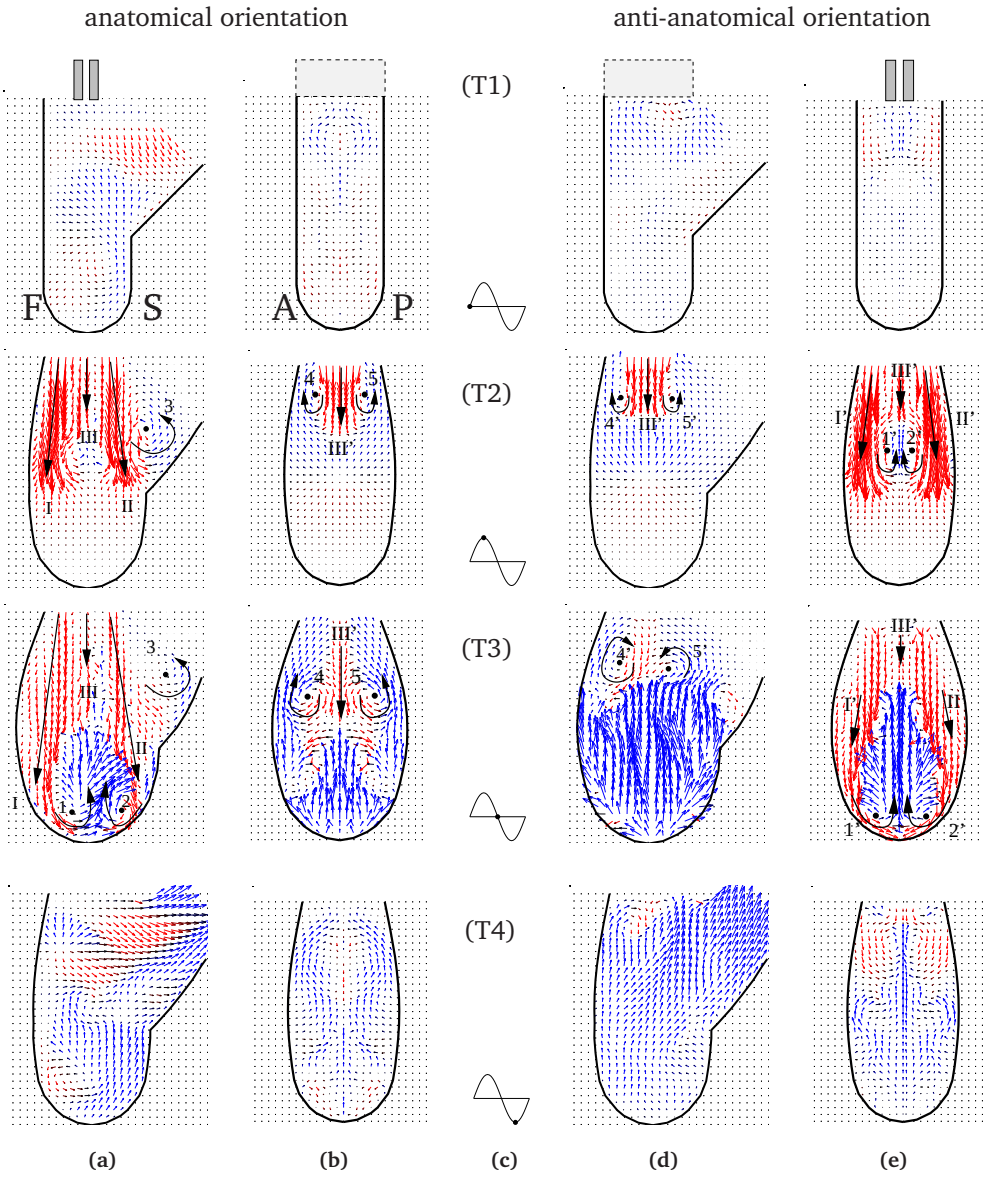

Figure 2.9: Computed (FEM) fluid velocity fields at four equidistant instances in the cardiac cycle indicated by the dot in the flow pulse (c). Results are interpolated on a rectangular grid through the FS-plane ((a) and (d)) and the AP-plane ((b) and (e)). Vectors are colored red for downward and blue for upward velocity direction and scaled identical to Figure 2.8. The boundary of the computational mesh is drawn in each plot.

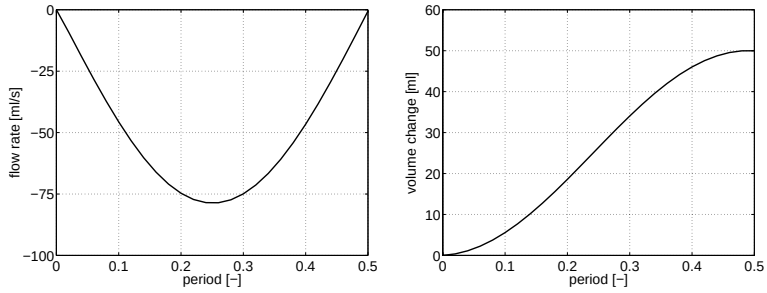

(a) **(b)**

Figure 2.10: Flow rate in mitral valve computed from results (a) and fluid volume entered through mitral valve (b) during the ventricular filling phase.

between the jets with reversed flow in between (Figure 2.9 (a) and (e)). A third jet enters through the central orifice which is smaller than the two major jets and lags behind them in traveling towards the apex. In the plane of the central orifice (Figure 2.9 (b) and (d)), the central jet enters the ventricle as two counter-rotating vortices develop to the sides of this jet with reversed flow to the walls. The vortices in the plane of the central orifice (panel (b) and (d)) stay in the upper half of the ventricle, whereas the vortices induced by the two large lateral jets (panel (a) and (e)) develop mid-ventricle and travel towards the apex.

A quantitative comparison of the experimental and computational velocity fields, presented in Figures 2.8 and 2.9 respectively, is given in Figure 2.11. To this end, the vertical velocity component was interpolated to several cross sections of the ventricle. It is evident from these interpolated vertical velocity components that at mid diastole (T2, (a) and (e)) the velocity in the lateral jets resulting from the computations is significantly higher than obtained from the measurements. Also the jets are more to the long axis of the ventricle in the computational results. The difference in velocity in the central jet, visible in columns (b) and (d) is not as pronounced.

At the end of the filling phase the mismatch between experimental and computational velocities is the highest, as in the experiments the jets diminish whereas in the computations the increased velocity in the lateral jets has also resulted in increased back-flow velocity.

Also presented in Figure 2.11, is the position of the ventricle wall. In diastole, the shape of the computational ventricle model closely matches that of the experimental model. For decreasing ventricle volumes, however, the shape of the ventricular cavity matches worse. Nonetheless, the volumes of both models match throughout the entire cycle.

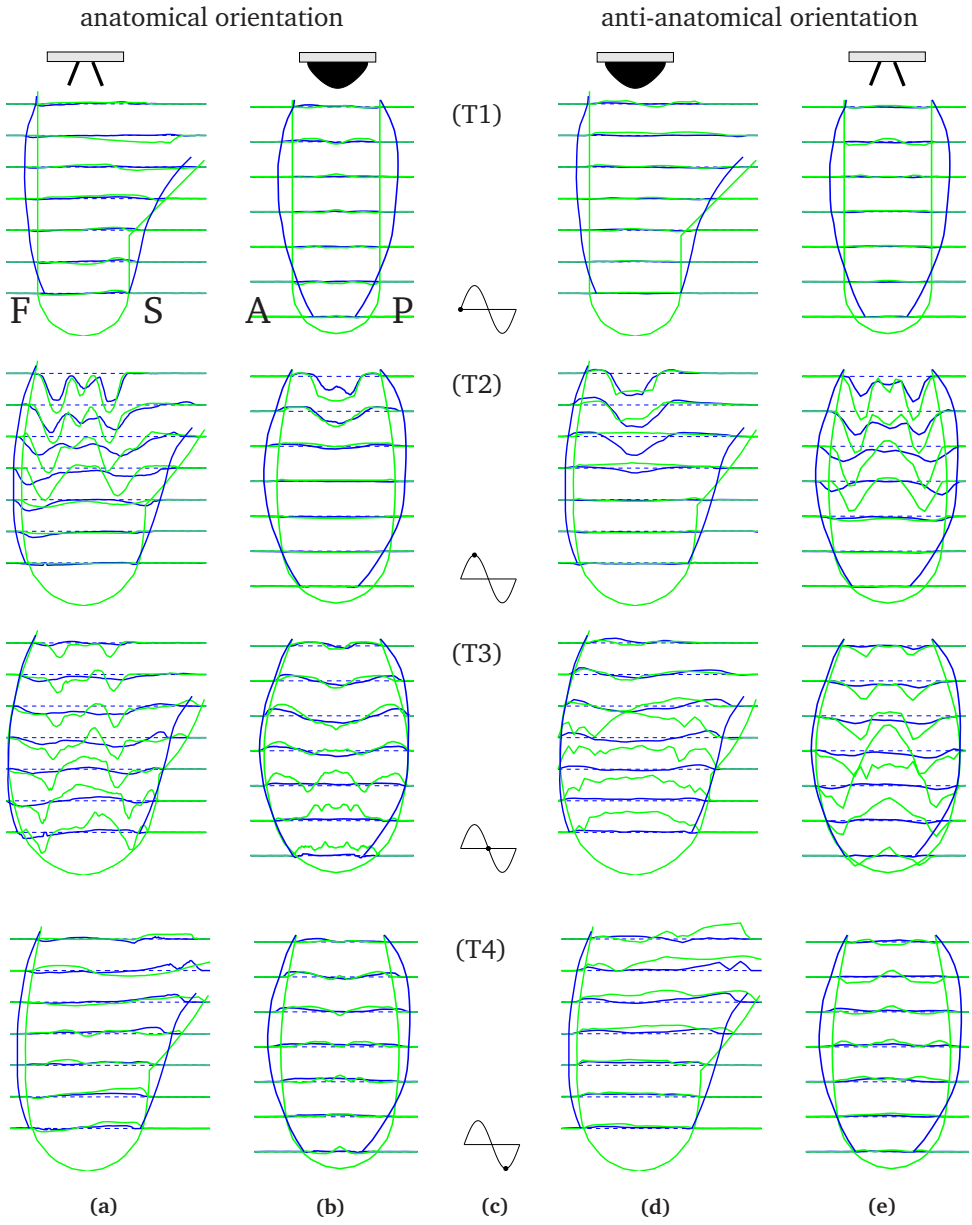

Figure 2.11: Interpolated vertical velocity components at several cross sections of the ventricle in the FS-plane ((a) and (d)) and the AP-plane ((b) and (e)) at four equidistant instants in the flow cycle indicated in (c). Computational data is represented by light lines, experimental data by dark lines.

2.5 Discussion

The aim of this work was to make a step towards an experimentally validated three dimensional computational model of the relation between prosthetic mitral valve orientation and left ventricular flow patterns, which can simulate the entire cardiac cycle under physiologically relevant conditions, and to assess its quality by quantitatively comparing the results to experimental data obtained in an *in-vitro* setup using DPIV measurements.

Both models were used to investigate the influence of mitral valve orientation on left ventricular flow, and both confirmed earlier reports that a 90 degree rotation of the mitral valve results in a significantly different ventricular flow pattern (Chandran *et al.*, 1989; Garitey *et al.*, 1995). Although similar flow structures were found in the experiments and the computations, the quantitative comparison in Figure 2.11 shows that the current computational model did not predict the fluid velocity field successfully.

The flow conditions applied in both the computations and the experiments, based on an inner mitral diameter of 22 mm, a period time of 1 second and an average peak inflow velocity of 0.4 m/s, are characterized by a Reynolds number in the order of $1.2{\cdot}10^3$ and a Strouhal number of 0.05. Physiologically, the flow is characterized by a Reynolds number in the order of magnitude of $3{\cdot}10^3$ and a Strouhal number of 0.04. The computational model did not allow higher settings of the Reynolds number. Therefore, the viscosity of the fluid was raised to $8{\cdot}10^{-3}$ such that convergence of the solutions was obtained. As such, the flow conditions do not match the physiological settings of a Reynolds number in the order of magnitude of $3{\cdot}10^3$ and a Strouhal number of 0.04. However, in a preliminary study the ventricular flow patterns were visualized for experiments with a Reynolds number of $2.6{\cdot}10^3$.

In Figure 2.12, arrows representing the ventricular flow patterns near the end of the diastolic phase are superimposed on images of a CCD camera. The flow structures observed in these visualizations for a Reynolds number of $2.6{\cdot}10^3$ are similar to those found in the computations and the measurements performed for a Reynolds number of $1.2{\cdot}10^3$ for both orientations of the mitral valve. In this respect, the Reynolds number does not seem to be a major influence to the flow structures developing during ventricular filling, although the location of the flow structures as well as the local velocity is influenced.

To explain the discrepancy between the experimental and computational results, we first focus on the quality of the experimental data. The fluid motion was assessed through a DPIV technique, in which instantaneous fluid velocity fields are derived by correlating particle displacements within interrogation areas of subsequent images. As such, measured velocities represent an average over the interrogation area, and details in the velocity field with a length scale below the size of the interrogation area are averaged out. This averaging effect may become important near small vortices and near the boundaries of jets. As a result, the measured velocity immediately downstream the mitral valve at peak flow rate may be lower than in reality. In our experiments, interrogation areas have a size of just over 2 mm, which is small compared to the 8 mm distance between the tips of the leaflets at the downstream

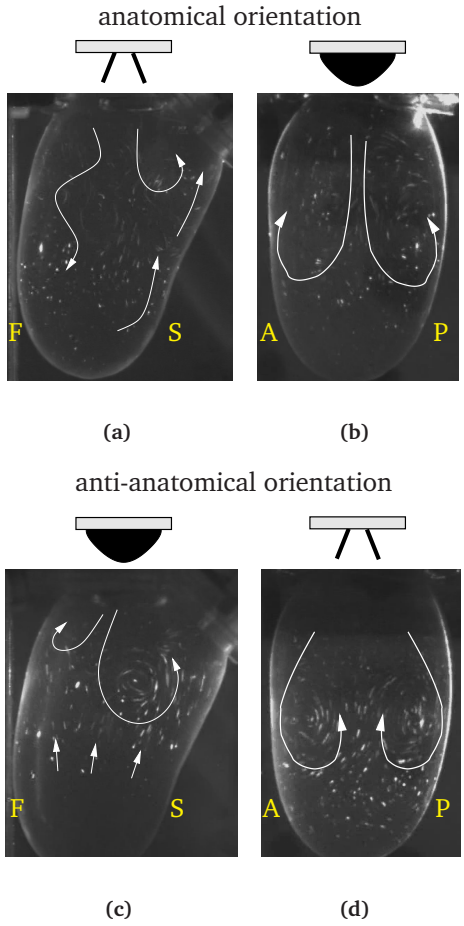

Figure 2.12: Camera images of moving seeding particles in the plane through the free wall and the septum (FS-plane) ((a) and (c)) and in the plane through the anterior and posterior wall (AP-plane)((b) and (d)) at the end of the rapid filling phase. In the FS-plane the mitral valve is located horizontally near the top while the aortic valve is under an angle of 45 degrees to the top right of the image. The AP-plane is viewed from the free wall side. Arrows representing the flow directions are superimposed for the anatomical (a) and (b) and the anti-anatomical (c) and (d) orientation of the mitral valve.

side of the mitral valve. Therefore, it is expected that lower experimental velocity (compared to the simulation) measured in the center of the jets is not caused by the averaging of the correlation. Besides the averaging error, the DPIV measurements could also be affected by distortion of the images because of the breaking of light

at the polyurethane-fluid interface. This effect is assumed to be negligible as the polyurethane is very thin.

Focusing on the computational model several sources for the discrepancy in experimental and computational results can be pointed out, especially approximations in the geometry such as valve shape and ventricle shape.

The difference in flow fields suggest that the experimental flow conditions were not equal to those in the computations. However, the duration of the cardiac cycle was equal, as was the viscosity of the fluid. Also the mitral diameter was matching. A very small deviation in the stroke volume was present, 50.3 ml was applied by the piston motion of 10 mm, whereas 50 ml was applied in the computational model, which was confirmed by determining the inflow through the mitral orifice which amounted to 49.9 ml as shown in Figure 2.10(b).

Regarding the valve model, motion of the valve leaflets was neglected and the timing of valve opening and closing was prescribed. The duration of the opening and closing of the valve leaflets is short compared to the duration of the systolic and diastolic phase and is therefore expected not to be of major importance to the flow patterns developing in the left ventricle. Furthermore, the pressure at the in- or outflow surface of an opened valve was prescribed to be zero. This is possible because the valves are not opened simultaneously and it does not influence the flow in a cavity with prescribed wall velocity, since the fluid velocity is governed by pressure gradients rather than the absolute value of the pressure. Regarding the valve shape, the thickness of each of the prosthetic valve leaflets is about 0.5 mm, whereas the thickness of the computational valve model is 2.5 mm per leaflet, which means a reduction of valve orifice area of approximately 29%. The average inflow velocity is the volumetric flow divided by orifice area, thus a significant increase in computed average inflow velocity can be expected on account of the valve model. A reason why the two jets through the lateral orifices are further apart in the experiments than in the computations may be found in the opening angle of the fully opened mitral valve leaflets, which is about 73 degrees. As the fluid upstream the valve flows alongside the valve leaflets, it is directed away from the long axis of the ventricle towards the walls. As shown in Figure 2.7 (c), in the computational model the valve angle is 90 degrees and as such the jets through the lateral orifices will not be diverted on account of the valve.

The starting geometry represents the ventricle at the beginning of the filling phase. At that instant, the experimental geometry is elliptical while the computational geometry is cylindrical. As a result, in the experiments the upper half of the ventricle is wider in the filling phase, allowing the jets through the lateral valve orifices to be further apart from each other, as shown in Figure 2.11 in the left and right plots at time T2. As the jets have more space in the experiments, the velocity in the jet can be lower without affecting the flow volume. At the end of the filling phase, however, the shape of the ventricle in the experiments is matched by the computational mesh, except in the outflow tract (near the aorta).

In order to improve the computational model, full three dimensional information is needed on the geometry of the experimental ventricle model throughout the cycle. Also the valve model should be improved, with respect to the orifice area and leaflet

position in the open state. A thinner valve structure , using an increased viscosity technique, will require substantial mesh refinement upstream the mitral opening. This in turn, will lead to increased memory usage and CPU-time. Updating the valve position according to the measured valve position will even increase these requirements. Not taking valve motion into account, replacement of the high viscosity valve model by a mesh boundary where Dirichlet boundary conditions can be applied might be an option, but this is difficult to achieve using brick elements and the current mesh generator. Alternatively, application of local forces to account for the fixed, fully opened valve structure, in a manner similar to the immersed boundary method presented by Peskin (1972) might provide a solution, as the fluid mesh and the valve structure are independent of each other. Application of a fictitious domain method to replace the current valve model, as used by de Hart *et al.* (2000, 2003), will enable a correct valve geometry in a fixed position.

Summarizing, similar flow structures were found for both mitral valve orientations, although quantitative agreement between the computational results and experimental data was not reached. Improved valve geometry and ventricle shape might lead to a better quantitative agreement with the experiments. But still, prescribing the timing of opening and closure based on the flow pulse would be erroneous. Ultimately, valve behavior should be the result of valve-fluid interaction. Possibly, a fictitious domain method enables the analysis of the interaction of the valve leaflets with the fluid motion. Therefore, in the next chapter we will focus on the description of valve-fluid interaction using a fictitious domain method. To obtain a good understanding of the interaction between the fluid flow and the motion of the valve leaflets, we will study this interaction in two dimensional models in which the flow structures are less complex.

Bibliography

Baccani, B., Domenichini, F., and Pedrizzetti, G. (2003). Model and influence of mitral valve opening during the left ventricular filling. *Journal of Biomechanics*, **36**, 355–361.

Chandran, K. B., Shoephoerster, R., and Dellsperger, K. C. (1989). Effect of prosthetic mitral valve geometry and orientation on flow dynamics in a model human left ventricle. *Journal of Biomechanics*, **22**, 51–65.

de Hart, J., Peters, G. W. M., Schreurs, P. J. G., and Baaijens, F. P. T. (2000). A two-dimensional fluid-structure interaction model of the aortic valve. *Journal of Biomechanics*, **33**, 1079–1088.

de Hart, J., Peters, G. W. M., Schreurs, P. J. G., and Baaijens, F. P. T. (2003). A three-dimensional computational analysis of fluid-structure interaction in the aortic valve. *Journal of Biomechanics*, **36**, 103–112.

Donea, J., Giuliani, S., and Halleux, J. P. (1982). An arbitrary lagrangian-eulerian finite element method for transient dynamic fluid-structure interactions. *Computer Methods in Applied Mechanics and Engineering*, **33**, 689–723.

Garitey, V., Gandelheid, T., Fusezi, J., Pelissier, R., and Rieu, R. (1995). Ventricular flow dynamic past bileaflet prosthetic heart valves. *Int. J. Artificial Organs*, **18**, 380–391.

Kilner, P. J., Yang, G. Z., Wilkes, A. J., Mohiaddin, R. H., Firmin, D. N., and Yacoub, M. H. (2000). Asymmetric redirection of flow through the heart. *Nature*, **404**, 759–761.

Lemmon, J. D. and Yoganathan, A. P. (2000). Three-dimensional computational model of left heart diastolic function with fluid-structure interaction. *Journal of Biomechanical Engineering*, **122**, 109–117.

Patankar, S. V. (1983). *Numerical heat transfer and fluid flow*. Hemisphere Publishing Corporation, McGraw-Hill, New York.

Peskin, C. S. (1972). Flow patterns around heart valves: a numerical method. *Journal of Computational Physics*, **10**, 252–271.

Peskin, C. S. and McQueen, D. M. (1989). A three-dimensional computational method for blood flow in the heart: I. immersed elastic fibers in a viscous incompressible fluid. *Journal of Computational Physics*, **81**, 372–405.

Peskin, C. S. and McQueen, D. M. (1996). *Fluid dynamics of the heart and its valves*. Prentice-Hall Inc., New Jersey.

Pop, G., Sutherland, G. R., Roelandt, J., Vletter, W., and Bos, E. (1989). What is the ideal orientation of a mitral disc prosthesis? an in vivo haemodynamic study based on colour flow imaging and continuous wave doppler. *European Heart Journal*, **10**, 346–353.

Redaelli, A. and Montevecchi, F. M. (1996). Computational evaluation of intraventricular pressure gradients based on a fluid-structure approach. *Journal of Biomechanical Engineering, transactions of the ASME*, **118 (4)**, 529–537.

Saber, N. R., Gosman, A. D., Wood, N. B., Kilner, P. J., Charrier, C. L., and Firmin, D. N. (2001). Computational flow modeling of the left ventricle based on in vivo mri data: initial experience. *Annals of Biomedical Engineering*, **29**, 275–283.

Schreurs, P. J. G., Veldpaus, F. E., and Brekelmans, W. A. M. (1986). Simulation of forming processes, using the arbitrary eulerian-lagrangian formulation. *Computer Methods in Applied Mechanics and Engineering*, **58**, 19–36.

Shortland, A. P., Black, R. A., Jarvis, J. C., Henry, F. S., Iudicello, I., Collins, M. W., and Salmons, S. (1996). Formation and travel of vortices in model ventricle: application to the design of skeletal muscle ventricles. *Journal of Biomechanics*, **29**, 503–511.

Taylor, T. W. and Yamaguchi, T. (1995). Realistic three-dimensional left ventricular ejection determined from computational fluid dynamics. *Med. Eng. Phys.*, **17 (8)**, 602–608.

van der Vorst, H. (1992). Bi-cgstab: A fast and smoothly converging variant of bi-cg for the solution of nonsymmetric linear systems. *SIAM Journal on Scientific and Statistical Computing*, **13(2)**, 631–644.

Vierendeels, J. A., Riemslagh, K., Dick, E., and Verdonck, P. R. (2000). Computer simulation of intraventricular flow and pressure gradients during diastole. *Journal of Biomechanical Engineering*, **122**, 667–674.

Vlachos, P. P., Pierrakkos, O., Phillips, A., and Telionis, D. P. (2001). Vorticity and turbulence characteristics inside a transparent flexible left ventricle. *Proceedings of the 2001 ASME Bioengineering Conference*, **BED-Vol.50**, 493–495.

Walker, P. G., Cranney, G. B., Grimes, R. Y., Delatore, J., Rectenwald, J., Phost, G. M., and Yoganathan, A. P. (1996). Three-dimensional reconstruction of the flow in a human left heart by using magnetic resonance phase velocity encoding. *Journal of Biomedical Engineering*, **24**, 139–147.

Willert, C. E. and Gharib, M. (1991). Digital particle image velocimetry. *Experiments in Fluids*, **10**, 181–193.

Chapter 3

Evaluation of a fictitious domain method for predicting dynamic response of mechanical heart valves[1]

Abstract

Flow phenomena around heart valves are important for the motion of the valve leaflets, hence the dynamics of the valve. This work presents an evaluation of a two dimensional moving rigid heart valve, in which a fictitious domain method is used to describe fluid-structure interaction. Valve motion and fluid flow around the valve were computed for several Reynolds and Strouhal numbers. Particle Image Velocimetry measurements in an in-vitro experimental setup were performed to validate the computational results. The influences of variations of the flow pulse, expressed in Reynolds and Strouhal number, are well predicted by the computational method. As the fictitious domain method can readily be applied to fully three-dimensional fluid structure interaction problems, this study indicates that this method is well suited for the analysis of valve dynamics and ventricular flow in physiologically realistic geometries.

[1] This Chapter is accepted for publication in the Journal of Fluids and Structures

3.1 Introduction

The four valves of the heart maintain the unidirectional flow of blood through the heart. Pathologies of one or more of the valves may cause significant limitation of their function and subsequently the pump function of the heart. The diseased valve may not be able to fully close, causing leakage (regurgitation), or it may not be able to open properly (stenosis), obstructing the blood to enter or leave the heart. The function of one of the valves may be compromised to an extent that valve replacement is desired. In many cases a mechanical prosthesis will be chosen, because of its high durability. Several different shapes of valve prostheses have been developed and evaluated in the past (Chandran *et al.*, 1989).

Compared to the natural valve, these prostheses have several drawbacks in common with respect to their haemodynamic performance, like increased trans-valvular pressure gradient, increased back-flow during closure and increased shear stresses in the blood causing damage to or activation of blood platelets (Chandran *et al.*, 1989). These phenomena are all related to the design and properties of the valve.
In-vivo, *in-vitro* and numerical studies are commonly used to investigate the relation between valve design and function. *In-vivo* investigation of flow through heart valves is possible, for example using ultrasound (Pop *et al.*, 1989) or MR-techniques (Walker *et al.*, 1996; Kilner *et al.*, 2000). While *in-vivo* studies assess valve function in the final application, *in-vitro* setups allow for a more controllable, accessible and reproducible assessment the behavior of prosthetic valves. In such setups several techniques have been used such as flow visualization (Reul *et al.*, 1981; Chandran *et al.*, 1989; Lim *et al.*, 2001), pressure drop measurements (Chandran *et al.*, 1989; Pop *et al.*, 1989; Garitey *et al.*, 1995; Cape *et al.*, 1996), regurgitant flow measurements (Chandran *et al.*, 1989), velocity measurements using ultrasound (Pop *et al.*, 1989; Garitey *et al.*, 1995), LDA (Fatemi and Chandran, 1989; King *et al.*, 1996; Grigioni *et al.*, 2001) and DPIV (Bluestein *et al.*, 2000; Lim *et al.*, 2001; Vlachos *et al.*, 2001). Experimental studies also have some drawbacks: they are expensive, labor-intensive and not flexible with respect to geometrical variations.

Computational Fluid Dynamics (CFD) models are more flexible in applying variations in geometry, and less expensive in constructing. Thus, CFD models are a useful tool to reduce the amount of experiments necessary. Moreover, they can provide information that is hard, or even impossible, to measure.

In some CFD models, flow around heart valves in fixed position is studied (King *et al.*, 1996; Krafczyk *et al.*, 1998; Lemmon and Yoganathan, 2000; Bluestein *et al.*, 2002). These models are suitable for analyzing trans-valvular pressure drop and shear stresses at the surface of the valve leaflets. CFD models can also be useful to study the influence of valve orientation on the flow patterns downstream, as described in Chapter 2. In order to study the pump function of the heart, however, analysis of valve motion is necessary.

The behavior of an opening and closing valve depends on the interaction between the motion of the valve and the motion of the surrounding fluid. Furthermore, when investigating the pump function of the left heart, i.e. ejection fraction, it has to be noted that there is an interaction between the mitral and aortic valve: the opening

timing of one valve is influenced by the closing behavior of the other valve. Hence, in order to study the dynamics of a mechanical valve prosthesis and the associated pump function of the ventricle, valve motion and time-dependent fluid-structure interaction has to be taken into account in the computational model.

Also computational models of moving valves have been published in the last three decennia (Peskin, 1972; Peskin and McQueen, 1995; Horsten, 1990; de Hart *et al.*, 2000; Baccani *et al.*, 2003; de Hart *et al.*, 2003). Baccani *et al.* (2003) prescribed the velocity of a moving valve as a boundary condition on the fluid. In this way, no real interaction between valve and fluid motion was taken into account and it was not necessary to adapt the computational grid of the fluid domain to the position of the valve.

In order to allow the local coupling of fluid and valve properties, the mesh of the fluid domain will have to be updated to follow the motion of the valve. One way to do this is the use of an Arbitrary Lagrange-Eulerian (ALE) method with a moving grid for the velocity domain. This method was used by Horsten (1990) for modeling a moving aortic valve leaflet in a pulsatile flow, and by Vierendeels *et al.* (2000) for the analysis of the filling of a deforming axisymmetric ventricle where no valve was present in the mitral orifice. The ALE method was also applied in Chapter 2, where the influence of mitral valve orientation on the flowpatterns inside the deforming ventricle was analyzed. In this method the positions of the computational grid of the fluid are adapted based on the position of the moving valve, while maintaining the grid topology. When analyzing flow through moving valves, the large translations of the valve leaflets cause the quality of the grid to degenerate rapidly. Complete closure of an initially opened valve is not possible using this method.
In order to maintain the quality of the computational grid, remeshing combined with an ALE-technique can be applied. This method is more commonly used in solid mechanics (Kwak and Im, 2003). Remeshing requires interpolation techniques to transfer state variables from the old mesh to the new one, which may introduce additional inaccuracies. Furthermore, remeshing is a computationally expensive technique and may be very difficult to apply for three dimensional problems.

One of the most advanced models incorporating fluid-structure interaction is a left ventricle model by Peskin (Peskin, 1972; Peskin and McQueen, 1995). In this model the immersed boundary technique is used, which effectively uses local volume forces on the fluid to account for the interaction between the fluid and the heart wall and the valves. In this way, there is no need to change the fluid mesh thus avoiding the corresponding problems described above. However, to guarantee the stability of the numerical technique used, the viscosity was increased to 25 times that of blood resulting in a Reynolds number in the order of magnitude of 80, which is 25 times lower than physiological (Peskin and McQueen, 1995). Lemmon and Yoganathan (2000) used Peskin's immersed boundary technique and applied a semi-implicit method for pressure linked equations (Patankar, 1983) to provide solution stability for physiological Reynolds numbers. However, their model did not incorporate moving heart valves.

Recently, fictitious domain methods (Glowinski *et al.*, 1994; Bertrand *et al.*, 1997; de Hart *et al.*, 2000; Baaijens, 2001) have been introduced to couple quantities on separate meshes. The method enables the coupling of velocities of a structure to fluid velocities while the structural mesh arbitrarily moves through the fluid mesh. De Hart *et al.* (2000) applied and validated a fictitious domain method in a two dimensional model of a flexible aortic valve, and extended it to a three dimensional realistic geometry (de Hart *et al.*, 2003), for a single set of the characteristic fluid flow parameters, i.e. the Reynolds and Strouhal number. Successful simulation of a fluid-structure interaction problem with a very stiff elastic solid in a fluid is not trivial. The eigenvalues of the system are related to the viscosity of the fluid and to the stiffness of the solid. Since the stiffness of a mechanical valve is considerably higher than that of a flexible leaflet, the range of eigenvalues of the system to be solved is increased, which adversely affects its stability .

The objective of this work is to investigate the applicability of a fictitious domain method for simulating the motion of a stiff prosthetic heart valve leaflet. To this end, model predictions on flow fields and on timing of valve motion are compared to experimental results obtained in a quasi two dimensional experiment. To evaluate the sensitivity of the computational method to variations in the characteristic fluid flow parameters, expressed in the Reynolds and Strouhal numbers, a range of flow pulses was used in the computational method and the results were compared to the respective experimental findings.

3.2 Methods

3.2.1 Experimental method

To validate the predictions of the two dimensional version of the computational model an experimental setup, based on the one used by de Hart *et al.* (2000), was used. The geometry of the measurement section, shown in Figure 3.1, is a quasi two dimensional

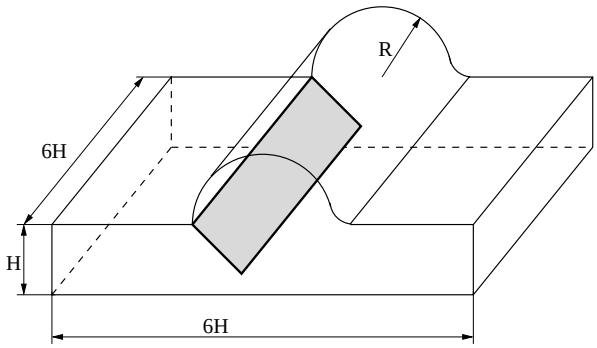

Figure 3.1: Schematic drawing of the geometry of the measurement section.

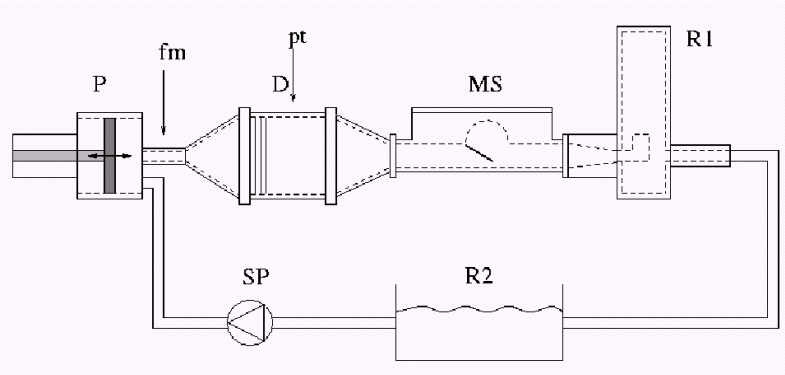

Figure 3.2: Schematic representation of the pulse duplicator. (P) piston; (D) diffuser; (MS) measurement section; (R1, R2) reservoir; (SP) steady pump; (fm) flow meter; (pt) pressure transducer.

representation of a cross section of a stiff aortic valve with a sinus cavity. It consists of a Plexiglas channel with a height H of 20 mm and length 6H. Halfway the length of the channel is a cylindrical cavity, representing the sinus cavity of the aortic valve, with radius R equal to H. In order to obtain a two dimensional flow field in the center plane of the channel, the width of the channel is 6H. At the upstream side of the sinus cavity a stiff strip of lexane is fixed to the top of the channel. The fixation was realized using three pieces of water resistant adhesive tape, one next to the center of the channel and two near the side walls. The width of the adhesive tape was 5 mm, in order to keep the bending stiffness low. The measurement section, built of Plexiglas, was mounted in a pulse duplicator setup as shown in Figure 3.2. The setup consists of a steady pump (SP), a computer controlled piston (P), a diffuser (D), the measurement section (MS), a reservoir combined with a resistance (R1) and a reservoir (R2). The reservoir attached to the measurement section was completely filled with fluid, such that the setup was not compliant. To be able to obtain physiologically relevant fluid flow parameters, the fluid used was a mixture of 36% by volume of glycerol in water with a viscosity of $4.3 \cdot 10^{-3}$ [kg/m·s]. The viscosity of this mixture matches the viscosity of blood assuming newtonian constitutive behavior.

The flow pulse used is shown in Figure 3.3. The pulsatile flow rate is obtained as follows. The steady pump creates a stationary flow rate, on top of which a pulsating flow is superimposed by applying a periodical motion of the computer controlled piston. The forward motion of the piston results in a flow rate higher than the stationary component and lasts 0.38 T, with T the period time of the signal. The reversed stroke of the piston lasts the rest of the period time. The resulting flow pulse resembles the physiological aortic flow pulse, in the sense that there is a large systolic flow peak lasting approximately 38% of the cardiac cycle and a relatively low flow rate throughout the rest of the cardiac cycle. This choice enabled a variation of the Reynolds and

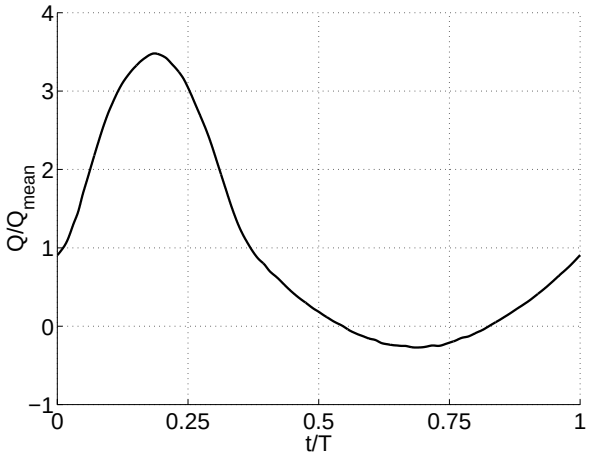

Figure 3.3: Flow pulse measured by the electromagnetic flow probe, located between the piston and the diffuser.

Strouhal number, by variation of the amplitude and frequency of the piston motion, without changing the characteristics of the flow pulse.

The flow is characterized by the Reynolds and Strouhal numbers, given by:

$$Re = \frac{\rho V H}{\eta}; \qquad Sr = \frac{H}{TV} \tag{3.1}$$

with ρ the fluid density, V the average peak velocity over the height H of the channel, η the dynamic viscosity of the fluid and T a time constant chosen to be the period time.

Several flow conditions were applied in order to study the effect on the dynamic behavior of the valve. The amplitude of the flow pulse was changed such that at peak flow rate the required Reynolds numbers were reached. Next, the frequency was changed in order to reach relevant Strouhal numbers. Finally, the magnitude of the steady flow component was adjusted such that the amount of back-flow obtained was enough to close the valve at the end of the back-flow phase. Within the possibilities of the setup used, the Reynolds number could be varied from 500 to 750 for a Strouhal number of 0.055. For Reynolds number 750 the Strouhal number was varied both ways by 0.025. The corresponding period times are shown in Table 3.1.

For each case presented in Table 3.1, instantaneous whole field velocities were measured using a Particle Image Velocimetry system (Dantec PIV-1100). To obtain the fluid velocity field using the PIV technique (Willert and Gharib, 1991; Westerweel, 1993), the fluid was seeded with light reflecting particles (Hollow Glass Spheres) with a mean diameter of 100 μm and a density of 1010 kg/m^3.

The seeded fluid was illuminated with a pulsed laser sheet directed through the center plane of the measurement section. A CCD camera (Kodak ES-1.0) recorded the

Table 3.1: Period time of the applied flow pulse for each experiment.

	Sr=0.03	Sr=0.055	Sr=0.08
Re=500	–	3.70 (case 1)	–
Re=750	4.50 (case 2)	2.45 (case 3)	1.65 (case 4)

position of the seeding particles and the valve leaflet (see Figure 3.4). The camera images of 1016 by 1008 pixels were subdivided into interrogation areas of 64 x 64 pixels, corresponding to 7.5 x 7.5 mm. A correlation technique was applied to the interrogation areas of subsequent camera images to determine the average displacement within the interrogation areas. In order to obtain good quality correlations, the maximum particle displacement should not exceed a quarter of the interrogation area size (Willert and Gharib, 1991). To this end, the time between two subsequent images is set to 1000 microseconds at a maximum velocity estimated to be 0.2 m/s. A sub-pixel interpolation technique was used which allows for the detection of particle motion up to 0.1 times the pixel pitch. Thus, the smallest resolvable velocity would be $1.25 \cdot 10^{-3}$ m/s. The velocity field is derived by dividing the displacement field, obtained from the correlation technique, by the time between subsequent images. The opening angle of the valve (shown in Figure 3.5) is derived straightforwardly from the position shown in the camera images.

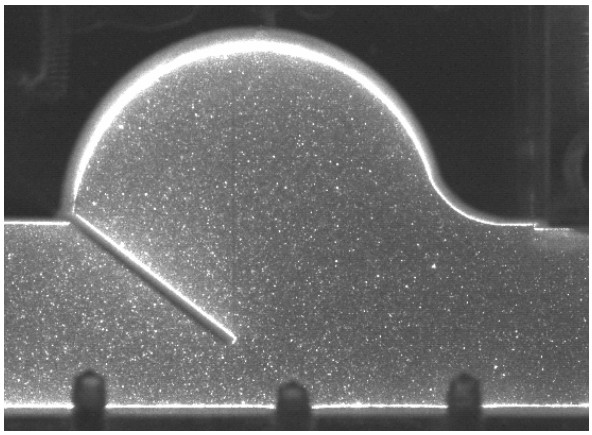

Figure 3.4: Image of the PIV camera showing the sinus cavity and the stiff leaflet. Only the particles in the laser sheet are detected by the camera.

3.2.2 Computational Method

The geometry used in the computations corresponds to the geometry of the center plane of the experimental setup, and is shown in Figure 3.5. The fluid domain is denoted by Ω_f, the solid domain by Ω_s.

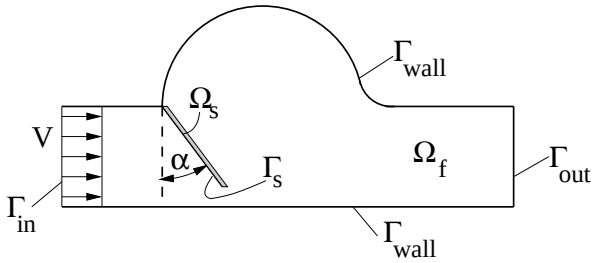

Figure 3.5: Schematic representation of the geometry, the domain of the fluid (Ω_f) and solid (Ω_s) phase, the boundaries of the domains, the inflow boundary condition (V) and the definition of the opening angle of the valve (α).

The fluid motion is computed by solving the Navier-Stokes equation (3.2) and the continuity equation (3.3),

$$\rho\left(\frac{\partial \mathbf{v}_f}{\partial t} + \mathbf{v}_f \cdot \boldsymbol{\nabla}\mathbf{v}_f\right) = \boldsymbol{\nabla}\cdot(-p\,\mathbf{I} + 2\eta\mathbf{D}) + \mathbf{f}_f^* \qquad \text{in } \Omega_f \qquad (3.2)$$

$$\boldsymbol{\nabla}\cdot\mathbf{v}_f = 0 \qquad \text{in } \Omega_f \qquad (3.3)$$

where ρ represents the fluid density, $\mathbf{v}_f$ the fluid velocity field, t the time, p the pressure, η the dynamic viscosity, $\mathbf{D}$ the rate of deformation tensor $\mathbf{D} = \frac{1}{2}(\boldsymbol{\nabla}\mathbf{v}_f + (\boldsymbol{\nabla}\mathbf{v}_f)^T)$ and $\mathbf{f}_f^*$ the body forces. In the computational method laminar flow is assumed of a newtonian, isothermal and incompressible fluid.

At the top and the bottom of the fluid domain, denoted, by Γ_{wall}, no-slip boundary conditions were applied. The experimentally obtained flow pulse given in figure 3.3 was approximated by a positive and a negative part of a sinus, and applied in the shape of a plug flow at the inlet (Γ_{in}) boundary. At the outlet (Γ_{out}) the tangential velocity and the normal component of the stress vector ($\boldsymbol{\sigma}_f \cdot \mathbf{n}_f$) were set to zero.

The valve is considered to be a stiff incompressible elastic solid strip. The momentum equation of the solid is given by:

$$\boldsymbol{\nabla}\cdot\boldsymbol{\sigma_s} = \mathbf{0} \qquad \text{in } \Omega_s \qquad (3.4)$$

$$\det(\mathbf{F}) = 1 \qquad \text{in } \Omega_s \qquad (3.5)$$

where $\boldsymbol{\sigma_s}$ is the Cauchy stress tensor of the solid, $\mathbf{F}$ the deformation tensor $\mathbf{F} = (\boldsymbol{\nabla}_0\mathbf{x}_s)^T = \mathbf{I} + (\boldsymbol{\nabla}_0\mathbf{u}_s)^T$, $\boldsymbol{\nabla}_0$ the gradient operator with respect to the initial configuration, $\mathbf{x}_s$ the solid position field and $\mathbf{u}_s$ the displacement vector. Body forces were

neglected. The density of the stiff leaflet is assumed equal to the fluid density, allowing the buoyancy forces to be neglected. The inertia of the stiff valve is not taken into account since the mass of the leaflets is negligible with respect to the fluid mass.

The incompressible, isotropic material of the valve leaflet is subject to small strains. Therefore a physically linear constitutive model is used for the material behavior. A geometrically non-linear model is used to deal with the large rotations of the leaflet, describing the strain of the solid in an objective manner:

$$\boldsymbol{\sigma}_s = -p_s\mathbf{I} + \boldsymbol{\tau}_s; \qquad \boldsymbol{\tau}_s = G(\mathbf{B} - \mathbf{I}) \qquad \text{in } \Omega_s \tag{3.6}$$

where p_s is the hydrostatic pressure in the solid and $\boldsymbol{\tau}_s$ the extra stress tensor. The extra stress tensor is a function of the shear modulus G and the left Cauchy-Green strain tensor $\mathbf{B}$ which is defined as $\mathbf{B} = \mathbf{F} \cdot \mathbf{F}^{\mathbf{T}}$.

The stiff leaflet is fixed at a point to the top right corner. In this point, the displacement is prescribed to be zero. As a result, free rotation of the leaflet around this point is allowed.

At the boundary of the solid domain Γ_s, which is completely immersed in Ω_f, the velocities of the fluid and the solid are coupled:

$$\mathbf{v}_f = \mathbf{v}_s = \dot{\mathbf{u}}_s \qquad \text{on } \Gamma_s \tag{3.7}$$

with $\dot{\mathbf{u}}_s$ the time derivative of the displacement field. Furthermore, the stress exerted by the solid on the fluid and the stress exerted on the solid by the fluid are in equilibrium at the boundary of the solid domain Γ_s:

$$\boldsymbol{\sigma}_f \cdot \mathbf{n}_f = \boldsymbol{\sigma}_s \cdot \mathbf{n}_s \qquad \text{on } \Gamma_s \tag{3.8}$$

with $\mathbf{n}_s$ the outward normal of the solid domain and $\mathbf{n}_f$ the outward normal of the fluid domain, i.e. the opposite direction. However, the fluid domain does not have a physical boundary at the location of the boundary of the solid domain, which is where the fictitious domain method comes in.

In the original formulation of the fictitious domain method a variational approach is used. In this formulation, the use of Lagrange multipliers to establish coupling between fluid and structure is commonly applied. However, there exists no variational principle for the Navier-Stokes equations due to the non-linear term. Nevertheless, the method is used by deriving the weak form of the Stokes equation and adding the non-linear term afterwards (Bertrand *et al.*, 1997). Alternatively, the weighted residuals method can be applied. In this formulation, the stress exerted by the solid on the fluid can be regarded as a locally acting body force. Using the Dirac-delta function $\delta(\mathbf{x})$, the body force $\mathbf{f}_f^*$ in equation (3.2) can be described as:

$$\mathbf{f}_f^* = \mathbf{f}_f \; \delta(\mathbf{x} - \mathbf{x}_{\Gamma_s}) \qquad \text{in } \Omega_f \tag{3.9}$$

where $\mathbf{f}_f^*$ only has values unequal to zero at the fluid-structure interaction interface Γ_s. This introduces a globally acting surface force $\mathbf{f}_f$, localized at the interface Γ_s by

means of the delta function. Making use of the property of the delta function, the body force term in the Navier-Stokes equation (eq. 3.2) can, in the weak form, be written as:

$$\int_{\Omega_f} \mathbf{w}_f \cdot \mathbf{f}_f^* \, d\Omega_f = \int_{\Omega_f} \mathbf{w}_f \cdot \mathbf{f}_f \, \delta(\mathbf{x} - \mathbf{x}_{\Gamma_s}) \, d\Omega_f = \int_{\Gamma_s} \mathbf{w}_f \cdot \mathbf{f}_f \, d\Gamma_s \text{in } \Omega_f \tag{3.10}$$

with $\mathbf{w}_f$ the weighting functions defined in the fluid domain. The rightmost expression in equation (3.10) is the same term as added to the system equations using the variational principle (Bertrand *et al.*, 1997), where $\mathbf{f}_f$ is regarded as a Lagrange multiplier.
When deriving the weak formulation for the solid equations, partial integration results in a boundary integral in which the external load of the fluid on the valve can be incorporated:

$$\int_{\Omega_s} \mathbf{w}_s \cdot (\boldsymbol{\nabla} \cdot \boldsymbol{\sigma}_s) \, d\Omega_s = -\int_{\Omega_s} (\boldsymbol{\nabla} \mathbf{w}_s)^T : \boldsymbol{\sigma}_s \, d\Omega_s + \int_{\Gamma_s} \mathbf{w}_s \cdot (\boldsymbol{\sigma}_s \cdot \mathbf{n}_s) \, d\Gamma_s \tag{3.11}$$

In order to reach an equilibrium of interaction forces, the last term in equation (3.11) must be in equilibrium with the righthandside of equation (3.10):

$$\int_{\Gamma_s} \mathbf{w}_s \cdot (\boldsymbol{\sigma}_s \cdot \mathbf{n}_s) \, d\Gamma_s = \int_{\Gamma_s} \mathbf{w}_f \cdot \mathbf{f}_f \, d\Gamma_s \tag{3.12}$$

As the pressure p of equation (3.2) is used to weakly enforce the incompressibility constraint (equation 3.3), the interaction force $\mathbf{f}_f$ is used as a Lagrange multiplier to weakly couple the velocities of the fluid and solid domain on non-conforming discretizations,

$$\int_{\Gamma_s} \mathbf{w}_i \cdot (\mathbf{v}_s - \mathbf{v}_f) \, d\Gamma_s = 0 \tag{3.13}$$

with $\mathbf{w}_i$ the weighting functions defined on the fluid-structure interaction interface. Generally, the fluid-structure interaction interface entails the entire boundary Γ_s of the solid domain Ω_s. Extra coupling equations (eq. 3.13) are introduced where coupling is required. In the case of a thin leaflet, however, two sides of the boundary of the solid are very close to each other. This may lead to an overconstraining of velocity unknowns per element in the fluid domain. This may introduce deteriorating convergence properties of the solution procedure. To circumvent this problem, the interaction is approximated by only taking the upstream part (Γ_i) of the solid boundary Γ_s into account. As the valve leaflet is thin, this approximation will only influence trans-valvular stresses and strains and it may be assumed not to influence the fluid-structure interaction.

In the momentum equation for the fluid (eq. 3.2), as in the fluid-structure interaction equation (eq. 3.13), the velocity field is considered. However, the unknown

quantity in the momentum equation for the solid is the displacement field $\mathbf{u}_s$. For the velocity field of the solid during a time step a first order approximation of the displacement field $\mathbf{u}_s$ is used:

$$\mathbf{v}_s = \frac{\mathbf{u}_s - \mathbf{u}_s^n}{\Delta\, t} \tag{3.14}$$

where Δt represents the time step. The variables ($\mathbf{x}$) can be approximated by the sum of their estimates ($\hat{\mathbf{x}}$) and their error ($\delta\mathbf{x}$). This procedure is elaborated in appendix A; in summary while writing $\boldsymbol{\sigma}_s \cdot \mathbf{n}_s = \mathbf{f}_s$, the weak form of the governing equations read:

$$\begin{aligned}
&\int_{\Omega_f} \rho\mathbf{w}_f \cdot \left(\frac{\delta\mathbf{v}_f}{\Delta\, t} + \hat{\mathbf{v}}_f \cdot \boldsymbol{\nabla}\delta\mathbf{v}_f + \delta\mathbf{v}_f \cdot \boldsymbol{\nabla}\hat{\mathbf{v}}_f\right)\, d\Omega_f + \int_{\Omega_f} (\boldsymbol{\nabla}\mathbf{w}_f)^T : \delta\boldsymbol{\tau}_f\, d\Omega_f + \\
&\quad - \int_{\Omega_f} (\boldsymbol{\nabla}\cdot\mathbf{w}_f)\delta p_f\, d\Omega_f - \int_{\Gamma_i} \mathbf{w}_f \cdot \delta\mathbf{f}_f\, d\Gamma_i \;= \\
&\quad - \int_{\Omega_f} \rho\mathbf{w}_f \cdot \left(\frac{\hat{\mathbf{v}}_f - \mathbf{v}^n}{\Delta\, t} + \hat{\mathbf{v}}_f \cdot \boldsymbol{\nabla}\hat{\mathbf{v}}_f\right) - (\boldsymbol{\nabla}\mathbf{w}_f)^T : \hat{\boldsymbol{\sigma}}_f\, d\Omega_f + \\
&\quad + \int_{\Gamma_f} \mathbf{w}_f \cdot \mathbf{t}_f\, d\Gamma_f + \int_{\Gamma_i} \mathbf{w}_f \cdot \hat{\mathbf{f}}_f\, d\Gamma_i
\end{aligned} \tag{3.15}$$

$$\int_{\Omega_f} \mathbf{q}_f (\boldsymbol{\nabla}\cdot\delta\mathbf{v}_f)\, d\Omega_f = -\int_{\Omega_f} \mathbf{q}_f (\boldsymbol{\nabla}\cdot\hat{\mathbf{v}}_f)\, d\Omega_f \tag{3.16}$$

$$\begin{aligned}
&\int_{\Omega_s} \Delta t\, (\boldsymbol{\nabla}\mathbf{w}_s)^T : \left(\delta\boldsymbol{\tau}_s - (\boldsymbol{\nabla}\delta\mathbf{v}_s)^T \cdot \hat{\boldsymbol{\sigma}}_s\right)\, d\Omega_s - \int_{\Omega_s} \delta p \boldsymbol{\nabla}\cdot\mathbf{w}_s\, d\Omega_s + \\
&\quad - \int_{\Gamma_i} \mathbf{w}_s \cdot \delta\mathbf{f}_s\, d\Gamma_i = -\int_{\Omega_s} (\boldsymbol{\nabla}\mathbf{w}_s) : \hat{\boldsymbol{\sigma}}_s\, d\Omega_s + \int_{\Gamma_i} \mathbf{w}_s \cdot \hat{\boldsymbol{f}}_s\, d\Gamma_i
\end{aligned} \tag{3.17}$$

$$\int_{\Omega_s} q_s\, \Delta t\, (\boldsymbol{\nabla}\cdot\delta\mathbf{v}_s)\, d\Omega_s = -\int_{\Omega_s} q_s\, \frac{(\hat{J}-1)}{\hat{J}}\, d\Omega_s \tag{3.18}$$

$$\int_{\Gamma_s} \mathbf{w}_i \cdot (\delta\mathbf{v}_f - \delta\mathbf{v}_s)\, d\Gamma_s = -\int_{\Gamma_i} \mathbf{w}_i \cdot (\hat{\mathbf{v}}_f - \hat{\mathbf{v}}_s)\, d\Gamma_i \tag{3.19}$$

Temporal discretization of the Navier-Stokes equation (eq. 3.15) is achieved using an implicit Euler scheme, while the linearization of the convective term $\mathbf{v_f} \cdot \nabla\mathbf{v_f}$ is obtained using Newton's method including iterations during a time step.

The two dimensional representation of the aortic root shown in Figure 3.5 was discretized to a finite element mesh. Figure 3.6 shows the part of the mesh near the sinus cavity. The length of the inlet channel is 4H while the outlet channel is 10 times the height of the channel. In this figure the stiff leaflet is shown in closed position. The length of the leaflet is 1.07 H, so the leaflet in closed position is under an angle of approximately 22 degrees with the vertical. The thickness of the leaflet is 1 mm.

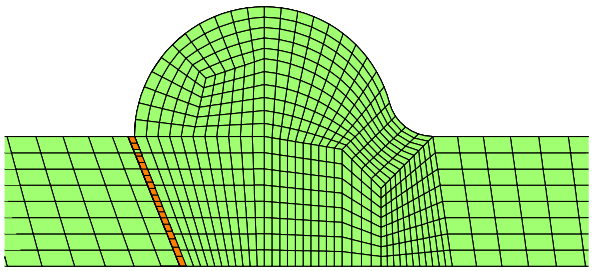

Figure 3.6: Section near the sinus cavity of the mesh used for the finite element computations. The valve leaflet, located in the transition from the inflow channel (left) to the sinus cavity, is shown in closed configuration and is represented by the darker elements

Galerkin's method is used for the spatial discretization, using 834 rectangular quadratic Crouzeix-Raviart elements. For the structure, spatial discretization is obtained using 19 rectangular quadratic Crouzeix-Raviart elements. The discretization of the Lagrange multiplier in equation (3.19) is chosen discontinuous, piecewise constant and coincides with the midpoints of the upstream edges of the solid elements of the leaflet. Gaussian integration was used to compute the integrals of the weak forms of the governing equations. The resulting system to be solved is given by:

$$\begin{pmatrix} \begin{bmatrix} \underline{K}_f^* & \underline{L}_f^T \\ \underline{L}_f & \underline{0} \end{bmatrix} & \begin{bmatrix} \\ \underline{0} \\ \\ \end{bmatrix} & \begin{bmatrix} \underline{C}_f^T \\ \underline{0} \end{bmatrix} \\ \begin{bmatrix} \\ \underline{0} \\ \\ \end{bmatrix} & \begin{bmatrix} \underline{K}_s^* & \underline{L}_s^T \\ \underline{L}_s & \underline{0} \end{bmatrix} & \begin{bmatrix} \underline{C}_s^T \\ \underline{0} \end{bmatrix} \\ \begin{bmatrix} \underline{C}_f & \underline{0} \end{bmatrix} & \begin{bmatrix} \underline{C}_s & \underline{0} \end{bmatrix} & \begin{bmatrix} \underline{0} \end{bmatrix} \end{pmatrix} \cdot \begin{pmatrix} \delta \underset{\sim}{v}_f \\ \delta \underset{\sim}{p}_f \\ \delta \underset{\sim}{v}_s \\ \delta \underset{\sim}{p}_s \\ \delta \underset{\sim}{f}_c \end{pmatrix} = \begin{pmatrix} \underset{\sim}{f}_f^v \\ \underset{\sim}{f}_f^p \\ \underset{\sim}{f}_s^v \\ \underset{\sim}{f}_s^p \\ \underset{\sim}{f}_c \end{pmatrix} \tag{3.20}$$

where $\underline{K}_f^*$ is the fluid matrix, $\underline{K}_s^*$ the solid matrix, $\underline{L}_f$ and $\underline{L}_s$ the divergence matrices for the fluid and solid phase, $\underline{C}_f$ and $\underline{C}_s$ the fluid and solid matrices concerning the coupling of the fluid and solid velocity. The variations in the estimates for the fluid velocity, solid velocity, fluid pressure, solid pressure and coupling force are represented by $\delta \underset{\sim}{v}_f$, $\delta \underset{\sim}{v}_s$, $\delta \underset{\sim}{p}_f$, $\delta \underset{\sim}{p}_s$ and $\delta \underset{\sim}{f}_c$ respectively. For more details on this subject and the definitions of the sub-matrices, the reader is referred to Appendix A of de Hart (2002), or van de Vosse *et al.* (2003). The linearized system is solved in a fully coupled manner using a direct solver.

3.3 Results

3.3.1 Fluid motion

Fluid velocity vector fields were measured in an *in-vitro* setup of the aortic root with a rigid valve in the sinus cavity, and simulated using the computational model, as

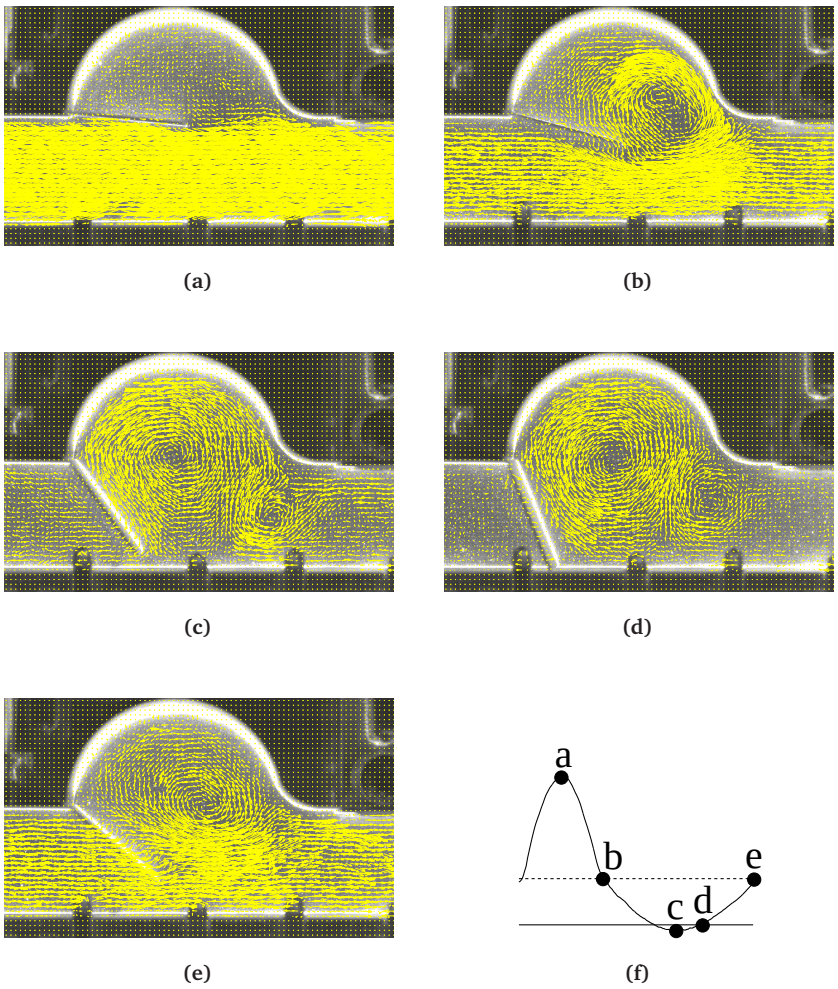

Figure 3.7: Measured velocity vector fields superimposed on the images captured by the PIV-camera for five instants of time in the flow cycle: (a) peak flow rate, (b) average flow rate in deceleration, (c) peak reversed flow rate, (d) end of back-flow and (e) average flow rate in acceleration. These instants are illustrated in the flow pulse (f); Re = 750 and Sr = 0.055

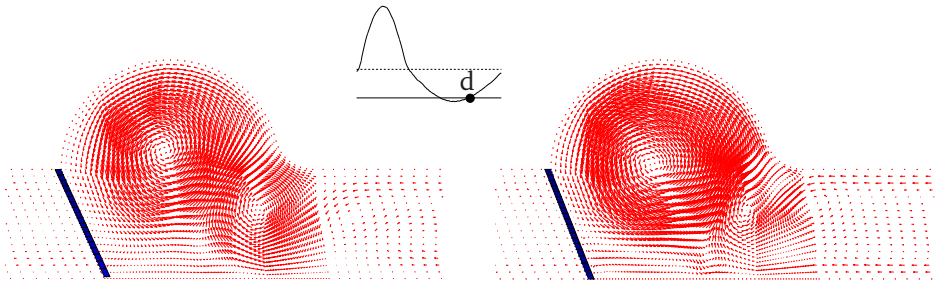

(a) Re=750, Sr=0.055 **(b)** Re=3000, Sr=0.055

Figure 3.8: Computational result at the end of back-flow (indicated as instant of time d in the flow curve), showing the velocity field at the moment that the valve is almost completely closed. The Strouhal number in these simulations is 0.055 with Reynolds numbers of 750 (a) and 3000 (b).

described in the previous section. Figure 3.7 shows the velocity fields as obtained by the PIV-measurements at five instants in time in the flow cycle, as indicated in panel (f), for a Reynolds number of 750 and a Strouhal number of 0.055. Panel (a) shows the velocity field for peak flow rate. Closer examination reveals that the fluid velocity in the entire channel can be described as a plug flow in the center with a boundary layer near the top and the bottom walls of the channel (see also Figure 3.9). In the sinus cavity a very weak vortex is present downstream the tip of the valve leaflet. In panel (b), the deceleration of the fluid has initiated the development of a large vortex in the sinus cavity. Further in the flow pulse, the flow changes direction and back-flow occurs. This reversed flow is necessary for the valve to reach its closed position. In panel (c) the reversed flow has reached its maximum value. The large vortex in the sinus cavity has grown and now fills the entire cavity. Downstream the large vortex, a second vortex has developed which is much smaller and rotates in the opposite direction. The fluid motion at the end of the back-flow period is shown in panel (d). The two vortices are still present and the secondary vortex has increased slightly in size.

Because of the settings of the flow pulse, the valve has now just reached its closed position. The fluid now accelerates further to the mean value of the cyclic flow rate, for which the velocity field is shown in panel (e). The velocity in the in- and outflow channel is increased and the large vortex in the cavity is being suppressed. The secondary vortex has already diminished.

Figure 3.8 shows the computational results at the end of back-flow (indicated as instant of time d in the flow curve, see also Fig. 3.7 (f)), at the moment the valve is almost completely closed. Panel (a) shows the results of the simulation with Reynolds and Strouhal numbers being 750 and 0.055 respectively. In agreement with the experiments (Figure 3.7 (d)), a large vortex has formed in the sinus cavity, downstream

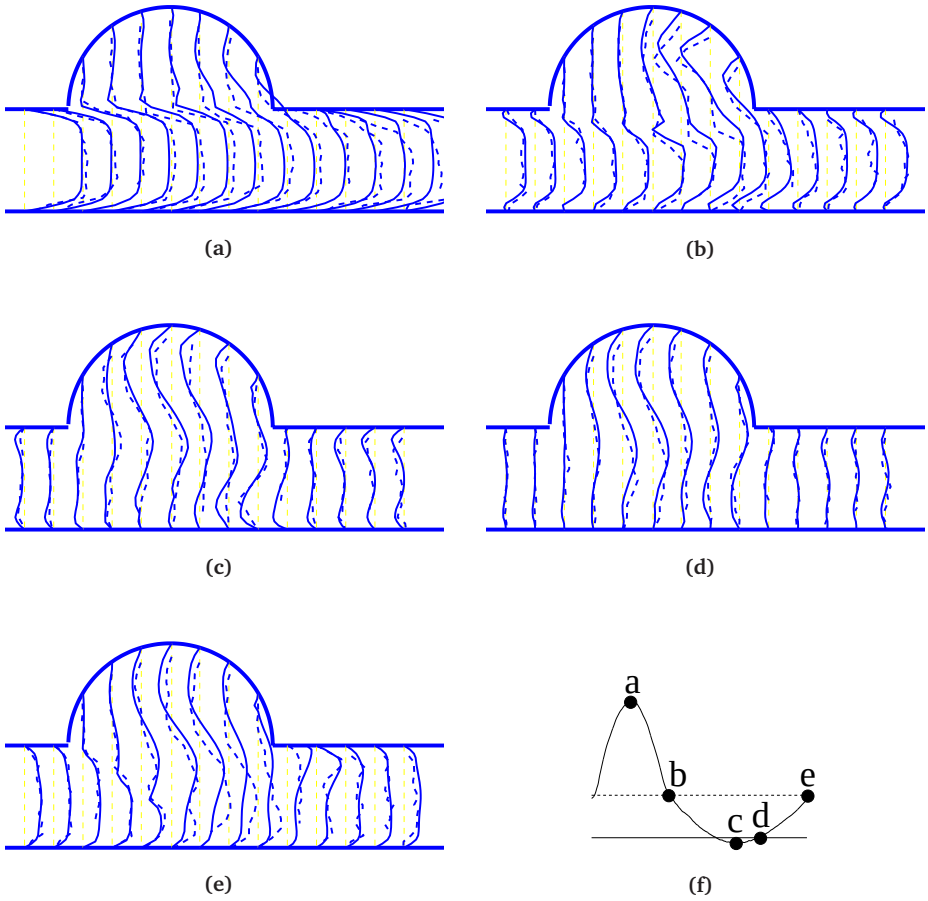

Figure 3.9: Interpolated horizontal velocity components at several cross sections of the channel at five points in the flow cycle; peak flow (a), average flow rate in deceleration (b), maximum reversed flow rate (c), end of reversed flow (d) and mean flow rate during acceleration (e). The computations are represented by the solid lines, the experiments by the dashed lines; Re = 750 and Sr = 0.055.

of which a smaller counter-rotating vortex has formed. Panel (b) shows the result at the same instant in the flow pulse as in panel (a), but now for a Reynolds number of 3000. Note that the main flow characteristics are similar, though the strength of the large vortex is increased, the secondary vortex is located slightly further upstream and the instationary boundary layer flow near the top and bottom of the outflow channel is more pronounced.

Quantitative comparison of the experimental and computational velocity fields is given in Figure 3.9. Hereto, the horizontal components of both flow fields were interpolated to several cross sections in the channel. The interpolations shown in Figure (3.9) are given for the same five instants in the flow cycle as in Figure (3.7).

Generally, the computed velocity field matches the experiments quite well. However, apart from local differences as a result of measurement and computational inaccuracies, there are some striking global differences. During the entire cycle, the computed vortex in the cavity is more pronounced and located slightly lower than the experimentally observed vortex. During the deceleration of the fluid (b) and just beyond (c), in the boundary layers near the top and bottom walls of the channel, reversed flow occurs due to the instationary nature of the flow. These kind of Womersley profiles are not detected well by the PIV measurements. Furthermore, during acceleration (subfigure (e)) the measured velocity below and downstream the tip of the valve is higher than predicted by the computational method.

3.3.2 Valve Motion

The motion of the valve is expressed in terms of the time-course of the opening angle of the valve, defined as the angle between the valve leaflet and the vertical (see Figure 3.5). Figure 3.10 shows a graph of the normalized average inflow velocity and opening angle of the valve for the entire flow cycle, measured from the camera images.

The flow pulse is normalized with the maximum flow rate (Q/Q_{max}) and divided by the cross-section area to obtain the normalized average inflow velocity (V/V_{max}), while the opening angle of the valve is normalized by dividing the difference between the opening angle of the valve and the closed angle by the range of the opening angle: $(\alpha - \alpha_{min})/(\alpha_{max} - \alpha_{min})$.

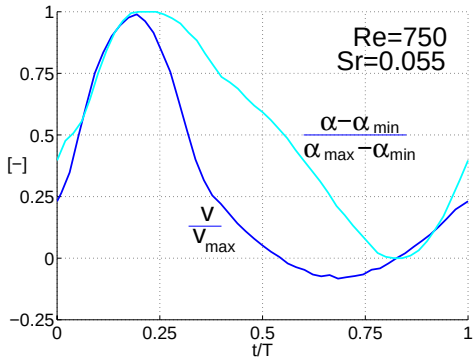

Figure 3.10: Experiment: normalized measured fluid velocity (v/v_{max}) and normalized valve opening angle ($(\alpha - \alpha_{min})/(\alpha_{max} - \alpha_{min})$) as a function of the cycle time (t/T).

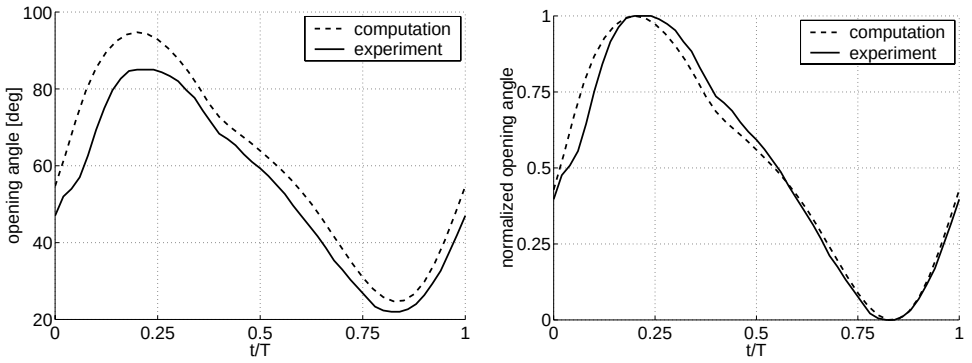

Figure 3.11: Valve opening angles (a) observed in the experiments (solid line) and computational prediction (dashed line). Normalized curves are shown in (b).

The curves in Figure 3.10 show that during acceleration of the fluid, the opening angle of the valve increases. The valve reaches its maximum opening angle just after peak flow rate. During early deceleration the valve opening angle starts to decrease, while the flow upstream the valve is still directed forward. The closing motion of the valve is approximately linear in time. In order to close the valve a small amount of back-flow (regurgitation) was necessary. At the end of the back-flow the valve is closed, which is shown in Figure 3.10 where the curves of the fluid inflow velocity and the normalized opening angle cross the zero line and each other.

Figure 3.11 (a) shows the experimentally observed and computationally predicted opening angle of the valve. The computed angles exceed the measured ones during the entire cycle. This is most pronounced near the maximum opening angle and least near the closed position. Note that the valve is closed at an angle of 22^o. The timing of the computed valve motion closely matches the experimentally observed pattern, which is better visible in Figure 3.11 (b) where both curves are normalized. Furthermore, the experimentally observed opening angle slightly lags behind the computationally predicted values for high fluid accelerations.

3.3.3 Dependence of valve motion on flow conditions

In order to study to what extent the valve motion is influenced by the characteristics of the flow pulse, the experiment was performed under several flow conditions as presented in Table 3.1. Figure 3.12 (a) shows the average velocity over the inflow area during a cycle for each flow case. The difference in period time is clear, as is the lower maximum flow rate for Reynolds equal to 500. For each flow case a different

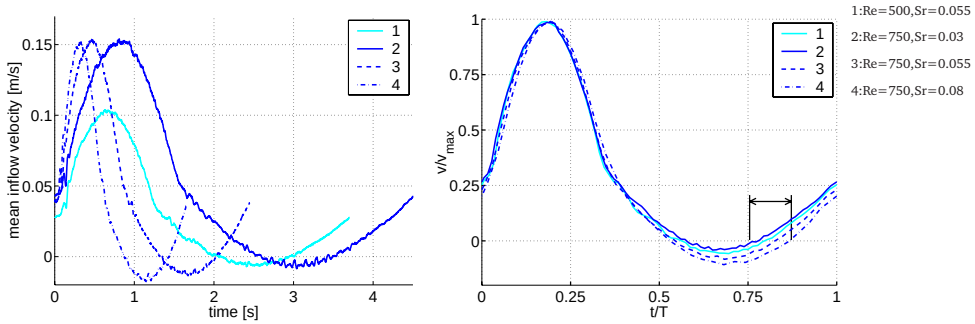

(a) **(b)**

Figure 3.12: Average inflow velocity derived from measurements of the applied flow pulses versus time for each flow case (a) and normalized velocity versus normalized time (b). The curves in panel (b) show that the maximum reversed flow-rate and the end of back-flow are different for each flow case.

amount of back-flow was necessary to close the valve. Figure 3.12 (b) shows the same data, normalized by the period time and peak velocity. Since the valve is closed when the velocity curve rises through zero, this figure shows that the moment of valve closure was different for each case (see arrow in 3.12 (b)).

Figure 3.13 shows the relative amount of back-flow with respect to the amount of forward flow $Q_{reversed}/Q_{forward}$ for each flow condition, both for the experiments and the computations. It is shown that for increasing the Reynolds number from 500

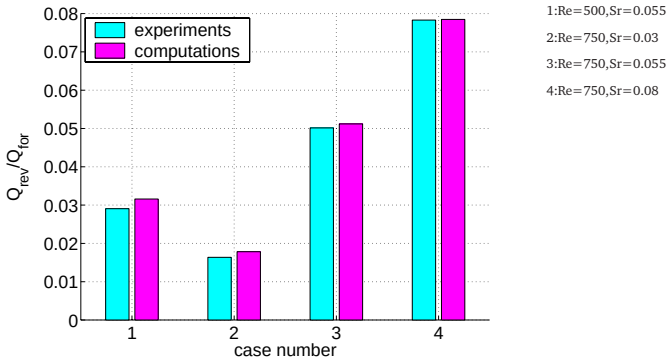

Figure 3.13: Back-flow divided by forward flow of measured flow curves (light bars) and flow pulses applied to the computational model (dark bars).

to 750 (by increasing the velocity V), while keeping the Strouhal number at 0.08 (by keeping TV constant), the amount of back-flow increases with respect to the amount of forward flow. The same occurs when the Strouhal number is increased (by decreasing the period time T), while keeping the Reynolds number at 750. Due to the noise on the flow measurement, the relative amount of back-flow is not exactly the same as applied to the computational model.

Figure 3.14 shows that, for every flow condition, the valve reaches its closed position at the end of back-flow phase. Furthermore, it shows that for increasing either the Strouhal number (decreasing T) or the Reynolds number (increasing V and keeping TV constant) the valve reaches its closed position later in the flow cycle, as predetermined by the flow pulse applied, and also that the valve reaches its maximum opening angle later for increasing either the Reynolds or the Strouhal number within the range applied.

The instant of time of valve closure in the flow cycle is clarified in the bar plot of Figure 3.15 (a). In this figure the left bar of each set shows the experimentally obtained moment at which the valve is closed, measured from the start of the flow pulse as shown in Figure 3.12 (b) for each case. The range (n=3) of the time of valve closure is given by the error bars. In the same way, panel (b) of Figure 3.15 shows the duration of valve opening, from closed to opened position. The experimentally observed duration of valve opening increases for increasing Strouhal number or de-

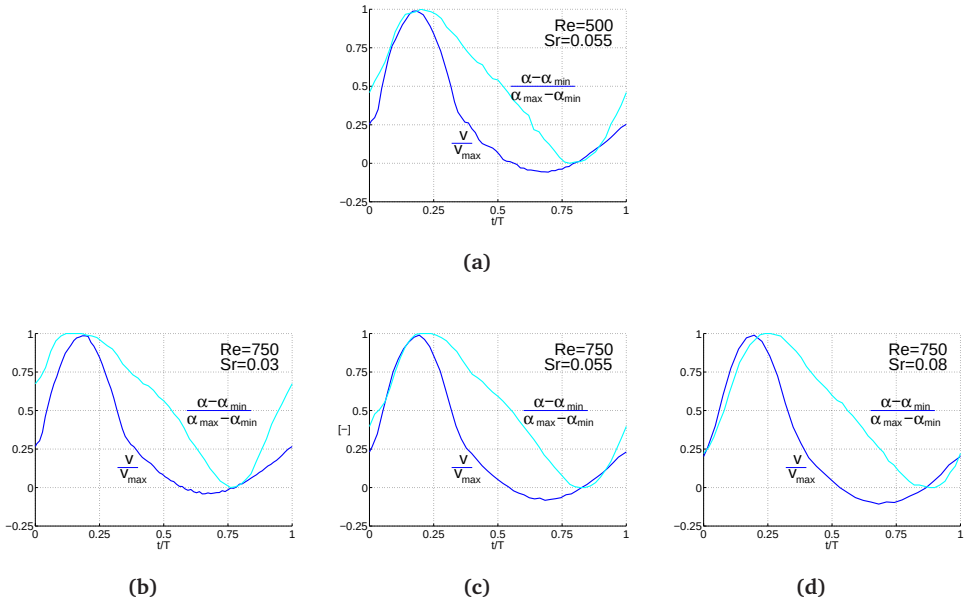

Figure 3.14: Measured normalized inflow velocity and normalized opening angle for each flow case.

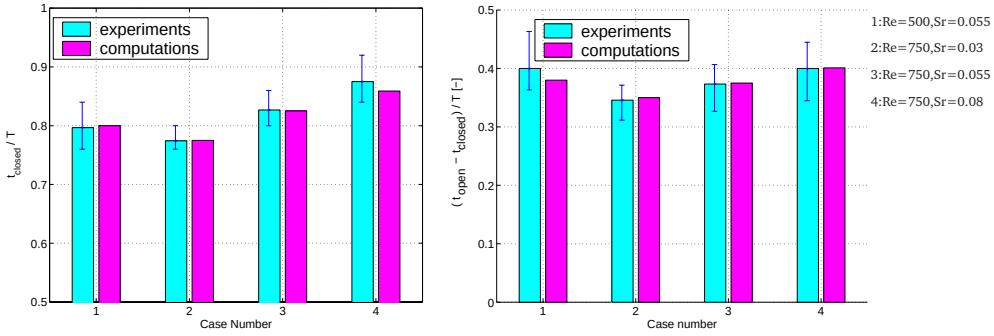

(a) **(b)**

Figure 3.15: Time of smallest valve opening angle (a) and duration of opening motion of the valve (b) for each case. Experimental data in light bars with error bar giving data range (n=3), computational data in dark bars.

creasing Reynolds number, although not significantly.

The right bars of Figure 3.15 (a) and (b) show the predictions for the time of minimum opening angle and the duration of the opening motion of the valve with the computational model. The prediction of the moment in the flow pulse at which the opening angle is minimal matches the experimentally observed values. The difference between the two is maximal for case 4, but still lies within the range of experimental data. In the computational model, the same trend is found for the duration of the opening motion of the valve. The maximum difference in opening is seen in case 1 (the low Reynolds number case), which also lies within the range of the experimental data.

3.4 Discussion

In an experimental setup of the aortic valve, fluid and valve motion were recorded by the camera of a Particle Image Velocimetry system. Instantaneous fluid velocity fields were derived by correlating average particle displacement within interrogation areas of subsequent camera images, under the assumption of small velocity gradients in the interrogation area. This condition is fulfilled in the major part of the measurement section. However, the instationary boundary layers developing near the top and bottom walls of the in- and outflow channel during deceleration are not well detected by the PIV method, since these velocity structures are too small for the interrogation areas. This can be solved by increasing the resolution of the camera, or decreasing the field of view combined with the use of smaller seeding particles.

A two-dimensional finite element model of the experiment is developed, in which fluid-structure interaction is modeled by means of a fictitious domain method, as de-

scribed in Glowinski *et al.* (1994); Bertrand *et al.* (1997), but formulated in terms of a locally acting volume force. The system matrix, arising after discretization of the governing equations of the solid and the fluid, is ill-conditioned. The eigenvalues of the matrix are related to the stiffness of the solid and the viscosity of the fluid, which differ several orders of magnitude. Nonetheless, no stability problems occurred in solving the set of equations.

The experimental results showed the development of a large vortex in the sinus cavity during fluid deceleration. Further downstream a secondary counter-rotating vortex develops. During acceleration, these vortices diminish. These phenomena are also found using a flexible valve leaflet, as reported in de Hart *et al.* (2000). The valve opens due to the forward flow pulse in the inflow channel during acceleration. In agreement with previous observations (van Steenhoven and van Dongen, 1979) the vortex in the sinus cavity initiates valve closure in early deceleration, even though the inflow velocity is still directed forward. A certain amount of regurgitation is necessary to close the valve completely. The computational results correctly predict the main characteristics of fluid and valve motion. Computed timing of valve motion, in terms of minimum opening angle and duration of valve opening, lies within the experimental range. However, the computationally predicted valve opening angle exceeds the angle observed in the experiments. This mismatch increases during fluid acceleration. A possible explanation for this effect is that in the experiments the valve motion is hampered by the boundary layer flow near the side walls of the setup. This effect is not present in the two-dimensional computational model. Furthermore, since the valve is fixed to the top of the inflow channel using three strips of adhesive tape, a small amount of fluid can leak over the top of the valve between the strips of tape. When the valve is closed and the fluid starts to move forward, the fluid passing underneath the valve will push the valve open. Since some of the fluid will leak over the valve, the valve will possibly not open as far as without the leakage.

In the entire region, the measured and computed flow patterns match very well. The slight differences are probably caused by the difference in valve motion. As the valve opening angle is larger in the computations, the large vortex in the sinus cavity will be more near the top of the cavity. During acceleration in the experiments, the fluid has to squeeze through a smaller opening due to the smaller opening angle of the valve. Since the same amount of fluid is entering the cavity, the fluid velocity underneath the valve tip is higher than in the computational results.

An other possible source for the discrepancy between computational and experimental results can be sought in the fact that fluid-structure interaction was taken into account at the upstream side of the valve only. It was assumed that this approximation is allowed as the valve is thin compared to the flow structures. Moreover, during most of the acceleration and deceleration, the direction of flow is perpendicular to the valve surface, which is not likely to cause a deviation in the opening angle of the valve. Refining the fluid mesh to element sizes smaller than the thickness of the valve leaflet will enable the coupling of fluid and valve velocity at both the up- and downstream side of the valve. In this way, the error made by coupling at the upstream side only could be determined. It will, however, require a substantial increase in CPU-time.

Four cases with different inflow characteristics were applied to both the experimental and the computational model. Experiments showed that the duration and maximum value of back-flow, necessary to close the valve, was different for each case. This means, since the shape of the pulse is fixed, that valve closure occurs at different instants in time in the flow cycle. The development of vortices in the cavity during deceleration is influenced by changing the Strouhal or Reynolds number of the inflow. The valve leaflet interacts with these vortices and therefore the valve motion is influenced by the characteristics of the inflow condition. The experimental results showed that there is a weak trend of increasing duration of valve opening for increasing Strouhal number or decreasing Reynolds number. The same trend is observed in the computational results. However, taking into account the range in experimental data, this trend is not statistically significant.

In the model by Horsten (1990) the valve motion was modeled using an ALE-method. The method does not allow the valve to fully close, since the fluid elements between the wall and the leaflet will be compressed. This is not a problem for the fictitious domain method, nor for the Immersed Boundary method by Peskin and McQueen (1995). The method by Peskin and McQueen (1995) was not applied for physiological Reynolds numbers due to numerical stability problems. In order to obtain numerical stability the viscosity was increased by a factor 25, resulting in a Reynolds number of 80. With the computational model presented in this work, no stability problems occurred for simulations with Reynolds numbers up to the physiologically relevant value of 3000. However, the experimental setup did not allow validation of the simulations with Reynolds and Strouhal numbers within this physiological range. In order to apply the present method to a valve in the heart, the closed valve will have to be able to carry the pressure difference between the ventricle and the aorta or the atrium. This situation could not be simulated with the experimental setup and will need further investigation.
Computations in three-dimensional geometries will enable studies to more realistic situations. For flexible valves, extension of the method to three dimensions is straightforward, as shown by de Hart *et al.* (2003).

From the results it may be concluded that the fictitious domain method was successfully applied for modeling rigid heart valve motion. In the range of flow pulses applied to the experimental and the computational model, the sensitivity of the time dependent response of the valve to changes in the applied flow pulse was low (maximum deviation in duration of opening about 5% of the period time (see Figure 3.15)), but still well predicted by the computational method.

Bibliography

Baaijens, F. P. T. (2001). A fictitious domain/mortar element method for fluid-structure interaction. *International Journal for Numerical Methods in Fluids*, **35**, 743–761.

Baccani, B., Domenichini, F., and Pedrizzetti, G. (2003). Model and influence of mitral valve opening during the left ventricular filling. *Journal of Biomechanics*, **36**, 355–361.

Bertrand, F., Tanguy, P. A., and Thibault, F. (1997). A three-dimensional fictitious domain method for incompressible fluid flow problems. *International Journal for Numerical Methods in Fluids*, **25**, 719–736.

Bluestein, D., Rambod, E., and Gharib, M. (2000). Vortex shedding as a mechanism for free emboli formation in mechanical heart valves. *Journal of Biomechanical Engineering*, **122**, 125–134.

Bluestein, D., Li, Y. M., and Krukenkamp, I. B. (2002). Free emboli formation in the wake of bi-leaflet mechanical heart valves and the effects of implantation techniques. *Journal of Biomechanics*, **35**, 1533–1540.

Cape, E. G., Sung, H., and Yoganathan, A. P. (1996). Hemodynamica assessment of carbomedics bileaflet heart valves by ultrasound: Studies in the aortic and mitral positions. *Ultrasound in Medicine & Biology*, **22**, 421–430.

Chandran, K. B., Shoephoerster, R., and Dellsperger, K. C. (1989). Effect of prosthetic mitral valve geometry and orientation on flow dynamics in a model human left ventricle. *Journal of Biomechanics*, **22**, 51–65.

de Hart, J. (2002). *Fluid-Stucture interaction in the aortic heart valve*. Ph-D thesis, Eindhoven University of Technology.

de Hart, J., Peters, G. W. M., Schreurs, P. J. G., and Baaijens, F. P. T. (2000). A two-dimensional fluid-structure interaction model of the aortic valve. *Journal of Biomechanics*, **33**, 1079–1088.

de Hart, J., Peters, G. W. M., Schreurs, P. J. G., and Baaijens, F. P. T. (2003). A three-dimensional computational analysis of fluid-structure interaction in the aortic valve. *Journal of Biomechanics*, **36**, 103–112.

Fatemi, R. and Chandran, K. B. (1989). An in vitro comparative study of St. Jude Medical and Edwards-Duromedics bileaflet valves using laser anemometry. *Journal of Biomechanical Engineering*, **111**, 298–302.

Garitey, V., Gandelheid, T., Fusezi, J., Pelissier, R., and Rieu, R. (1995). Ventricular flow dynamic past bileaflet prosthetic heart valves. *Int. J. Artificial Organs*, **18**, 380–391.

Glowinski, R., Pan, T. W., and Periaux, J. (1994). A fictitious domain method for dirichlet problem and applications. *Computer Methods in Applied Mechanics and Engineering*, **111**, 283–303.

Grigioni, M., Daniele, C., D'Avenio, G., and Barbaro, V. (2001). The influence of the leaflets' curvature on the flow field in two bileaflet prosthetic heart valves. *Journal of Biomechanics*, **34**, 613–621.

Horsten, J. B. A. M. (1990). *On the analysis of moving heart valves: a numerical fluid-structure interaction model*. Ph-D thesis, Eindhoven University of Technology.

Kilner, P. J., Yang, G. Z., Wilkes, A. J., Mohiaddin, R. H., Firmin, D. N., and Yacoub, M. H. (2000). Asymmetric redirection of flow through the heart. *Nature*, **404**, 759–761.

King, M. J., Corden, J., David, T., and Fisher, J. (1996). A three-dimensional, time-dependent analysis of flow through a bileaflet mechanical heart valve: comparison of experimental and numerical results. *Journal of Biomechanics*, **29(5)**, 609–618.

Krafczyk, M., Cerrolaza, M., Schulz, M., and Rank, E. (1998). Analysis of 3d transient blood flow passing through an artificial aortic valve by lattice-boltzmann methods. *Journal of Biomechanics*, **31**, 453–462.

Kwak, D. Y. and Im, Y. T. (2003). Hexahedral mesh generation for remeshing in three-dimensional metal forming analyses. *Journal of Materials Processing Technology*, **6691**, 1–7.

Lemmon, J. D. and Yoganathan, A. P. (2000). Three-dimensional computational model of left heart diastolic function with fluid-structure interaction. *Journal of Biomechanical Engineering*, **122**, 109–117.

Lim, W. L., Chew, Y. T., Chew, T. C., and Low, H. T. (2001). Pulsatile flow studies of a procine bioprosthetic aortic valve in vitro: PIV measurements and shear-induced blood damage. *Journal of Biomechanics*, **34**, 1417–1427.

Patankar, S. V. (1983). *Numerical heat transfer and fluid flow*. Hemisphere Publishing Corporation, McGraw-Hill, New York.

Peskin, C. S. (1972). Flow patterns around heart valves: a numerical method. *Journal of Computational Physics*, **10**, 252–271.

Peskin, C. S. and McQueen, D. M. (1995). A general method for the computer simulation of biological systems interacting with fluid. *Society for Experimental Biology*, **49**, 265–276.

Pop, G., Sutherland, G. R., Roelandt, J., Vletter, W., and Bos, E. (1989). What is the ideal orientation of a mitral disc prosthesis? an in vivo haemodynamic study based on colour flow imaging and continuous wave doppler. *European Heart Journal*, **10**, 346–353.

Reul, H., Talukder, N., and Muller, E. W. (1981). Fluid mechanics of the natural mitral valve. *Journal of Biomechanics*, **14(5)**, 361–372.

van de Vosse, F. N., de Hart, J., van Oijen, C. H. G. A., Bessems, D., Gunther, T. W. M., Segal, A., Wolters, B. J. B. M., Stijnen, J. M. A., and Baaijens, F. P. T. (2003). Finite-element based computational methods for cardiovascular fluid-structure interaction. *Journal of Engineering Mathematics*, **47**, 335–368.

van Steenhoven, A. A. and van Dongen, M. E. H. (1979). Model studies of the closing behaviour of the aortic valve. *Journal of Fluid Mechanics*, **90(1)**, 21–32.

Vierendeels, J. A., Riemslagh, K., Dick, E., and Verdonck, P. R. (2000). Computer simulation of intraventricular flow and pressure gradients during diastole. *Journal of Biomechanical Engineering*, **122**, 667–674.

Vlachos, P. P., Pierrakkos, O., Phillips, A., and Telionis, D. P. (2001). Vorticity and turbulence characteristics inside a transparent flexible left ventricle. *Proceedings of the 2001 ASME Bioengineering Conference*, **BED-Vol.50**, 493–495.

Walker, P. G., Cranney, G. B., Grimes, R. Y., Delatore, J., Rectenwald, J., Phost, G. M., and Yoganathan, A. P. (1996). Three-dimensional reconstruction of the flow in a human left heart by using magnetic resonance phase velocity encoding. *Journal of Biomedical Engineering*, **24**, 139–147.

Westerweel, J. (1993). *Digital Particle Image Velocimetry, Theory and Application*. Ph-D thesis, Delft University of Technology.

Willert, C. E. and Gharib, M. (1991). Digital particle image velocimetry. *Experiments in Fluids*, **10**, 181–193.

Chapter 4

Analysis of ventricular pump efficiency using a computational two-valve flow model: Influence of flow conditions

Abstract

Apart from dependence on the heart muscle contractility, the pump efficiency of the heart depends on the efficiency of the functioning of its valves. Valve efficiency, expressed as 1 minus the ratio between regurgitant and stroke volume, is the result of the motion of the valve, which in turn depends on the motion of the surrounding blood, and on the dynamics of the other valve in the same ventricle. In this work, the relation between valve efficiency and flow conditions is studied in a two dimensional computational model of the left ventricle with two valves. It is found that valve efficiency is non-periodic. Also, with increasing Strouhal number aortic valve efficiency decreases while mitral valve efficiency increases, an effect that is attributed to the decreasing size of the ventricular vortices with increasing Strouhal number. Valve efficiency is found to be relatively insensitive to variations in the Reynolds number. For the two dimensional model considered in this study, a change in flow conditions from Re=1200, Sr = 0.04 to Re = 2400, Sr=0.12 significantly decreases the ventricular pumping efficiency.

4.1 Introduction

The four valves of the heart enable the ventricles to fill with blood from the atria, and to eject blood into the aorta and the pulmonary artery. Due to valvular disease the condition of a valve can deteriorate which, for example, can obstruct a valve in opening or closing properly (stenosis) and may also cause leakage of the not fully closed valve (regurgitation). In some cases, the function of a valve is compromised to the extent that valve replacement is desired.

The haemodynamic performance of the different types of mechanical prostheses is not as good as that of the natural valves. This is reflected in terms of increased trans-valvular pressure gradients in opened position, increased back-flow during valve closure (regurgitation) or increased shear stresses causing damage to the blood platelets (Chandran *et al.*, 1989). These phenomena depend on the properties and the design of the prosthetic valves.

The performance of a valve is the result of its interaction with the surrounding blood flow during the cardiac cycle. Valve performance has been the topic of many studies, both experimental and numerical (see references in Stijnen *et al.* (2004)). These studies assessed flow patterns downstream prosthetic valve designs in several positions and orientations, trans-valvular pressure gradients in opened state, back-flow during valve closure, shear stresses on valve surfaces and the influence of the geometry of the valve environment on the performance of the valve.

To the best of our knowledge, none of these studies focused on the interaction between valves, as mediated by the surrounding fluid. Nevertheless, in each cardiac ventricle two valves function in close vicinity of each other. We hypothesize that, dependent on flow characteristics, the opening and closing behavior of one valve will affect the motion of the other valve.

The objective of this work is to investigate to what extent flow patterns in the left ventricle may influence the interaction between the mitral and aortic valve, and thus the pump function of the left ventricle. To this end, we simulated fluid and valve dynamics in a geometrically simplified two dimensional two-valve model of the left ventricle. We used a fictitious domain method (Glowinski *et al.*, 1994; Bertrand *et al.*, 1997; Baaijens, 2001; van de Vosse *et al.*, 2003) to account for the interaction of the mitral and aortic valve leaflets with the fluid entering and leaving the ventricle during the complete cardiac cycle.

4.2 Method

4.2.1 Geometry of the model

The cooperation of the two valves to direct fluid from the atrium to the aorta is studied in the two dimensional geometry shown in Figure 4.1. The ventricular cavity is modeled as a rectangular domain with a rectangular inflow channel at the top right of the ventricle, representing the atrium, and a rectangular outflow channel at the top left, representing the aorta. Valves are positioned in the transitions from the in-

and outflow channel to the ventricle. The in- and outflow channels have a width D and a length H_c of 10 D (Figure 4.1). The mitral and aortic channel are separated by half a circle with a radius R of 0.2 D. Thus, the width of the ventricular cavity is 2.4 D. The ventricular cavity has a length H_v of 5 D. The fluid domain, denoted by Ω_f, is enclosed by boundaries Γ_w, Γ_p, Γ_i and Γ_o. The solid domains of the mitral valve and the aortic valve are denoted by Ω_m and Ω_a and their boundaries are Γ_m and Γ_a, respectively.

4.2.2 Fluid flow

Assuming the fluid to be laminar, incompressible and Newtonian, its motion is governed by the Navier-Stokes equations, completed with appropriate boundary and initial conditions. At the boundaries Γ_w, no-slip boundary conditions are applied.

At boundary Γ_p at the bottom of the ventricular cavity a sinusoidal plug velocity

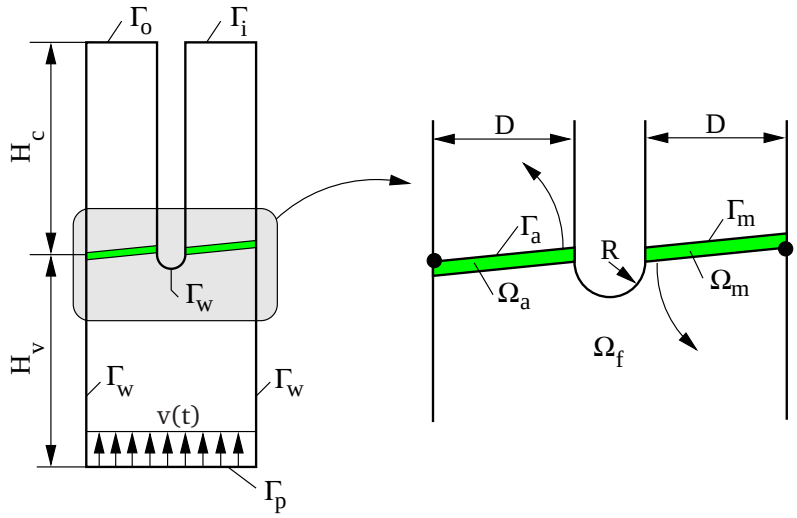

Figure 4.1: Schematic representation of the geometry, consisting of a rectangular ventricle with height H_v, in- and outflow channels with height H_c and width D representing the atrium and the aorta, and the mitral and aortic valves which can rotate around the corner points (denoted by the dots) in the direction of the arrows. The fluid domain Ω_f is enclosed by boundaries Γ_w, Γ_p, Γ_i and Γ_o. At the bottom of the ventricle (Γ_p) a pulsatile plug flow v(t) is prescribed. The boundaries of the structural domains of the mitral valve (Ω_m) and the aortic valve (Ω_a) are denoted by Γ_m and Γ_a. The in- and outflow channels are separated by a half circle with radius R.

profile v(t) is prescribed:

$$v(t) = V_p \sin\left(\frac{2\,\pi\,t}{T}\right) \tag{4.1}$$

where V_p is the amplitude of the pulsatile velocity, t the time and T the period time of the cycle. Settings of V_p and T determine the flow conditions, which are characterized by the Reynolds and Strouhal numbers given by:

$$Re = \frac{\rho\,V\,D}{\eta}; \qquad Sr = \frac{D}{T\,V}; \qquad V = V_p\frac{2(D+R)}{D} \tag{4.2}$$

with V the average peak velocity in a cross section of the in- or outflow channel.

At the inflow boundary Γ_i and the outflow boundary Γ_o the tangential velocity component is set to zero and a constant normal component of the stress vector $\mathbf{n}_f \cdot \boldsymbol{\sigma}_f \cdot \mathbf{n}_f$ of P_i and P_o is prescribed respectively, with $P_o = 5\ P_i$. The pressure difference $P_o - P_i$ is chosen high compared to the pressure difference related to fluid acceleration: $P_o - P_i >> \rho V^2$. The influence of the valves on the fluid at the valve boundaries Γ_a and Γ_m is accounted for using a fictitious domain method (Glowinski *et al.*, 1994; Bertrand *et al.*, 1997; Baaijens, 2001).

At the start of the first cycle the velocity of the fluid is set to zero. In order to ensure similar initial conditions at the start of subsequent cycles, the flow in the in- and outflow channels is suppressed once the valve has closed. To this end, in the first ten time steps after valve closure the viscosity in the channel above a closed valve is gradually increased to three orders above the original viscosity. In this way, the flow patterns that potentially develop in the closed channels while the flow rate is zero are damped, and the interaction between the mitral and aortic valves will depend on ventricular flow patterns only.

4.2.3 Valve motion

The displacement of the valves is governed by the equations of motion, completed by initial and boundary conditions and a constitutive law for the valve material. The density of the valve leaflets is taken to be equal to the fluid density, allowing buoyancy forces to be neglected. Since the mass of the valve leaflets is negligible with respect to the mass of fluid flowing through the valve orifice, the inertia of the valve leaflets is not taken into account either.

At the start of the first cycle, the displacement of the valves is set to zero. The displacement of the hinge point of each leaflet is prescribed to be zero (see Figure 4.1) throughout the cycle. Free rotation around these points is allowed. Each leaflet is slightly longer than the width of the channel, such that from the closed position free rotation is possible in one direction only.

At the boundaries of the solid domains of the valves Γ_m and Γ_a, which are completely immersed in the fluid domain Ω_f, the velocity of the fluid and the solid is coupled:

$$\mathbf{v}_f = \mathbf{v}_s \qquad \text{on } \Gamma_m \text{ and } \Gamma_a \tag{4.3}$$

where $\mathbf{v}_f$ and $\mathbf{v}_s$ represent the fluid and solid velocity field, respectively. Furthermore, at these boundaries the stress exerted by the fluid on the leaflets is in equilibrium with the stress exerted by the leaflets on the fluid:

$$\boldsymbol{\sigma}_f \cdot \mathbf{n}_f = -\boldsymbol{\sigma}_{\text{sm}} \cdot \mathbf{n}_{\text{sm}} \qquad \text{on } \Gamma_m \qquad (4.4)$$

$$\boldsymbol{\sigma}_f \cdot \mathbf{n}_f = -\boldsymbol{\sigma}_{\text{sa}} \cdot \mathbf{n}_{\text{sa}} \qquad \text{on } \Gamma_a \qquad (4.5)$$

with $\mathbf{n}_{\text{sm}}$ and $\mathbf{n}_{\text{sa}}$ the outward normals of the solid domains of the mitral and aortic valve, respectively, and $\mathbf{n}_f$ the outward normal of the fluid domain, i.e. the opposite direction.

The valve leaflets are assumed to be incompressible and isotropic. Since the leaflets are subject to small strains, a physically linear constitutive model is used to describe the material behavior. To account for the large rotations of the leaflets, a geometrically non-linear model is used:

$$\boldsymbol{\sigma}_s = -p_s\,\mathbf{I} + \boldsymbol{\tau}_s; \qquad \boldsymbol{\tau}_s = \text{G}\,(\mathbf{B\text{-}I}) \qquad \text{in } \Omega_m \text{ and } \Omega_a \quad (4.6)$$

where p_s is the hydrostatic pressure in the solid leaflets, $\boldsymbol{\tau}_s$ the extra stress tensor and G the shear modulus. The left Cauchy-Green strain tensor $\mathbf{B}$ is defined as $\mathbf{B} = \mathbf{F} \cdot \mathbf{F}^T$, where $\mathbf{F}$ represents the deformation gradient tensor. The value of G is chosen such that the deformation of the stiff leaflets is negligible, i.e. $||\ \mathbf{B\text{-}I}\ || < 10^{-8}$.

4.2.4 Implementation of the computational method

The governing equations for the fluid and the valves are solved, each on their own computational grid. These grids are completely independent of each other and the valve grids can move arbitrarily through the fluid grid. As there is not necessarily a computational boundary of the fluid domain present at the location of the moving boundary of the valve leaflets, a fictitious domain method is used to account for the coupling of fluid and solid variables. These variables are coupled in the central points of the element edges along the outer boundary of the solid domain only (Stijnen *et al.*, 2004; van de Vosse *et al.*, 2003). Application of the coupling of the fluid and solid variables to only one side of the valve leaflets does not influence the fluid-structure interaction since the leaflets are thin compared to the size of the local geometry of the fluid domain (Baaijens, 2001; Stijnen *et al.*, 2004). It also reduces the number of coupling constraints per element which is beneficial to the stability of the solution (Stijnen *et al.*, 2004). Experimental validation of this method is given in earlier studies where the computed motion of a single valve in a pulsatile flow was compared to experimental results obtained using LDA (de Hart *et al.*, 2000) and DPIV (Stijnen *et al.*, 2004).

For the spatial discretization Galerkin's method is used, with 1224 rectangular quadratic Crouzeix-Raviart elements for the fluid and 20 rectangular quadratic Crouzeix-Raviart elements for each valve leaflet. Gaussian integration is used to compute the integrals of the weak forms of the governing equations. Temporal discretization of the Navier-Stokes equation is achieved using an implicit Euler scheme, while

the convective term is linearized using newton's method. The linearized system is solved in a fully coupled manner using a direct solver

Initially, the flow pulse is discretized in 512 time steps. Time step splitting is applied if convergence is not reached within 15 newton iterations. The time step is split in half, until convergence is reached. After convergence, the new time step is chosen to be the remainder of the split time step. When the end of the split time step is reached, time evolution proceeds with the initial time step. Time step splitting is also applied near the moment of valve closure: to prevent the valve from penetrating the wall at the end of the time step, time steps are split until a maximum penetration of 10^{-2} D is found.

To enable a closed valve to bear a pressure load the fluid-structure interaction interface of the closed valve is kept on an element edge of the fluid domain. As the Crouzeix-Raviart type fluid elements allow a discontinuous pressure across the element boundary, sub-elemental pressure gradients in the fluid elements are not affected by the pressure difference across the interface, circumventing spurious leakage of the valves.

Since the system is completely rigid, instant deceleration of the fluid mass inside the channel occurs immediately after valve closure leading to high pressure peaks in the in- and outflow channel, which compromise convergence of the solution. On one hand, the length of the channels should be small to reduce the mass of the impacting blood, and hence the pressure peak. On the other hand, the in- and outflow channels should be long enough to prevent the boundary conditions at the in- and outflow boundaries from interfering with the flow around the valves. The length of the atrial and aortic channels therefore is a compromise.

4.2.5 Simulations and data processing

Since this work focuses on the relation between the dynamic response of a two-valve system and the flow conditions applied, a range of pulsatile flow conditions is applied at Γ_p. This was done by changing the amplitude V_p and the period time T of the flow pulse in equation (4.1) around a reference simulation in the physiological range, characterized by a Reynolds number of 1800 and a Strouhal number of 0.08. Computations are performed for Reynolds numbers equal to 1200, 1800 and 2400 in combination with Strouhal numbers of 0.04, 0.08 and 0.12. For each flow condition 19 cycles are simulated, in order to obtain information about the periodicity of the system response.

The primary results of the computations are fluid and solid velocity fields, fluid pressure fields and valve positions. The back-flow during valve closure is derived straightforwardly from the fluid velocity fields. The efficiency of the ventricle as a pump is defined as the total stroke volume, applied at the bottom of the ventricle, minus the mitral and aortic regurgitant volumes, divided by the total stroke volume :

$$\text{Efficiency} = \frac{V_{stroke} - V_{mr} - V_{ar}}{V_{stroke}} \tag{4.7}$$

with V_{stroke} the stroke volume, V_{mr} the mitral regurgitant volume, V_{ar} the aortic re-

gurgitant volume.

4.3 Results

4.3.1 Fluid and valve dynamics in the reference situation

Simulations were performed in a ventricular analogue model as described in the previous section. Figure 4.2 shows the computed velocity fields and valve positions at eight instants in the flow cycle, at cycle number 9 for the reference situation (Re=1800, Sr=0.08).

Velocity field

At the beginning of the flow cycle, i.e. the onset of fluid ejection, an *upper ventricular inflow vortex* is present below the closed aortic valve. A weaker, *lower ventricular inflow vortex* is present below the tip of the opened mitral valve. The mean cross-sectional flow rate in the aortic and atrial channel is zero, and *instationary inflow boundary layers* are present near the walls of the atrial channel. Application of upward flow at the bottom of the cavity, initially causes the fluid to flow through the opened mitral valve, causing a *mitral back flow jet* (b). The closing motion of the mitral leaflet is hampered by the upper part of the *upper ventricular inflow vortex* below the aortic valve, which is directed towards the closing mitral valve. The mitral valve has closed before peak flow rate is reached (c). Opening of the aortic valve occurs very quickly, due to the high flow rate at this point in the flow cycle. The *mitral back flow jet* that originated from the *upper ventricular inflow vortex* is cut off by the closure of the mitral valve, and the flow is redirected into the opened aortic opening causing an *aortic outflow jet*. The *upper ventricular inflow vortex* that was located below the aortic valve is washed out into the aorta. In the deceleration phase of ejection (d), the aortic valve is fully opened, almost parallel to the flow of the *aortic outflow jet*. At the side walls of the aorta, *instationary outflow boundary layers* are present.

At the onset of the ventricular filling phase (e), the flow rate applied is zero. The aortic valve is starting to close due to the reversed flow in the *instationary outflow boundary layer* along the aortic wall. Near the wall opposite of the opened valve and further downstream in the aorta, several small *aortic outflow vortices* have developed. In the acceleration phase of ventricular filling (f), the fluid is sucked into the ventricle out of the aorta, causing *aortic back flow* and aortic valve closure. At peak flow rate (g), the aortic valve is closed and the mitral valve is opening. A *mitral inflow jet* is entering the ventricular cavity which is directed towards the left wall, due to the position of the mitral valve leaflet as well as the one-sided widening of the ventricle with respect to the atrial channel. At the end of the cycle, the fluid entering the ventricle is decelerating (h). The *mitral inflow jet* front has traveled towards the bottom of the ventricle, while a new large *upper ventricular inflow vortex* has developed below the closed aortic valve. A new smaller *lower ventricular inflow vortex* is starting to develop below the mitral valve tip. As the flow reduces further, the *mitral inflow jet* becomes weaker and the vortex increases in size (a).

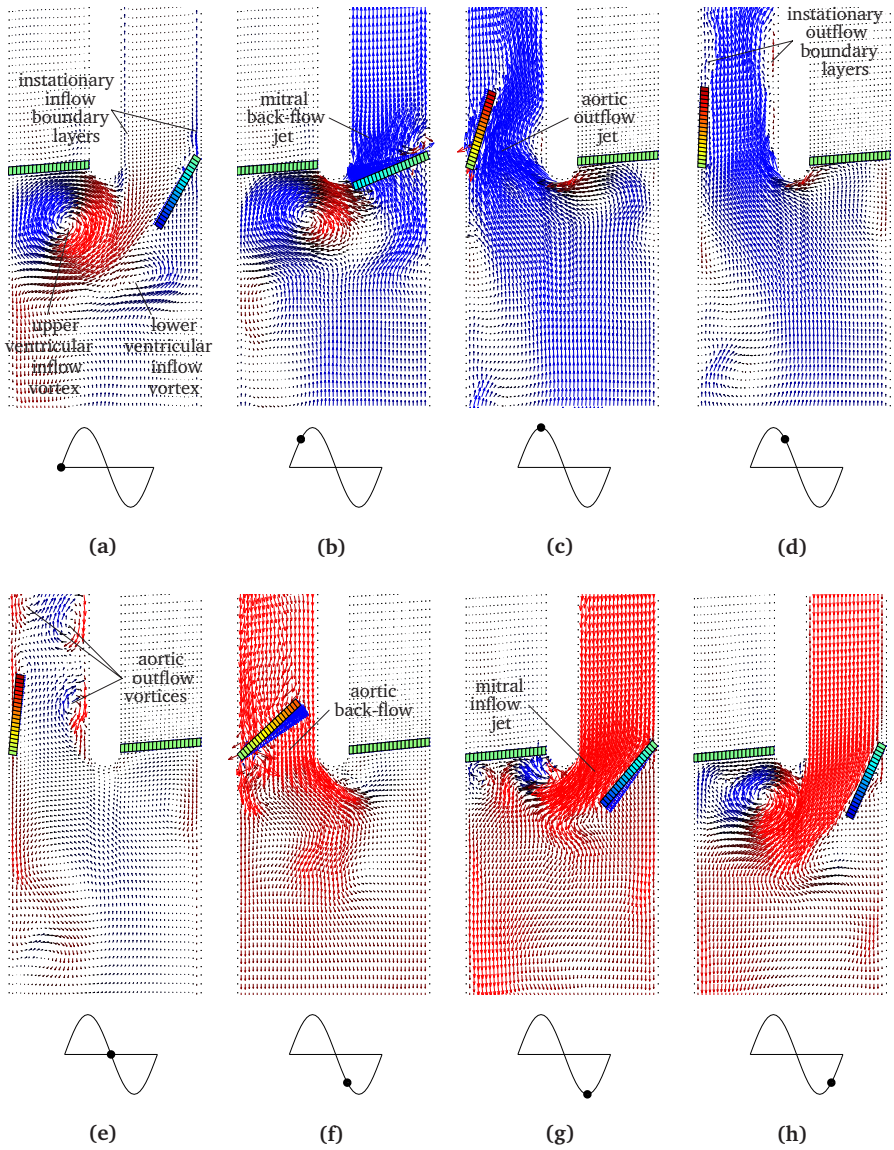

Figure 4.2: Simulation results of cycle 9 of the reference flow case (Re=1800, Sr=0.08), in the region of the valve base. Top row (a-d) shows flow patterns during ejection, progressing from early systole (a) to acceleration (b) to peak flow rate (c) to deceleration (d) as indicated by the dot in the flow pulse graphs below each vector field. For the filling phase the results are shown in the bottom row (e-f), the flow pulse advancing from early diastole (e) to acceleration (f) to peak flow rate (g) to deceleration (h).

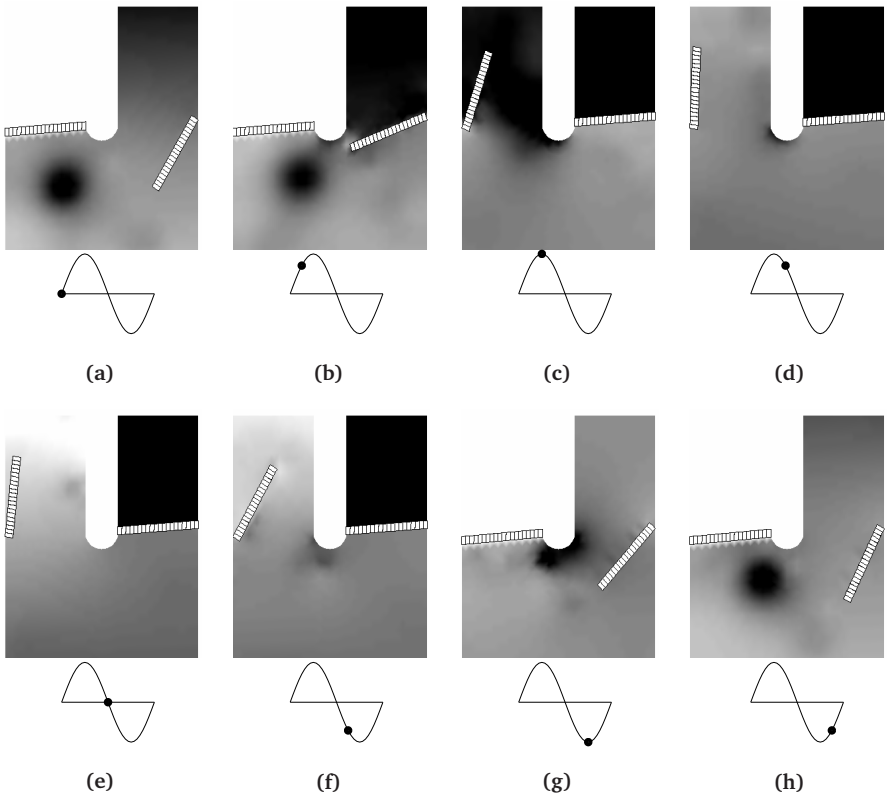

Figure 4.3: Normalized pressure $\frac{p}{\rho V^2}$ belonging to the velocity fields of Figure 4.2. The middle gray-scale value is adapted to the mean pressure in the area between the valve base and one valve diameter below. Higher pressures have a lighter gray value.

Pressure field

Figure 4.3 shows the normalized pressure distribution $\frac{p}{\rho V^2}$ belonging to the velocity fields shown in Figure 4.2, with V defined in equation 4.2. At the start of the ejection phase (a) the ventricular pressure is higher than the atrial pressure, initiating fluid ejection. In the center of the *upper ventricular inflow vortex*, shown in Figure 4.2 (a), the pressure is low. In panel (b) the fluid acceleration into the atrial tube causes an increased atrio-ventricular pressure gradient. The low pressure zone caused by the *upper ventricular inflow vortex* is still present. At peak flow rate (c) the mitral valve has closed, causing the ventricular pressure to rise above the aortic pressure due to which the aortic valve opens, and the fluid accelerates into the aorta. In panel (d) fluid deceleration is imposed, causing the pressure gradient between the ventricle

and aorta to change sign. The ventricular-aortic pressure gradient is smaller than in the previous panel. Toward the end of the ejection phase, fluid deceleration increases which is reflected in the increase in aortic pressure gradient from (d) to (e). During fluid acceleration in the filling phase (f-g) boundary layer separation occurs just below the circular wall between the mitral and aortic valve opening, which is accompanied by a low pressure zone in this region. As a result of this low pressure zone, the fluid entering through the aortic valve opening (*aortic back flow*)(f), and later (g) through the mitral valve opening (*mitral inflow jet*) is diverted around the corner, towards the center of the ventricular cavity. In the deceleration phase (h), the *upper ventricular inflow vortex* develops, causing the low pressure area below the closed aortic valve. The pressure gradient in the *upper ventricular inflow vortex* is large compared to that in all other vortices.

Valve efficiency

In Figures 4.4 (a) and (b), the detailed view of Figure 4.2 is condensed into the development in time of the mean cross-sectional velocity in the in- and outflow channel (a) and the opening angle of the aortic and mitral valves (b) for cycles 10 through 15. The envelop of the velocity curve is determined by the velocity, imposed at the bottom of the ventricle, with positive velocity during ejection and negative velocity during filling. At the beginning of the ejection phase, the ventricle empties through the mitral valve. The mitral regurgitation, i.e. the back flow volume before mitral valve closure, is given by the area below the mitral velocity curve and is shaded light. Similarly, aortic valve regurgitation corresponds to the areas shaded dark. The closure of both the mitral valve and the aortic valve occurs just before peak flow rate of the ejection or filling phase, respectively, which can be seen in panel (a) where the sinus curve changes from light to dark or from dark to light. This graph also shows that the moment of valve closure is not periodical. Panel (b) of Figure 4.4 shows that the maximum opening angle of the aortic valve is higher than that of the mitral valve. Also the maximum opening angle is different for subsequent cycles.

Figure 4.5 (a) shows a bar plot of the regurgitant volumes of each cycle, in percentages of the stroke volume. The average aortic regurgitation is higher than the average mitral regurgitation. Furthermore, this figure shows that both the mitral and the aortic regurgitation volumes are not equal for subsequent cycles. With average aortic and mitral regurgitant volumes of 35% and 20 % of the stroke volume respectively, the cardiac efficiency (equation 4.2) equals 45%. Figure 4.5 (b) shows the maximum opening angle of the mitral and aortic valve in each cycle. Compared to the aortic valve, the fluctuation of maximum opening angles of the mitral valve is higher, while the average value is lower.

4.3.2 Influence of flow conditions on valve-valve interaction

To investigate how cardiac efficiency is influenced by the characteristics of the flow applied, a range of flow pulses characterized by nine combinations of Reynolds numbers (1200, 1800 and 2400) and Strouhal numbers (0.04, 0.08 and 0.12) was applied

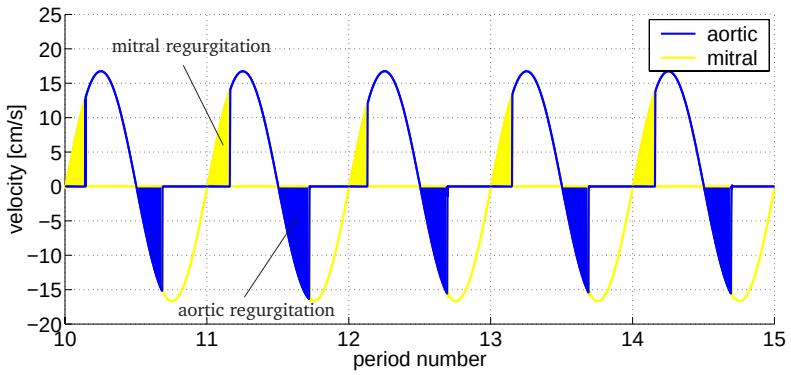

(a)

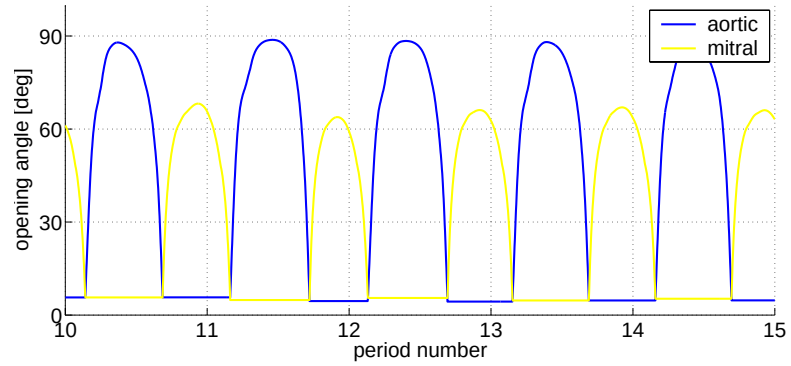

(b)

Figure 4.4: Mean velocity in atrial inflow and aortic outflow channel (a) and valve opening angle of both valves (b). In panel (a) the mitral regurgitation is given by the light colored area under the mitral velocity curve, the aortic regurgitation is given by the dark colored area. Re = 1800, Sr = 0.08.

to the model. In general, the flow phenomena described in the previous section were present in all simulations performed. However, the location and shape of the flow structures were different. Figures 4.6 and 4.7 show the normalized velocity fields $\frac{\mathbf{v}(x,t)}{V_p}$ for each simulation at the beginning of the ejection and filling phase, respectively. Overall, flow structures are affected more by a change in Strouhal number than in Reynolds number, even considering the larger variation of the Strouhal number.

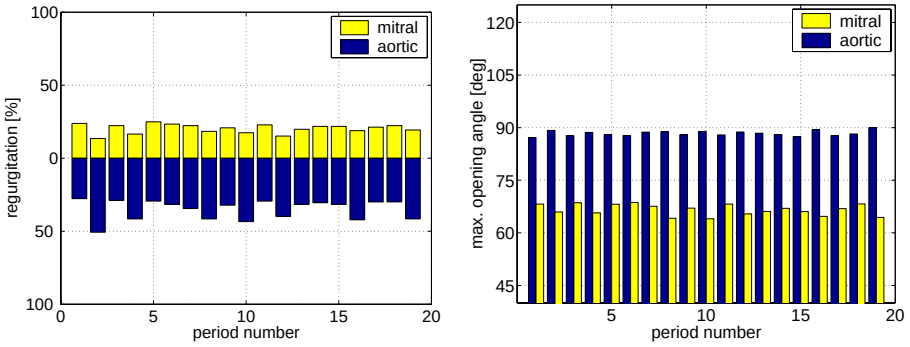

Figure 4.5: Regurgitant volumes (a) in percentages of stroke volume of the aortic (light) and mitral valves (dark) for 19 cycles. Maximum opening angle of mitral and aortic valves in each cycle are given in (b). Re = 1800, Sr = 0.08.

At the beginning of the ejection phase (Fig 4.6), the size of the *upper ventricular inflow vortex* (see Fig 4.2) decreases with increasing Strouhal number, and its location is closer to the valve base. A change in the Reynolds number is barely visible in the velocity fields.

At the beginning of ventricular filling (Fig 4.7), an increase in Strouhal number generally results in stronger, more compact *aortic outflow vortices*. An increase in the Reynolds number seems to slightly decrease the length scale of the flow structures in the aorta.

The regurgitation of the valves in each flow condition is presented in Figure 4.8. The mean value and standard deviations of the mitral and aortic regurgitation are given in Table 4.1. For each Reynolds number, an increase of the Strouhal number results in a decrease of mitral regurgitation and an increase of the aortic regurgitation. The effect of increasing the Reynolds number on the level of mitral and aortic regurgitation is far less pronounced.

Furthermore, the non-periodicity, represented by the fluctuations on the height of the subsequent bars in each plot, increases with increasing Strouhal number as well as with increasing Reynolds number. In the simulation with Reynolds number 2400 and Strouhal number 0.12, in cycle numbers 4 and 12 the aortic valve did not reach a closed position at the end of the filling phase. This is shown in the bottom right bar plot of Figure 4.8 where the dark bars show 100 % regurgitation.

Figure 4.9 shows the maximum opening angles of the mitral and aortic valves in each cycle for the nine flow conditions simulated. The fluctuations on the maximum opening angle increase with increasing Reynolds or Strouhal number. The average

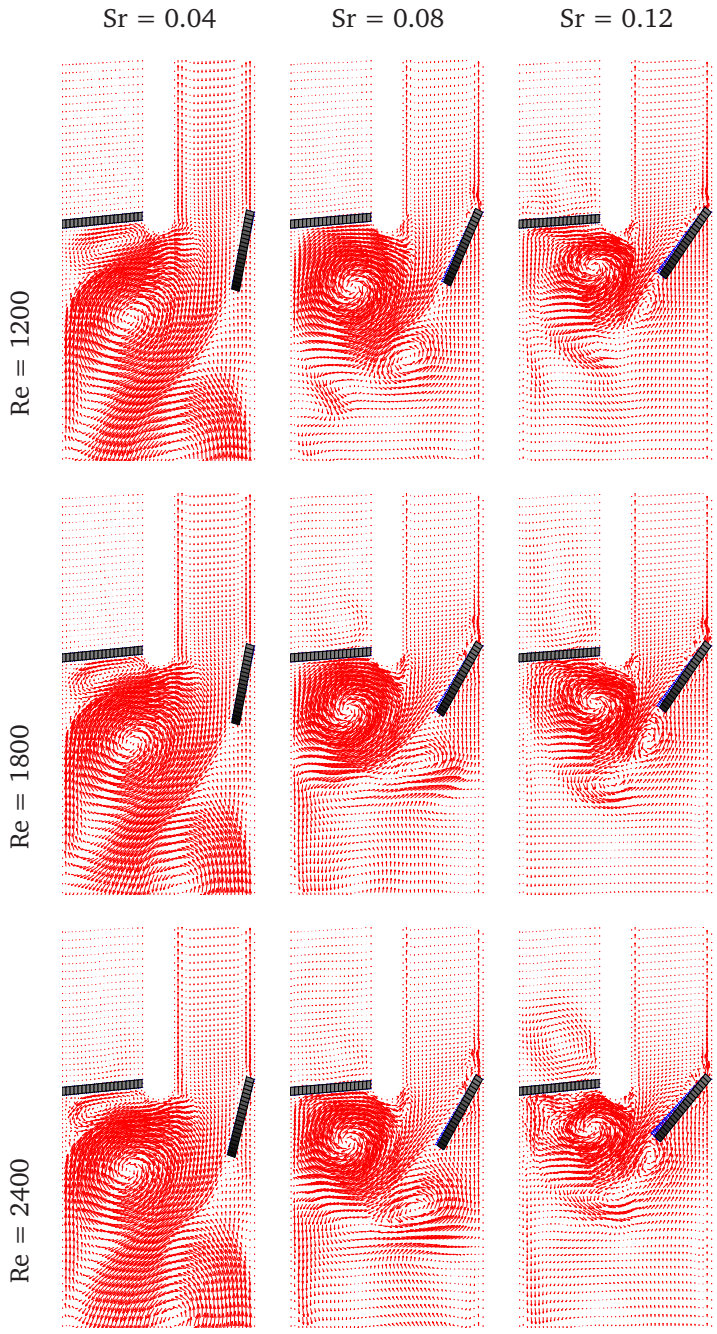

Figure 4.6: Normalized velocity fields $\frac{\mathbf{v}}{\bar{\mathbf{v}}}$ at beginning of ejection phase for each simulation performed.

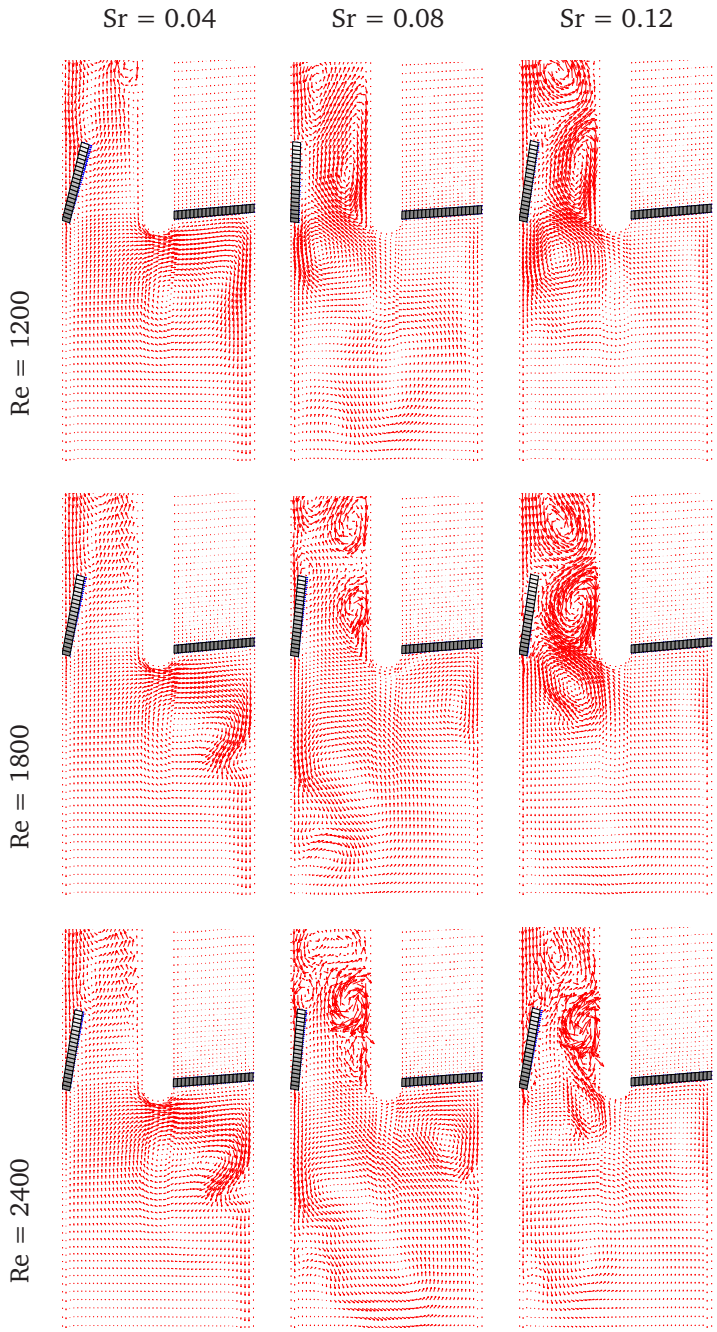

Figure 4.7: Normalized velocity fields $\frac{\mathbf{v}}{\bar{\mathbf{v}}}$ at beginning of filling phase for each simulation performed.

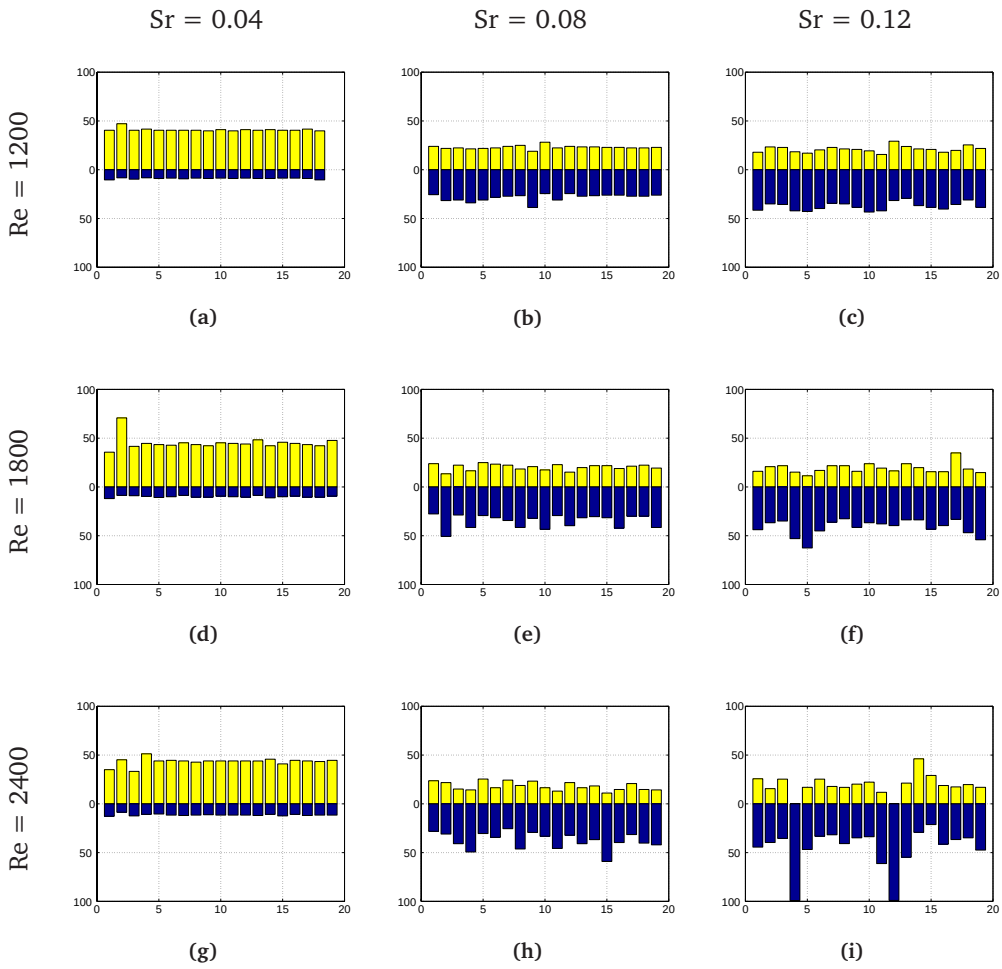

Figure 4.8: Aortic (dark bars) and mitral regurgitation (light bars) in percentage of the total stroke volume for nine simulations with different Reynolds and Strouhal numbers, for 19 cycles.

Table 4.1: Regurgitation in percentage of the stroke volume for the mitral and aortic valve for each flow condition.

	aortic valve			mitral valve		
Re \ Sr	0.04	0.08	0.12	0.04	0.08	0.12
1200	9 ± 1	28 ± 4	37 ± 4	41 ± 2	23 ± 2	21 ± 3
1800	10 ± 1	35 ± 7	41 ± 8	45 ± 7	20 ± 3	19 ± 5
2400	11 ± 1	38 ± 8	46 ± 21	43 ± 4	18 ± 4	19 ± 10

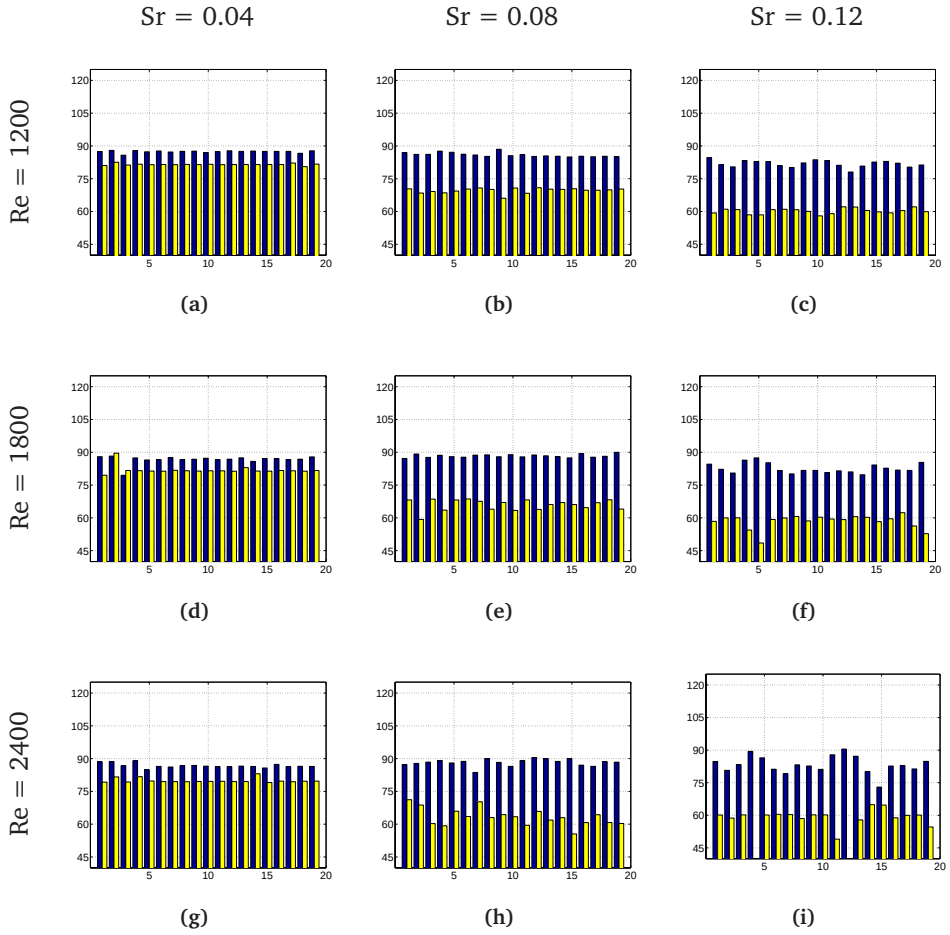

Figure 4.9: Maximum opening angle of the mitral (light bars) and aortic valves (dark bars) as a function of Reynolds and Strouhal number.

Table 4.2: Average pump efficiency of 19 cycles and standard deviations, for each simulation with different flow characteristics.

		Sr		
		0.04	0.08	0.12
Re	1200	50 ± 1	49 ± 3	42 ± 2
	1800	45 ± 6	45 ± 4	40 ± 6
	2400	45 ± 3	44 ± 5	35 ± 14

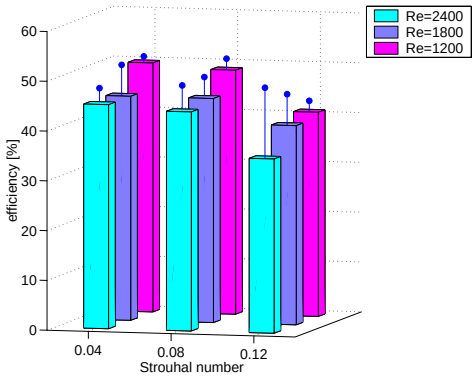

Figure 4.10: 3D bar plot of efficiency with standard deviation given by the line ended with a dot on top of the bar.

maximum opening angle of the mitral valve decreases with increasing Strouhal number, while that of the aortic valve is about constant. The average maximum opening angle does not seem to depend on the Reynolds number. In cycles 4 and 12 of the simulation represented in panel (i) of Figures 4.8 and 4.9, the aortic valve did not reach its closed position. As a result, the mitral valve did not open in these cycles which is represented in Figure 4.8 as zero regurgitation and in Figure 4.9 as a maximum opening angle of 5.7 degrees (the angle of a closed valve) which is outside the scale of this plot.

The average pump efficiency (equation 4.7) in each simulation as well as the standard deviation are given in Table 4.2 and presented graphically in Figure 4.10.

In general, increasing the Reynolds or the Strouhal number results in a decrease of the pumping efficiency of the ventricle. For the simulation with Reynolds number 2400 and Strouhal number 0.12, the average efficiency as well as the standard deviation are influenced by the cycles without aortic valve closure, causing a low average efficiency and a high standard deviation.

4.4 Discussion

Finite element simulations of the flow in a simplified two dimensional ventricular model with two valves are presented. Until now, most CFD models have focused on one valve only, thereby neglecting the interaction between valves. The models by Peskin and McQueen (1995), based on the Immersed Boundary method, incorporate

both the native mitral and aortic valves. However, to obtain numerical stability, a viscosity as high as 25 times the physiological value was necessary and as such simulations for physiological Reynolds numbers were not presented.

We used a fictitious domain method to model the interaction between the valves and the fluid. Fictitious domain methods have been used before to couple variables on separate domains that are independent of each other (Glowinski *et al.*, 1994; Bertrand *et al.*, 1997; de Hart *et al.*, 2000; Baaijens, 2001). De Hart *et al.* (2000) applied a fictitious domain method to a two dimensional model of the aortic valve, and later (de Hart *et al.*, 2003) extended the model to a three dimensional model of the native aortic valve. Using that method, pressure loading of the closed flexible leaflets of the native aortic valve proved troublesome, due to the deformation of the valve in the closed state. In this work, the position of the closed valve leaflet is known beforehand since deformation of a stiff valve is very small. Therefore, it was possible to build a mesh in which the boundary of a closed valve leaflet was coincident with an edge of the fluid elements. The Crouzeix-Raviart type elements allow a discontinuous pressure over the element boundary, and therefore the pressure loading of a closed mechanical valve was possible.

A time splitting scheme is applied to ensure convergence within 15 iterations. Results show that convergence of the solution is usually obtained using the initial time step size of T/512, except for the instants of valve closure and the first time steps immediately after closure as the instant deceleration of the fluid mass above the closed valve introduces high pressure peaks. The application of time splitting does not significantly influence the amount of valve regurgitation, as it is applied after valve closure and as such it also does not affect the efficiency of the pump function significantly. This was tested by increasing the convergence criterion by a factor 10, causing the time splitting to occur at different instants. The simulation with increased convergence criterion was run for three cycles and the maximum deviation found for the mitral regurgitant volume was 1 %, while a maximum difference in aortic regurgitation of 0.3 % was found. Part of this deviation may be attributed to the change of convergence criterion itself.

In our rigid system, the valve dynamics and the valve-valve interaction are not influenced by the pressure difference between the in- and outflow boundary as long as the pressure difference is higher than the pressure gradient that is needed to decelerate the fluid mass, i.e. ($P_o - P_i >> \rho V^2$). In the physiological case, the ratio between these two pressure gradients ($\frac{P_o - P_i}{\rho V^2}$) is in the order of magnitude of 40. In the simulations presented in this work, ratios up to 64 were reached and as such the pressure loading of the valve is deemed successful.

The decrease in vortex size with increasing Strouhal number, as observed in Figures 4.6 and 4.7, is consistent with the interpretation of the Strouhal number as the ratio of a static length scale, i.e. cavity width, over a dynamic length scale, i.e. vortex size. Increasing the Reynolds number slightly increases vortex strength and seems to promote breaking up of elongated vortices into small ones (Figure 4.7).

The motion of the mitral valve is influenced by the *upper ventricular inflow vortex* and the *lower ventricular inflow vortex* which are present below the mitral valve during filling. Due to their rotation direction, the *upper ventricular inflow vortex* will

hamper mitral valve closure, while the *lower ventricular inflow vortex* is likely to aid mitral valve closure. With increasing Strouhal number, the vortex size decreases, enabling particularly the lower ventricular inflow vortex to be located closer to the mitral valve, which results in a decrease of the mitral regurgitation. Increasing the Reynolds number, slightly increases the strength of the vortices near the mitral valve, but this hardly affects valve efficiency.

The motion of the aortic valve is influenced by the *aortic outflow vortices* which develop during deceleration of the ejection phase. Figure 4.7 shows that with increasing Strouhal number, *aortic outflow vortices* become smaller and fit more easily in the space between the opened aortic valve and the wall opposite to it. As these vortices hamper valve closure, an increase of the Strouhal number results in increased aortic valve regurgitation. An increase in the Reynolds number promotes breaking up of the elongated vortices in the aorta into smaller ones, and tends to increase the strength of these vortices. So, increasing the Reynolds number results in increased aortic regurgitation as well.

The decrease in periodicity of valve opening angles and regurgitation with increasing Strouhal number is related to vortex size as well. The exact position of a vortex depends on the valve dynamics of the previous cycle, and is therefore not necessarily the same in each cycle. With decreasing vortex size, the freedom in vortex position increases, and the interaction of the vortices with the valve becomes increasingly variable. Thus the motion of the valves will be less periodical, resulting in higher fluctuations of the regurgitant volumes for higher Reynolds and Strouhal numbers, as shown in Figure 4.8.

The results found in this work, in terms of regurgitant volumes and pumping efficiency, depend strongly on the geometry chosen of the fluid domain and are therefore not representative for physiological situations. The presented model is rigid, two dimensional and square whereas the elliptical shape of the compliant human ventricle as well as the presence of sinus cavities in the aortic root will surely influence the fluid mediated interaction between the mitral and aortic valve, and thus the cardiac efficiency and/or the cycle-to-cycle fluctuation thereof. Also, the maximum opening angle of most mechanical valve prostheses is limited to 60-90 degrees. As the maximum opening angle gets smaller, the development of vortices downstream the opened valve leaflets during deceleration is more likely to occur. These vortices may help to initiate valve closure earlier in the flow cycle and thus improve the efficiency of the valve by decreasing the amount regurgitation. Moreover, the valve leaflets would start closing from the same opening angle in each flow condition, which may influence the cardiac efficiency. Furthermore, the presence of a sinus cavity downstream the aortic valve initiates vortex formation, which may help valve closure (van Steenhoven and van Dongen, 1979; Horsten, 1990; de Hart *et al.*, 2000).

In conclusion, valve efficiency was found to depend on flow conditions: with increasing Strouhal number, mitral valve efficiency increased, aortic valve efficiency decreased and cycle-to-cycle variations of efficiency increased. With increasing Reynolds number, the same trends regarding valve efficiency were found though they were far less pronounced than for variations in the Strouhal number.

To obtain a good understanding of the interaction between the two valves, as

mediated by the fluid flow structures, a two dimensional setting was chosen. However, the quantitative results of the current two dimensional study are not believed to be representative for more realistic three dimensional geometries. Still, the qualitative outcome of this work shows that the effort needed to perform such a three dimensional analysis is worthwhile to take, as even in the two dimensional case the efficiency of the ventricle as a pump was significantly influenced by the local flow phenomena in the vicinity of the moving valves. Also a change in the mutual configuration of the two valves is expected to affect ventricular flow patterns and thus ventricular pump efficiency. Application of the method presented in this work to more realistic three dimensional geometries is expected to give more insight in the clinical impact of the choice of valve design and implantation orientation on ventricular function after valve replacement procedures. Since valve function is shown to depend on flow conditions, it would be conceivable that cardiac function can be improved by applying medication or pacemakers to influence physiological phenomena such as heart rate or stroke volume.

Bibliography

Baaijens, F. P. T. (2001). A fictitious domain/mortar element method for fluid-structure interaction. *International Journal for Numerical Methods in Fluids*, **35**, 743–761.

Bertrand, F., Tanguy, P. A., and Thibault, F. (1997). A three-dimensional fictitious domain method for incompressible fluid flow problems. *International Journal for Numerical Methods in Fluids*, **25**, 719–736.

Chandran, K. B., Shoephoerster, R., and Dellsperger, K. C. (1989). Effect of prosthetic mitral valve geometry and orientation on flow dynamics in a model human left ventricle. *Journal of Biomechanics*, **22**, 51–65.

de Hart, J., Peters, G. W. M., Schreurs, P. J. G., and Baaijens, F. P. T. (2000). A two-dimensional fluid-structure interaction model of the aortic valve. *Journal of Biomechanics*, **33**, 1079–1088.

de Hart, J., Peters, G. W. M., Schreurs, P. J. G., and Baaijens, F. P. T. (2003). A three-dimensional computational analysis of fluid-structure interaction in the aortic valve. *Journal of Biomechanics*, **36**, 103–112.

Glowinski, R., Pan, T. W., and Periaux, J. (1994). A fictitious domain method for dirichlet problem and applications. *Computer Methods in Applied Mechanics and Engineering*, **111**, 283–303.

Horsten, J. B. A. M. (1990). *On the analysis of moving heart valves: a numerical fluid-structure interaction model*. Ph-D thesis, Eindhoven University of Technology.

Peskin, C. S. and McQueen, D. M. (1995). A general method for the computer simulation of biological systems interacting with fluid. *Society for Experimental Biology*, **49**, 265–276.

Stijnen, J. M. A., de Hart, J., Bovendeerd, P. H. M., and van de Vosse, F. N. (2004). Evaluation of a fictitious domain method for predicting dynamic response of mechanical heart valves. *Journal of Fluids and Structures*. accepted.

van de Vosse, F. N., de Hart, J., van Oijen, C. H. G. A., Bessems, D., Gunther, T. W. M., Segal, A., Wolters, B. J. B. M., Stijnen, J. M. A., and Baaijens, F. P. T. (2003). Finite-element based computational methods for cardiovascular fluid-structure interaction. *Journal of Engineering Mathematics*, **47**, 335–368.

van Steenhoven, A. A. and van Dongen, M. E. H. (1979). Model studies of the closing behaviour of the aortic valve. *Journal of Fluid Mechanics*, **90(1)**, 21–32.

Chapter 5

Analysis of ventricular pump efficiency using a computational two-valve flow model: Influence of valve configuration

Abstract

The efficiency of the valves of the heart determine the efficiency at which the heart muscle can pump blood through the body. In a previous study, we have shown that cardiac pump efficiency is significantly influenced by the flow characteristics, in particular the value of the Strouhal number. In this work, the effect of valve configuration on pump efficiency is studied in a two dimensional computational model of the left ventricle with two mono-leaflet valves. The mitral valve was mounted in two orientations, such that its opening rotation was either clockwise (CW) or counter-clockwise (CCW). It was found that valve efficiency, defined as the stroke volume minus the valve regurgitant volumes in percentages, was non-periodic. For physiological flow conditions (Re=1800, Sr=0.08), the efficiency was higher in the CW configuration than in the CCW configuration, both for the aortic valve (76% vs 65%) and the mitral valve (84% vs 80%). With increasing Strouhal number mitral valve efficiency increased for the CCW configuration while it decreased for the CW configuration, and aortic valve efficiency decreased for both configurations. This effect was attributed to the decreasing size of the ventricular vortices with increasing Strouhal number.

5.1 Introduction

The four valves of the heart enable the heart muscle to fill with blood from the atria, and to eject blood into the aorta and the pulmonary artery. Due to valvular disease the condition of a valve can deteriorate to the extent that valve replacement is desired.

As for the natural valve, the performance of a valve prosthesis is the result of its interaction with the surrounding blood flow during the cardiac cycle. We have hypothesized that the opening and closing behavior of one valve will affect the motion of the other valve, and that this interaction depends on flow conditions and on the mutual configuration of the mitral and aortic valve. In the previous chapter, we investigated how flow characteristics influence the interaction between mitral and aortic valve, for one valve configuration. Changes in the Strouhal number were found to affect valve efficiency stronger than changes in the Reynolds number.

The objective of this work is to investigate to what extent the interaction between the mitral and aortic valves, and thus the pump function of the left ventricle, depends on the mutual valve configuration in the ventricle. To this end, we simulated fluid and valve dynamics in a geometrically simplified two dimensional two-valve model of the left ventricle, for a clockwise (CW) opening mitral valve and compared the results with our previous results on the counter-clockwise (CCW) opening mitral valve. In view of the results of our previous study, we varied the Strouhal number, while keeping the Reynolds number constant. We used a fictitious domain method (Glowinski *et al.*, 1994; Bertrand *et al.*, 1997; Baaijens, 2001; van de Vosse *et al.*, 2003) to account for the interaction of the mitral and aortic valve leaflets with the fluid entering and leaving the ventricle during the complete cardiac cycle.

5.2 Method

The two dimensional model used in this study is identical to the one presented in the previous chapter, except for a variation in the mitral valve configuration, and is summarized here.

5.2.1 Geometry of the model

The two dimensional geometry of the model is shown in Figure 5.1. The ventricular cavity is modeled as a rectangular domain with a rectangular inflow channel at the top right of the ventricle, representing the atrium, and a rectangular outflow channel at the top left, representing the aorta. Valves are positioned in the transitions from the in- and outflow channel to the ventricle. The mitral valve is studied in the clockwise (CW) opening configuration, as opposed to the counter-clockwise (CCW) opening configuration studied in the previous chapter. The in- and outflow channels have width D and a length H_c of 10 D. The mitral and aortic channel are separated by half a circle with a radius R of 0.2 D. Thus, the width of the ventricular cavity is 2.4 D. The ventricular cavity has a length H_v of 5 D. The fluid domain, denoted by Ω_f, is

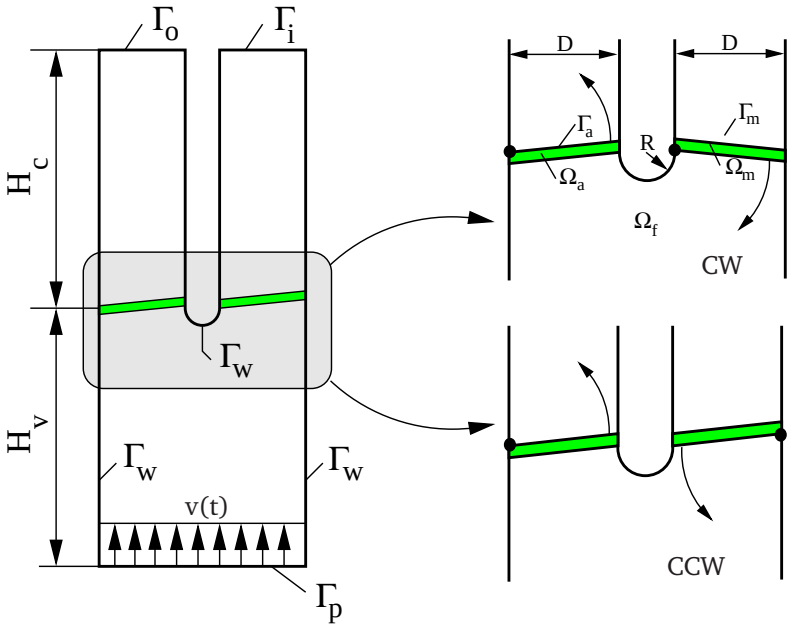

Figure 5.1: Schematic representation of the geometry, consisting of a rectangular ventricle with height H_v, in- and outflow channels with height H_c and width D representing the atrium and the aorta, and the mitral and aortic valves which can rotate around the corner points (denoted by the dots) in the direction of the arrows. To the top right, the clockwise (CW) opening mitral valve configuration is shown, to the bottom right the counter-clockwise (CCW) configuration. The fluid domain Ω_f is enclosed by boundaries Γ_w, Γ_p, Γ_i and Γ_o. At the bottom of the ventricle (Γ_p) a pulsatile plug flow v(t) is prescribed. The boundaries of the structural domains of the mitral valve (Ω_m) and the aortic valve (Ω_a) are denoted by Γ_m and Γ_a. The in- and outflow channels are separated by a half circle with radius R.

enclosed by boundaries Γ_w, Γ_p, Γ_i and Γ_o. The solid domains of the mitral valve and the aortic valve are denoted by Ω_m and Ω_a and their boundaries are Γ_m and Γ_a.

5.2.2 Fluid flow and valve motion

A pulsatile inflow velocity was prescribed at the bottom of the ventricle, varying sinusoidally in time with amplitude V_p. The characteristic velocity V is taken to be the average peak velocity in the in- and outflow channels. The Reynolds and Strouhal number, which characterize the flow pulse applied, are based on this velocity V and

are given by:

$$\mathrm{Re} = \frac{\rho \, \mathrm{V} \, \mathrm{D}}{\eta}; \qquad \mathrm{Sr} = \frac{\mathrm{D}}{\mathrm{T} \, \mathrm{V}}; \qquad \mathrm{V} = \mathrm{V_p} \frac{2(\mathrm{D} + \mathrm{R})}{\mathrm{D}} \tag{5.1}$$

For further details on the governing equations and boundary conditions regarding the fluid flow and valve motion, as well as the computational method, the reader is referred to the previous chapter.

5.2.3 Simulations and data processing

In this work the influence of mutual valve configuration on the pump efficiency of the ventricle is studied. However, the efficiency of a valve also depends on the flow conditions applied, in particular on the Strouhal number (Chapter 5). Therefore, computations were performed for a fixed Reynolds number of 1800 and three Strouhal numbers of 0.04, 0.08 and 0.12, respectively. This was done by changing the period time T of the flow pulse (equation 4.1). For each flow condition 19 cycles were simulated, in order to obtain information about the periodicity of the system response.

The efficiency of the ventricle pump is defined as the total stroke volume, applied at the bottom of the ventricle, minus the mitral and aortic regurgitant volumes, divided by the total stroke volume :

$$\text{Efficiency} = \frac{\mathrm{V_{stroke}} - \mathrm{V_{mr}} - \mathrm{V_{ar}}}{\mathrm{V_{stroke}}} \tag{5.2}$$

with $\mathrm{V_{stroke}}$ the stroke volume, $\mathrm{V_{mr}}$ the mitral regurgitant volume, $\mathrm{V_{ar}}$ the aortic regurgitant volume.

5.3 Results

5.3.1 Fluid and valve dynamics in the reference situation

Simulations were performed in a ventricular analogue model as described in the previous section. Figure 5.2 shows the computed velocity fields and valve positions at eight instants in the flow cycle, at cycle number 9 for the reference situation (Re=1800, Sr=0.08, CW configuration).

Velocity field

At the beginning of the flow cycle, i.e. the onset of fluid ejection, an *upper ventricular inflow vortex* is present below the closed aortic valve, rotating in counter-clockwise (CCW) direction (Figure 5.2 (a)). To the top left of the *upper ventricular inflow vortex*, a *secondary upper ventricular inflow vortex* is located, rotating clockwise (CW). In the center of the cavity, the *lower ventricular inflow vortex* is present, to the right of which a *secondary lower ventricular inflow vortex* has developed. The mean cross-sectional flow rate in the aortic and atrial channel is zero, and *instationary inflow boundary*

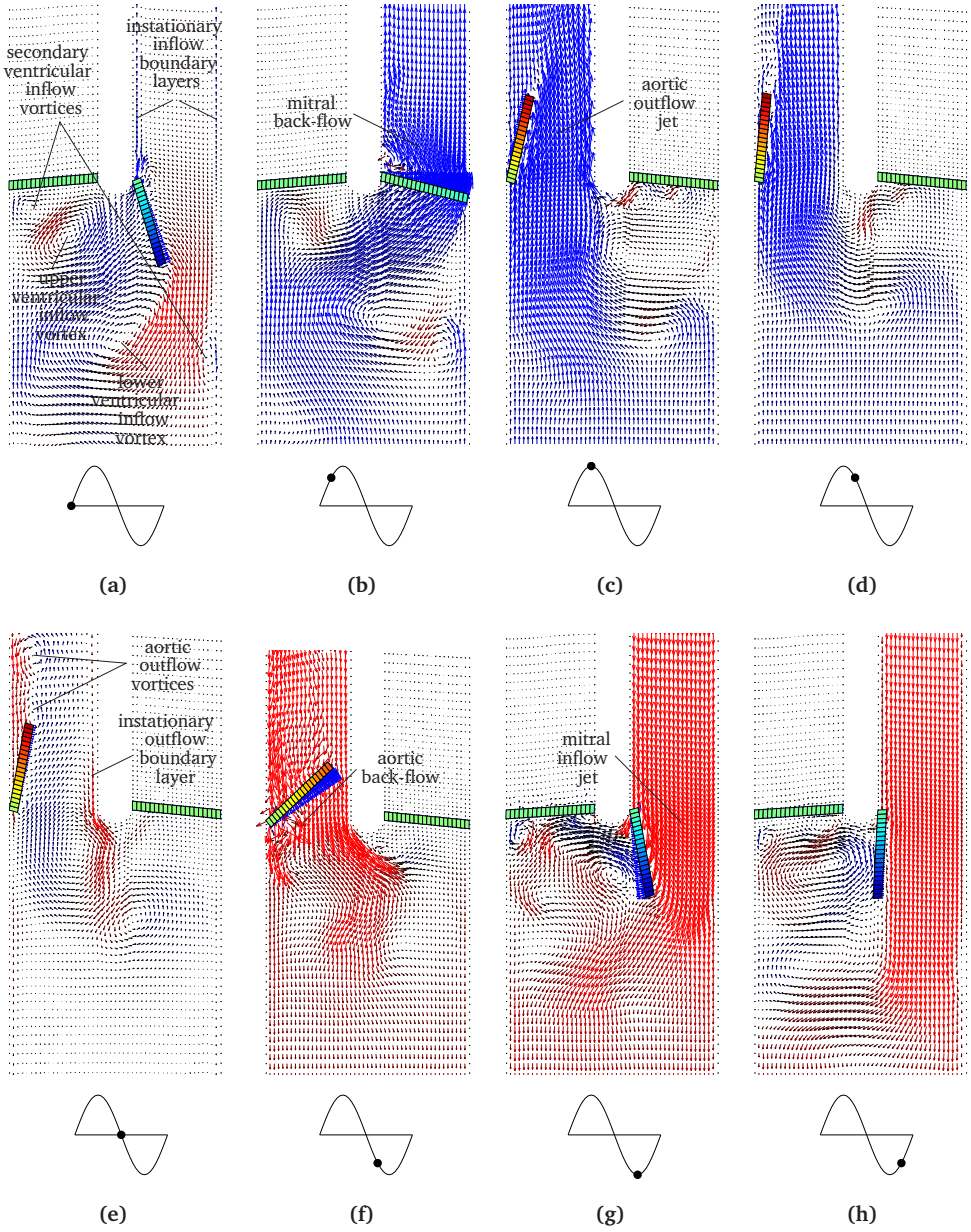

Figure 5.2: Simulation results of cycle 9 of the reference flow case (Re=1800, Sr=0.08, CW configuration), in the region of the valve base. Top row (a-d) shows flow patterns during ejection, progressing from early systole (a) to acceleration (b) to peak flow rate (c) to deceleration (d) as indicated by the dot in the flow pulse graphs below each vector field. For the filling phase the results are shown in the bottom row (e-h), the flow pulse advancing from early diastole (e) to acceleration (f) to peak flow rate (g) to deceleration (h).

layers are present near the walls of the atrial channel. The fluid flow between the *upper* and the *lower ventricular inflow vortex* has initiated the closure of the mitral valve. Application of upward flow at the bottom of the cavity (panel (b)), initially causes the fluid to flow through the opened mitral valve, causing *mitral back flow*. Due to the upward flow, the *upper ventricular inflow vortex* has diminished and has traveled toward the mitral side of the aortic valve. The *secondary upper ventricular inflow vortex* has increased in size and strength, just like the *secondary lower ventricular inflow vortex*. The *lower ventricular inflow vortex* has moved slightly toward the valve base. The mitral valve has closed before peak flow rate is reached (c). The *mitral back flow* is cut off instantly at mitral valve closure, due to which some small vortices have developed below the closed mitral valve. The *upper ventricular inflow vortex* has traveled toward the center of the valve base and now is very weak. Opening of the aortic valve happens very quickly, due to the high flow rate at this point in the flow cycle. The fluid velocity in the aorta is higher at the mitral side than downstream the opening aortic valve. In the deceleration phase of ejection (d), the aortic valve is fully opened, almost parallel to the flow of the *aortic outflow jet*. Downstream the aortic valve, the flow rate is lower near the aortic valve than in the rest of the aortic channel. The *lower ventricular inflow vortex* has now almost diminished and traveled to the mitral side of the aortic opening, just below where the tip of the closed aortic valve would be. The remains of the *secondary lower ventricular inflow vortex* have moved slightly toward the valve base and to the center of the ventricular cavity.

At the onset of the ventricular filling phase (e), the flow rate applied is zero. Downstream the aortic valve, *aortic outflow vortices* have developed. To the mitral side of the aortic channel, an *instationary outflow boundary layer* is present. Due to the forward flow in the center of the aortic opening and the reversed flow in the *instationary outflow boundary layer* at the mitral side of the aorta, the *lower ventricular inflow vortex* has regained strength and increased in size, and is now located in the transition from the ventricle to the aorta. The remains of the *secondary lower ventricular inflow vortex* in panel (d) have regained a vortical shape, which is located to the lower right of the *lower ventricular inflow vortex*. In the acceleration phase of ventricular filling (f), the fluid is sucked into the ventricle out of the aorta, causing *aortic back flow* and aortic valve closure. At peak flow rate (g), the aortic valve is closed and the mitral valve has opened rapidly. Below the closed aortic valve, a flow structure induced by the mitral valve opening displacement has developed. A *mitral inflow jet* is caused by the fluid entering the ventricle from the atrial channel, which is directed toward the bottom of the ventricle. At the end of the cycle the *mitral inflow jet* is decelerating (h), causing the development of the *lower ventricular inflow vortex* in the process. An *upper ventricular inflow vortex* has developed from the *mitral inflow jet* that originated from the fluid being pushed away by the opening mitral valve. As the flow reduces further, the *mitral inflow jet* becomes weaker and the *upper* and *lower ventricular inflow vortex*, as well as the *secondary ventricular inflow vortices* increase in size (a).

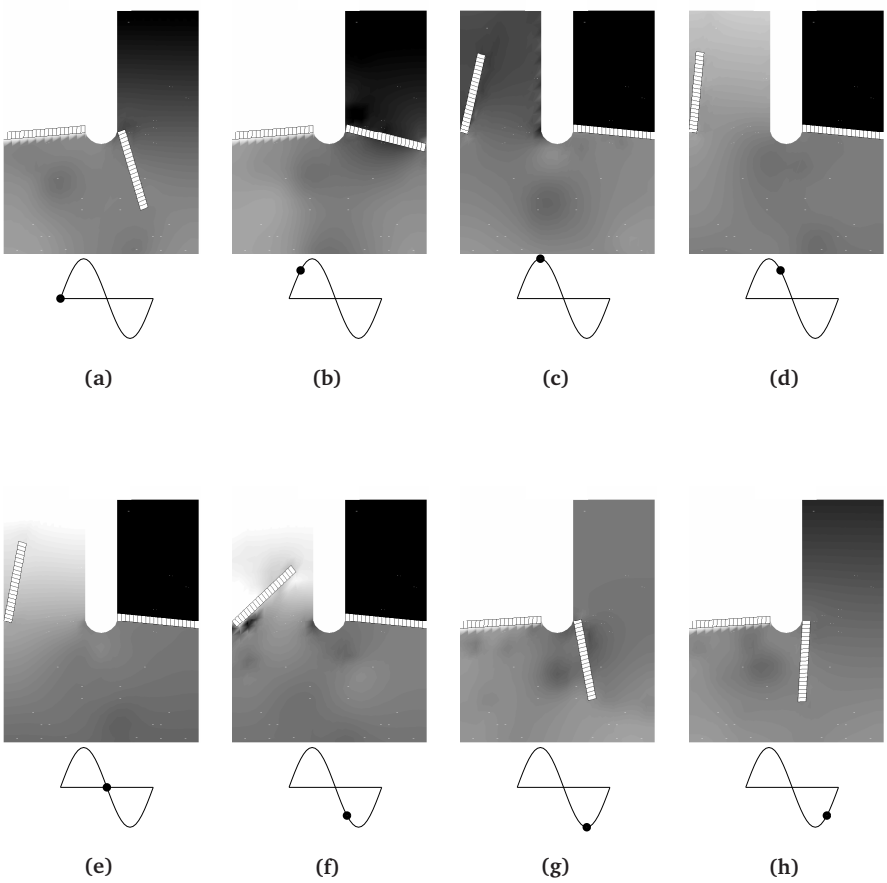

Figure 5.3: Normalized pressure $\frac{p}{\rho V^2}$ belonging to the velocity fields of Figure 5.2. The middle gray-scale value is adapted to the mean pressure in the area between the valve base and one valve diameter below. Higher pressures have a lighter gray value.

Pressure field

Figure 5.3 shows the normalized pressure distribution $\frac{p}{\rho V^2}$ belonging to the velocity fields shown in Figure 5.2, with V defined in equation 5.1. The initiation of pumping fluid out of the ventricle at the start of the ejection phase (a), causes the ventricular pressure to be higher than the atrial pressure. The pressure in the cores of the *upper* and *lower ventricular inflow vortex* is lower than in the surrounding fluid, which is represented by the darker regions in the ventricle. In panel (b) the fluid acceleration into the atrial tube causes an increased atrio-ventricular pressure gradient. At peak flow rate (c) the mitral valve has closed, causing the ventricular pressure to rise above the aortic pressure due to which the aortic valve opens and the fluid accelerates into the aorta. The core of the *lower ventricular inflow vortex* is represented by the dark area in the central part of the ventricle. In panel (d) fluid deceleration is imposed, causing the pressure gradient between the ventricle and aorta to change sign (aortic region has turned lighter than ventricular region). The ventricular-aortic pressure gradient is smaller than in the previous panel. The core of the *secondary lower ventricular inflow vortex* has entered the plotted region of the ventricle at the bottom. Towards the end of the ejection phase, fluid deceleration increases which is reflected in the increase in aortic pressure gradient from (d) to (e). In the first part of fluid acceleration in the filling phase (e-f) the acceleration is nearly constant, which is reflected by similar pressure gradients from the aorta to the ventricle. The aortic valve closes before peak flow rate during filling (g), after which the ventricular pressure drops below atrial pressure. As fluid deceleration is imposed (h), the ventricular pressure rises above atrial pressure. The core of the *upper ventricular inflow vortex* is visible below the closed aortic valve.

5.3.2 Influence of Strouhal variation on the velocity field

To investigate how the pump efficiency of the ventricle is influenced by a variation in the Strouhal number with respect to the reference value of 0.08, this number was lowered to 0.04 and increased to 0.12. In general, the flow phenomena described in the previous section were present in all simulations performed. However, the location and shape of the flow structures were different. Figure 5.4 shows the normalized velocity fields $\frac{\mathbf{v}(\mathrm{x,t})}{\mathrm{V}}$ for each simulation at the beginning of both the ejection and filling phase. In general, increasing the Strouhal number results in smaller but stronger, more circularly shaped vortices. At the beginning of the ejection phase (Fig 5.4 (a-c)), the position of the upper and lower ventricular inflow vortices is closer to the valve base.

At the beginning of ventricular filling (Fig 5.4 (d-f)), an increasing Strouhal number generally results in stronger *aortic outflow vortices*. Furthermore, the lower ventricular inflow vortex and the secondary lower ventricular inflow vortex remain inside the ventricular cavity and increase in size and strength with increasing Strouhal number. Their position is located more toward the aortic opening for decreasing Strouhal number.

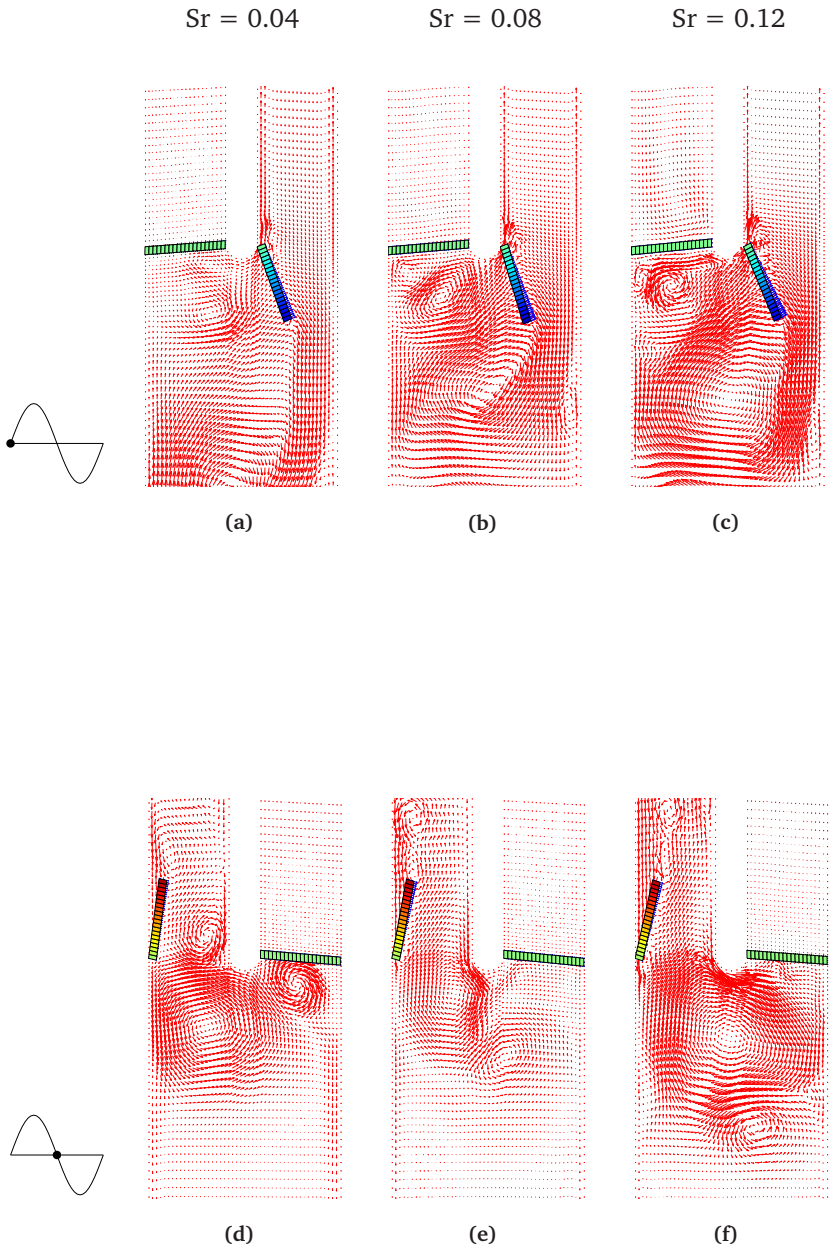

Figure 5.4: Normalized velocity fields $\frac{\mathbf{v}}{\bar{\mathbf{v}}}$ at beginning of ejection phase (a-c) and at beginning of filling phase (d-f) for each simulation performed.

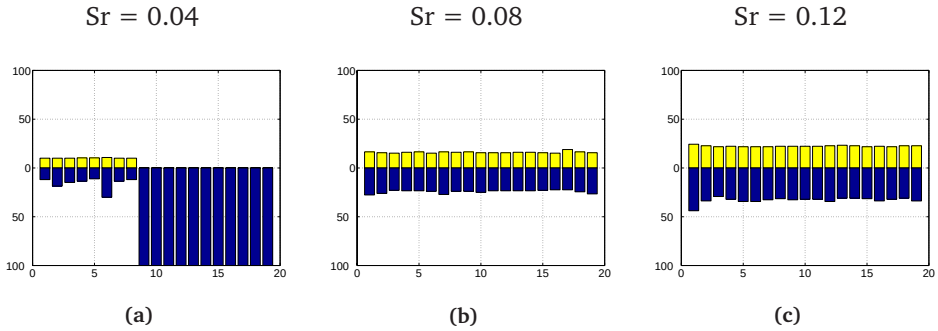

Figure 5.5: Aortic and mitral regurgitation in percentage of the total stroke volume for nine simulations with different Strouhal numbers and Reynolds number equal to 1800. The simulations were run for 19 cycles of which the regurgitation is shown in each graph. The aortic regurgitation is given by the dark bars, the mitral regurgitation by the light bars.

5.3.3 Influence of Strouhal variation on valve regurgitation

At the beginning of the filling phase, the aortic valve has not closed (see Fig 5.2(e)), which leads to a leakage of fluid into the aorta until the aortic valve is closed. Similarly, mitral regurgitation occurs at the beginning of the ejection phase. The regurgitation of the valves in each flow condition is presented in Figure 5.5 and summarized in Table 5.1. The non-periodicity, represented by the fluctuations on the height of the subsequent bars in each plot in Figure 5.5 and by the standard deviation in Table 5.1, does not seem to depend on the Strouhal number. An increase of the Strouhal number results in an increase of both the aortic and the mitral regurgitation (Table 5.1). For reference, this table also presents the results in the CCW valve configuration presented in the previous chapter. The non-periodicity in the regurgitation of both valves is higher for the CCW configuration, as shown by the values of the standard deviation in Table 5.1.

In the simulation with Strouhal number equal to 0.04, something extraordinary occurs in cycle number 9 (Figure 5.5(a)); at the end of the ejection phase, the *lower*

Table 5.1: Regurgitation in percentage of the stroke volume for the mitral and aortic valve for each flow condition and valve configuration.

	aortic valve			mitral valve		
Re \ Sr	0.04	0.08	0.12	0.04	0.08	0.12
CW	16 ± 6	24 ± 2	33 ± 3	10 ± 0	16 ± 1	22 ± 1
CCW	10 ± 1	35 ± 7	41 ± 8	45 ± 7	20 ± 3	19 ± 5

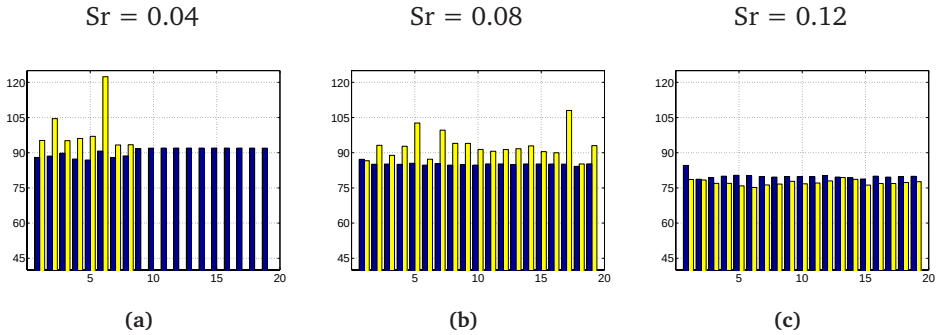

Figure 5.6: Maximum opening angle of the mitral (light bars) and aortic valves (dark bars).

ventricular inflow vortex enters the space between the opened aortic valve and the mitral side of the aortic wall. At that instant, the local fluid velocity is such that the aortic valve is pushed further open, never to close again. The aortic valve finds a state of equilibrium, where it sways as the fluid accelerates and decelerates alongside the opened valve. From this point, the aortic regurgitation is assumed to be 100% and the mitral regurgitation is assumed to be 0% of the stroke volume, as shown in panel (a) of Figure 5.5. The mean value and standard deviation of the regurgitant volumes presented in Table 5.1 are therefore based on the first eight cycles.

Figure 5.6 shows the maximum opening angles of the mitral and aortic valves in each cycle for the three flow conditions simulated. With increasing Strouhal numbers, the fluctuations on the maximum opening angle of the mitral valve decrease, while the fluctuations on the maximum aortic opening angle seem to be unaffected. The average maximum opening angle of both the mitral and aortic valve decreases with increasing Strouhal number.

The average pump efficiency (equation 5.2) in each simulation as well as the standard deviation are given in Table 5.2 and presented graphically in Figure 5.7. For reference, the values of the simulations with the CCW valve configuration presented in the previous chapter are given as well. In general, increasing the Strouhal number results in a decrease of the pumping efficiency of the ventricle. In all three flow conditions the CW configuration leads to higher pumping efficiency with respect to the CCW configuration. The improvement in efficiency decreases with increasing Strouhal number.

5.4 Discussion

The relation between flow conditions, valve configuration and valve efficiency can only be understood through a detailed view of the velocity field. For reference, Figure 5.8 shows the results of the CCW configuration in the same way they are presented

Table 5.2: Average pump efficiency of 19 cycles and standard deviations, for both valve configurations. Reynolds was kept constant at 1800. * indicates average and standard deviation over 8 cycles.

	Sr		
config	0.04	0.08	0.12
CW	74* ± 6*	60 ± 2	45 ± 3
CCW	45 ± 6	45 ± 4	40 ± 6

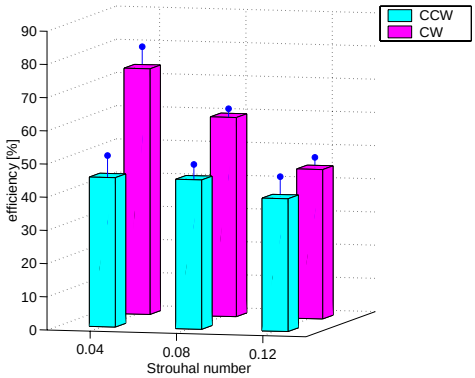

Figure 5.7: 3D bar plot of efficiency with standard deviation given by the line ended with a dot on top of the bar, for both valve configurations at Reynolds 1800.

in Figure 5.4 for the CW configuration.

In the reference flow case (Re = 1800, Sr = 0.08), in the CW configuration the ventricular inflow vortices are positioned further away from the valve base than in the CW configuration, as the fluid that enters the ventricle in the CW configuration is directed further into the ventricle by the opened mitral valve. In the CCW configuration, the strength of the upper ventricular inflow vortex is higher, and its rotation direction hampers mitral valve closure. As a direct result the mitral regurgitation is higher in this configuration (20% vs 16%).

During fluid ejection, in the CW configuration the lower ventricular inflow vortex and the secondary vortex remain in the ventricle, whereas in the CCW configuration the ventricular vortices are washed into the aortic channel. As a result, in the CCW configuration several vortices develop near the aortic wall opposite to the opened aortic valve, which hamper aortic valve closure. As such, the aortic regurgitation is higher in this configuration (35% vs 24%).

With increasing Strouhal number, the velocity fields for both the CW and the CCW configuration show a decrease in length scale and relative strength of the ventricular vortices in the ejection phase. This finding is consistent with the interpretation of the Strouhal number as the ratio of a static length scale, i.e. cavity width, over a dynamic length scale, i.e. vortex size. The decrease in size allows the vortices to be located closer to the valve, increasingly affecting the fluid flow in the vicinity of the valve leaflets.

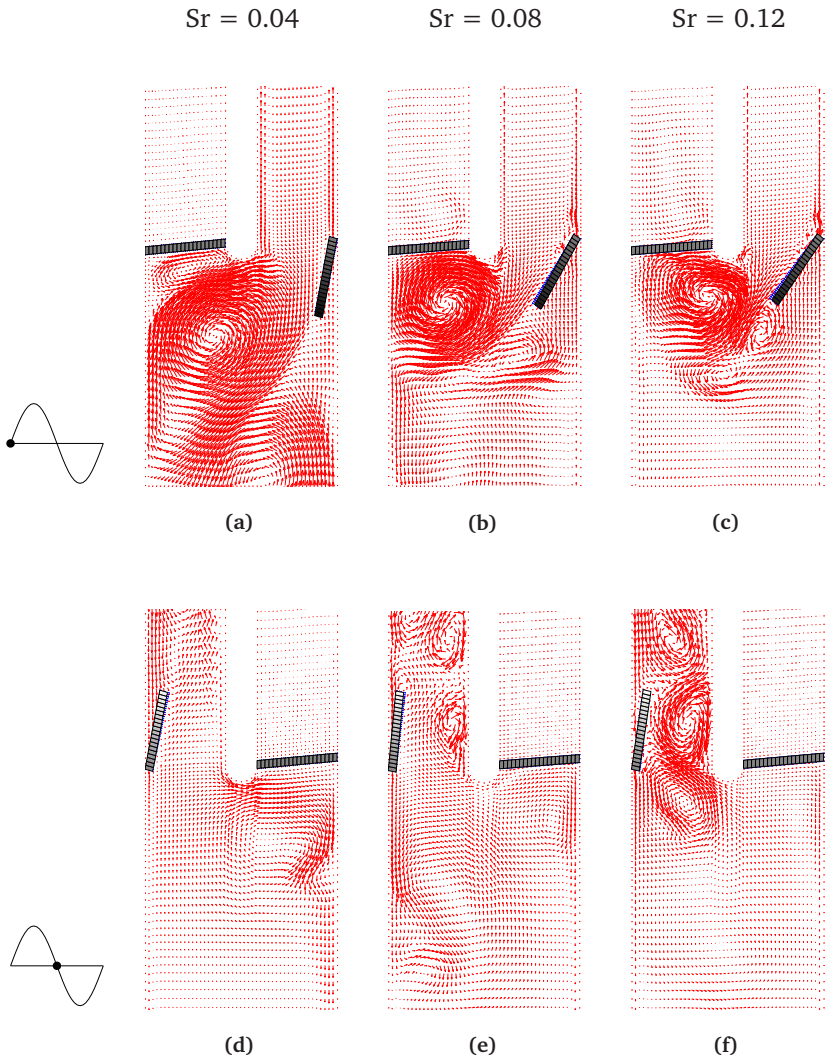

Figure 5.8: Normalized velocity fields $\frac{v}{V}$ at beginning of ejection phase (a-c) and at beginning of filling phase (d-f) for the simulations with Re = 1800 and the CCW opening mitral configuration.

For both configurations, aortic valve regurgitation increases with increasing Strouhal number. In the early stages of valve closure, the moment of the reversed flow on the valve is low as the valve is aligned to the main flow direction. As the valve is closing, its alignment will be increasingly perpendicular to the main flow direction, due to which the angular velocity will increase. As the fluid acceleration is higher for in-

creasing Strouhal number, more fluid will leak past the closing valve in the early stage of valve closure, resulting in higher aortic regurgitation. In addition to this effect, *ventricular inflow vortices* wash out into the aorta in the CCW opening orientation, which results in several *aortic outflow vortices*. Aortic valve closure is hampered by these vortices, resulting in higher aortic regurgitations compared to the CW configuration. With increasing Strouhal number, these vortices increase in strength and are located closer to the opened aortic valve, increasingly hampering aortic valve closure.

With increasing Strouhal number, mitral regurgitation increases for the CW configuration, but decreases for the CCW configuration In the CCW configuration, the upper ventricular inflow vortex hampers mitral valve closure while the lower ventricular inflow vortex helps mitral valve closure. As vortex size decreases with increasing Strouhal number, the lower ventricular inflow vortex is able to be closer to the mitral valve, which results in lower mitral regurgitation. In the CW configuration, the *upper* and *lower ventricular inflow vortex* are helping the initiation of mitral valve closure. However, in this configuration the mitral valve opens further than in the CCW configuration and the ventricular vortices are further away from the mitral valve which reduces the interaction. An increase of the Strouhal number from 0.04 to 0.12 resulted in 12% more mitral regurgitation for the CW configuration, while for the CCW configuration a decrease of 26 % of the stroke volume was found (see table 5.1).

The regurgitant volumes are more constant in subsequent cycles in the CW configuration as the vortices are further away from the opened valves, which may indicate a more stable system. This is reflected by a lower value of the standard deviation on the mean regurgitant volumes shown in table 5.1, and by the height differences in subsequent bars in Figures 4.8 and 5.5. However, due to the uniform direction of the fluid mass below the closing mitral valve, a large volume of moving fluid is stopped instantaneously at mitral closure. In the CCW configuration, the fluid directed toward the closing mitral valve can follow the rotational direction of the vortices, which may result in a lower impact of the closing mitral valve.

The results found in this work, in terms of regurgitant volumes and pumping efficiency, depend strongly on the chosen geometry and are therefore not representative for physiological situations. The presented model is two dimensional and square while the elliptical shape of the human ventricle as well as the presence of sinus cavities in the aortic root will surely influence the fluid mediated interaction between the mitral and aortic valve, and thus the cardiac efficiency.

The maximum opening angle of most mechanical valve prostheses is limited to 60-90 degrees. As the limited maximum opening angle gets smaller, the development of vortices downstream the opened valve leaflets during deceleration is more likely to occur. These vortices may help to initiate valve closure earlier in the flow cycle and thus improve the efficiency of the valve by decreasing the amount regurgitation. Moreover, the valve leaflets would start closing from the same opening angle in each flow condition, which may influence the cardiac efficiency and may reduce the cycle-to-cycle variations. Furthermore, the presence of a sinus cavity downstream the aortic valve initiates vortex formation, which may help valve closure (van Steenhoven and van Dongen, 1979; Horsten, 1990; de Hart *et al.*, 2000).

In conclusion, valve efficiency was found to depend both on the mutual valve

configuration and on the flow conditions. With increasing the Strouhal number, aortic valve efficiency decreased for both configurations, and mitral valve efficiency decreased in the CW configuration, whereas it increased in the CCW configuration. The total pump efficiency of the ventricle with two valves was better for the CW configuration of the valves and that this improvement in efficiency was decreasing with increasing Strouhal number.

A two dimensional setting was chosen for this work, in order to obtain a good understanding of the fluid mediated interaction between the two valves. Although the geometry chosen is not believed to generate results that are quantitatively representative for realistic three dimensional geometries, clear qualitative trends in pump efficiency and cycle-to-cycle variations thereof are found not only with respect to flow conditions but also to the mutual configuration of the mitral and aortic valve. As such, the outcome of this work shows that the effort needed to perform a three dimensional analysis is worth-wile to take. Application of the method presented in this work to more realistic three dimensional geometries is expected to give more insight in the clinical impact of the choice of valve design and implantation orientation on ventricular function after valve replacement procedures. Furthermore, post-surgical medication to improve flow conditions, in physiological terms of stroke volume, heart rate of blood pressure, could be provided based on physical knowledge generated by such three dimensional models.

Bibliography

Baaijens, F. P. T. (2001). A fictitious domain/mortar element method for fluid-structure interaction. *International Journal for Numerical Methods in Fluids*, **35**, 743–761.

Bertrand, F., Tanguy, P. A., and Thibault, F. (1997). A three-dimensional fictitious domain method for incompressible fluid flow problems. *International Journal for Numerical Methods in Fluids*, **25**, 719–736.

de Hart, J., Peters, G. W. M., Schreurs, P. J. G., and Baaijens, F. P. T. (2000). A two-dimensional fluid-structure interaction model of the aortic valve. *Journal of Biomechanics*, **33**, 1079–1088.

Glowinski, R., Pan, T. W., and Periaux, J. (1994). A fictitious domain method for dirichlet problem and applications. *Computer Methods in Applied Mechanics and Engineering*, **111**, 283–303.

Horsten, J. B. A. M. (1990). *On the analysis of moving heart valves: a numerical fluid-structure interaction model*. Ph-D thesis, Eindhoven University of Technology.

van de Vosse, F. N., de Hart, J., van Oijen, C. H. G. A., Bessems, D., Gunther, T. W. M., Segal, A., Wolters, B. J. B. M., Stijnen, J. M. A., and Baaijens, F. P. T. (2003). Finite-element based computational methods for cardiovascular fluid-structure interaction. *Journal of Engineering Mathematics*, **47**, 335–368.

van Steenhoven, A. A. and van Dongen, M. E. H. (1979). Model studies of the closing behaviour of the aortic valve. *Journal of Fluid Mechanics*, **90(1)**, 21–32.

Chapter 6

Discussion and conclusions

6.1 General discussion

The aim of this study was to develop a computational model of the relation between mitral valve orientation and left ventricular flow that can simulate the entire cardiac cycle, and to use that model to investigate to what extent the efficiency by which prosthetic heart valves are able to direct fluid from the atrium to the aorta, in terms of regurgitant volume of the valves with respect to ventricular stroke volume, is depending on the interaction of the valve leaflets with the surrounding fluid flow, which in turn is influenced by specific valve properties like the orientation of a mitral valve prosthesis. Many studies reported in literature address ventricular flow patterns, but often these studies are either two dimensional, simulate only the ejection or the filling phase and most do not incorporate valve dynamics (Taylor and Yamaguchi, 1995; Redaelli and Montevecchi, 1996; Shortland *et al.*, 1996; Lemmon and Yoganathan, 2000; Vierendeels *et al.*, 2000; Saber *et al.*, 2001; Baccani *et al.*, 2003). Fully three-dimensional fluid-structure interaction models of flow through moving heart valves are also published (Peskin and McQueen, 1989; de Hart *et al.*, 2003) in literature. The model by Peskin was able to simulate ventricular flow during an entire cardiac cycle, but in order to obtain stability for the solution the viscosity of the fluid needed to be 25 times that of blood. De Hart *et al.* (2003) simulated blood flow through the aortic valve for the systolic phase only. While many studies address ventricular flow or flow through moving valves, none of these studies focus on the interaction between the mitral and aortic valve, and the associated efficiency by which the heart can expel blood.

Before studying the interaction of the valves with the local flow patterns, we first focus on understanding the complex three dimensional ventricular flow patterns themselves. In *Chapter 2*, a pilot study is presented in which a first step towards a computational model to compute ventricular flow patterns is made, and an *in-vitro* setup is used to obtain experimental data on ventricular flow patterns. A stylistic ventricle geometry was chosen, without too much detail but such that the essence of the geometry of the natural ventricle was captured. In the *in-vitro* setup, Carbomedics

bi-leaflet valve prostheses were used in both the mitral and the aortic positions and DPIV was used to obtain velocity fields in two cross-sectional planes of the model ventricle. As a first step in the computational model, the mitral valve structure was approximated by two narrow blocks of high fluid viscosity in the mitral opening, such that the central orifice area matched that of the prosthetic valve whereas the width of the blocks was chosen such that the entire opened leaflet would fit inside. For the opened aortic valve the viscosity was not raised, whereas for the closed aortic valve the viscosity in the entire outflow orifice was raised. Physiological flow conditions are characterized by a Reynolds number in the order of 3000 and a Strouhal number of 0.04. Experiments and CFD simulations were performed for reduced stroke volume and increased fluid viscosity resulting in a Reynolds number in the order of $1.2{\cdot}10^3$ and a Strouhal number of 0.05, as the computational model did not allow higher settings for the mesh density chosen. Mesh refinement will probably allow for higher settings of the Reynolds and Strouhal number, but will also result in considerably higher memory usage and computational time.

The results of the CFD simulations and the experimental DPIV data, show similar flow structures. Moreover, both methods show that a 90 degree rotation of the mitral valve results in significantly different ventricular flow fields. Showing this was the goal in the first stage of the investigation. However, from the direct comparison of the vertical velocity component it is evident that the computed fluid velocity in the center of the ventricular jets is significantly higher than measured experimentally, up to twice the maximum velocity at peak flow rate during filling. The difference between the computed and the experimental velocities is predominantly attributed to the area of the mitral valve model, which entails a reduction of orifice area of about 30% with respect to the prosthetic valve. The opening angle of the valve also attributes to the difference in jet position. In the prosthetic valve the opened leaflets have an opening angle of approximately 72 degrees, whereas a 90 degree opening angle was applied in the computational model. The initial geometry of the computational ventricle model, which is cylindrical whereas it is elliptical in the experiments, attributes to a higher jet velocity as well as a deviation in the position of the inflow jets.

Further development of the model is considered valuable, to enable studies of the interaction between the mitral and aortic valves which can be beneficial to understanding the relation between valve orientation and ventricular pumping efficiency. Refinement of the viscosity based valve model is not considered a sensible next step: it would require substantial mesh refinement while still the timing of opening and closure would have to be prescribed, based on the volume signal. Instead, modeling of fluid-structure interaction between moving valve leaflets and the surrounding fluid flow was chosen. In order to increase insight in the fluid-structure interaction as well as to reduce computational times, a two-dimensional setting was chosen for these studies.

In *Chapter 3*, the motion of a single leaflet in a flow channel with a sinus cavity downstream the leaflet is studied in a two dimensional computational model and in a quasi two dimensional *in-vitro* setup. The setup consisted of a wide channel with respect to its height in which the fluid velocity field in the center plane was assumed to be two dimensional. DPIV measurements are performed to obtain experimental

data on fluid velocity fields and valve leaflet position. In the finite element model, a fictitious domain method is evaluated for its capability to predict time dependent leaflet motion. The results showed that the computed fluid velocity fields matched the experimental measurements for a range of flow pulses applied. The computed position of the valve leaflet did not exactly match the experimental observations, but the timing of the leaflet motion was predicted within the range of the experimental data. The inaccuracy of the predicted valve position was attributed to three dimensional effects near the side walls of the flow channel, interfering with valve motion. The computational method proved to be able to predict the time dependent behavior of the valve in a correct manner, and as such the method is assumed to be applicable to study valve motion.

The efficiency of the ventricle to pump blood around the body is depending on the motion of both the mitral and the aortic valve. The response of the single valve model presented in *Chapter* 3 is therefore not adequate to analyze the pumping function of the ventricle, as a changed response of one valve will reflect in the response of the other valve, both attributing to the efficiency of the ventricle as a pump. In *Chapter 4* a computational model of a ventricular cavity is presented with rigid mono-leaflet in- and outlet valves, which was used to simulate the fluid mediated interaction between the mitral and aortic valve for 9 different flow conditions. In order to perform the simulations the valves have to be able to bear a pressure load in the closed position. Pressure loading was made possible by generating a computational mesh such that the boundaries of the valve leaflets were coincident with an edge of the fluid elements. The closed valve leaflet was kept in its undeformed position, thereby neglecting possible deformation of the rigid valve due to the pressure loading. The results show that flow conditions influence valve regurgitation and the total efficiency of the ventricle as a pump, in terms of output stroke volume. It was also found that the regurgitant volume of the model valves did not become periodical, but cycle-to-cycle variations of the regurgitant volumes remained present for the 19 cycles that were simulated for several flow conditions. Moreover, the cycle-to-cycle variation in valve regurgitation was influenced by the flow conditions. The parameter study in Chapter 4 showed that variations in the Strouhal number had a larger effect on valve efficiency that variations in the Reynolds number.

Applications of the model to a more realistic compliant ventricle is not straightforward. The current implementation of the fictitious domain method, couples velocity of both media (fluid and valve). In the situation where a moving valve is near its closed position, the tip of the valve translates along a wall of the fluid domain. The velocity at the tip of the valve is weakly coupled to the fluid velocity at the wall, which is usually zero. So, near the closed position, prescribing a volumetric flow through the valve orifice will induce a high pressure at the upstream side of the valve. Therefor, the method is applicable to uncompliant systems with prescribed flow only, as in a compliant system the shape of the fluid domain would be changed as a result of the increased pressure. When introducing an active ventricle wall, providing the ventricular pressure needed for fluid ejection, such a stiff valve may not even open as the pressure needed for valve opening would be too high. Replacement of the coupling of the motion of stiff leaflets and zero velocity fluid boundary conditions by a contact al-

gorithm is recommended, as it may provide a suitable solution for compliant systems, as well as be beneficial for the stability of uncompliant systems due to the reduction of pressure.

The computational model of the interaction between the mitral and aortic valve presented in Chapter 4, was used in *Chapter 5* to study the effect of a change in mitral valve orientation on flow patterns in the cavity and subsequently on the valve-valve interaction. The regurgitant volumes of both the aortic and the mitral valve were affected significantly by changing the rotation direction of the mitral valve. Large differences in efficiency, up to 30% of the stroke volume, were found for changes in the orientation of the mitral valve. Furthermore, the cycle-to-cycle variation in the regurgitant volumes changed significantly by changing the mitral orientation.

The values found for the regurgitant volumes in the two dimenstional models have to be put into perspective. The influence of valve orientation on efficiency of the ventricle as a pump is not believed to be as large as the results of the two-dimensional computational method of Chapters 4 and 5 suggest. For the simulations with a Reynolds number of 1200 and a Strouhal number of 0.08, regurgitation of the aortic valve was found to be 28 % of the stroke volume. In Chapter 3, aortic regurgitations of 8% were found for a valve upstream a sinus cavity albeit at a Reynolds number of 750. Even though the Reynolds number of the simulations with the single valve are about half that of the two-valve ventricle simulations, it is assumed to be unlikely that regurgitant volumes of 28% of the stroke volume would be found in the latter simulations if a sinus cavity would be present downstream the aortic valve. Furthermore, the valves in the model used in Chapters 3, 4 and 5 were not limited in motion with respect to the maximum opening angle. Most mono-leaflet and bi-leaflet valves commercially available have a maximum opening angle varying from about 60 to 90 degrees. The results in Chapters 4 and 5 suggest that valve leakage is partly due to the reluctance of a valve to close when aligned to the main flow direction, as the rotational moment that the fluid can apply to the valve in that position is small. As such, a reduction of the maximum opening angle would reduce valve regurgitation and the pump efficiency of the ventricle might improve as a result. The three dimensional flow patterns presented in Chapter 2 show that the ventricular vortices are far downstream the mitral valve, compared to the two dimensional flow patterns presented in Chapters 4 and 5. This may indicate that the interaction of flow structures with the valve leaflets is not as large in a three-dimensional ventricular geometry as in the geometry used for in the studies of Chapters 4 and 5.

The three dimensional computational model of the relation between mitral valve orientation and ventricular flow patterns resulted in similar flow patterns as obtained in the *in-vitro* setup. The difference in velocity fields found was attributed to the difference in geometry of the mitral valve model with respect to the prosthesis, as well as to the mismatch in ventricular shape. It is therefore recommendable to replace the high viscosity valve model by a fictitious domain valve leaflet with a fixed position, in order to achieve a more realistic valve geometry. Also the possibility to generate a more accurate computational mesh, featuring a smaller diameter aortic outflow tract, should be explored. With such an improved mesh, the shape of the ventricle throughout the cardiac cycle should be based on wall displacements obtained from

the experimental model. It is believed that a computational model, which is improved in the areas mentioned above, will enable the simulation of velocity fields as obtained by the DPIV measurements in the *in-vitro* setup.

Although the flow structures observed in the computations and in the experiments show similarities, this does not necessarily mean that these flow patterns are true-to-life. Physiological Reynolds numbers are not reached computationally nor has quantitative experimental data been obtained under physiological flow conditions. Also, the geometry of the ventricular cavity is stylistic. The inner surface of the natural ventricular wall has trabecular structures at the surface which may be influential to the flow patterns at low pressures. Furthermore, the papillary muscles have a substantial volume and are likely to interfere with the ventricular flow. Therefore, a validation of the computational method with clinically obtained velocity fields is not relevant at this stage, but the stylistic geometry does attribute to the process of understanding ventricular flow patterns.

6.2 Conclusions

From the results presented in this work, the following conclusions can be made;

- Mitral valve orientation largely influences the three dimensional ventricular flow patterns, as shown using both a computational and an experimental model (Chapter 2).
- The fictitious domain method is a suitable method for analyzing time dependent motion of structures in a pulsatile fluid flow, such as mechanical valve prostheses (Chapter 3).
- Pressure loading of a stiff valve leaflet using a fictitious domain method is possible if the fluid-structure interaction interface of the closed valve coincides with an edge of fluid elements (Chapter 4).
- The influence of variations in the Strouhal number on valve regurgitation is larger than that of variations in the Reynolds number (Chapter 4).
- Valve regurgitation in a 2D ventricle with two moving valves is influenced by the mutual configuration of the valves, as well as by the flow conditions that they are subjected to (Chapters 4 and 5).
- In the 2D ventricle model with two valves, the motion of the valves and the associated regurgitant volumes did not become periodical for any of the 9 flow pulses applied. Moreover, the cycle-to-cycle variation in valve motion and regurgitation is affected both by the flow conditions and valve orientation (Chapters 4 and 5).
- To apply the fictitious domain method to compliant systems, or to apply a pressure gradient to drive fluid and valve motion, the implementation of the fictitious domain method used in this work should be adapted such that coupling between valve and wall displacement is not taken into account.

Based on the above conclusions, the following is expected:

- As mitral valve orientation influences ventricular flow patterns, the interaction of the leaflets of the valve with the surrounding fluid is also influenced. The motion of either one of the two ventricular valves will influence the motion of the other valve. Therefore, it is to be expected that the efficiency of the ventricle as a pump depends on the orientation of implantation of a mitral valve prosthesis. Similarly, the orientation of an aortic valve prosthesis with respect to the aortic sinuses may influence the motion of the valve leaflets, which in turn can influence ventricular pump function.

- Decreasing the maximum opening angle of a prosthetic valve will increase the entrainment of the valve in back-flow, aiding early valve closure and reducing the amount of valve regurgitation. It will also cause more disturbance to the main flow, increasing the trans-valvular pressure drop which may affect the flow rate in a negative sense. There is probably an optimum maximum opening angle to be found, which may be depending on the implantation orientation.

- The orientation of a valve with respect to the heart affects the fluid velocity field. As a result, the closure velocity of the valve can be affected, due to which the loading of the prosthesis at valve closure would be changed. This might be important in the designing process of valve prostheses, in determining the life of the valve.

In order to enable the prediction of pump efficiency related to prosthetic valve design and orientation, it is necessary that the current three dimensional model of left ventricular flow is extended in several areas. In order to increase the Reynolds number in the simulations to a physiologically relevant level the mesh density should be increased. More efficient solvers will be necessary to decrease the computational time required for such simulations. Parallellization of the computational code is likely to reduce the computational time as well.

The fictitious domain method used in the two dimensional ventricle model with two valves should be applied to the three dimensional ventricular flow model to predict physiologically relevant pumping efficiencies for different flow conditions and valve orientations. Pressure loading of a rigid valve was possible when the fluid-structure interface on the closed valve coincided with an edge of the fluid elements. Pressure loading of flexible valves, such as the native heart valves and bioprosthetic valves, is expected to be possible if the fluid element edge that coincides with the fluid-structure interaction interface of the undeformed closed valve is displaced to follow the closed but deforming flexible leaflet. This will enable studies of interaction between native and prosthetic valves in a ventricle, which is interesting as single valve replacement is more common than double valve replacement. In the current model the stroke volume is prescribed. To really investigate the relation between valve design and orientation and ventricular efficiency, the heart wall must be included. Extenstion of the model with a model of the contractile ventricular wall (Kerckhoffs, 2003) replaces the need to prescribe the stroke volume and incorporates the action of

the cardiac muscle that depends on intra-ventricular pressure and ventricular volume. Consequently, cycle-to-cyle variations in the stroke volume can be included.

In order to make the computational model clinically applicable, detailed clinical input is needed with respect to exact three dimensional geometrical information on the ventricle wall, papillary muscles and perhaps even the trabecular structures, as well as deformation patterns. This information could be provided by ultrasound or MRI images of human ventricles. Furthermore, clinical measurements of ventricular flow patterns and valve motion should be provided for clinical validation of the computational method.

Bibliography

Baccani, B., Domenichini, F., and Pedrizzetti, G. (2003). Model and influence of mitral valve opening during the left ventricular filling. *Journal of Biomechanics*, **36**, 355–361.

de Hart, J., Peters, G. W. M., Schreurs, P. J. G., and Baaijens, F. P. T. (2003). A three-dimensional computational analysis of fluid-structure interaction in the aortic valve. *Journal of Biomechanics*, **36**, 103–112.

Kerckhoffs, R. C. P. (2003). *Depolarization wave and mechanics in the paced heart*. Ph-D thesis, Eindhoven University of Technology.

Lemmon, J. D. and Yoganathan, A. P. (2000). Three-dimensional computational model of left heart diastolic function with fluid-structure interaction. *Journal of Biomechanical Engineering*, **122**, 109–117.

Peskin, C. S. and McQueen, D. M. (1989). A three-dimensional computational method for blood flow in the heart: I. immersed elastic fibers in a viscous incompressible fluid. *Journal of Computational Physics*, **81**, 372–405.

Redaelli, A. and Montevecchi, F. M. (1996). Computational evaluation of intraventricular pressure gradients based on a fluid-structure approach. *Journal of Biomechanical Engineering, transactions of the ASME*, **118 (4)**, 529–537.

Saber, N. R., Gosman, A. D., Wood, N. B., Kilner, P. J., Charrier, C. L., and Firmin, D. N. (2001). Computational flow modeling of the left ventricle based on in vivo mri data: initial experience. *Annals of Biomedical Engineering*, **29**, 275–283.

Shortland, A. P., Black, R. A., Jarvis, J. C., Henry, F. S., Iudicello, I., Collins, M. W., and Salmons, S. (1996). Formation and travel of vortices in model ventricle: application to the design of skeletal muscle ventricles. *Journal of Biomechanics*, **29**, 503–511.

Taylor, T. W. and Yamaguchi, T. (1995). Realistic three-dimensional left ventricular ejection determined from computational fluid dynamics. *Med. Eng. Phys.*, **17 (8)**, 602–608.

Vierendeels, J. A., Riemslagh, K., Dick, E., and Verdonck, P. R. (2000). Computer simulation of intraventricular flow and pressure gradients during diastole. *Journal of Biomechanical Engineering*, **122**, 667–674.

Appendix A

Finite element formulation

A.1 Weighted residuals formulation

Consider a fluid domain Ω_f in which a solid domain Ω_s is immersed. The fluid and solid domain are coupled at boundary Γ_{fsi}, which is a part of the boundary of Ω_s The governing equations for the fluid-structure interaction problem read:

$$\rho\left(\frac{\partial \mathbf{v}_f}{\partial t} + \mathbf{v}_f \cdot \boldsymbol{\nabla}\mathbf{v}_f\right) = \boldsymbol{\nabla}\cdot\boldsymbol{\sigma}_f + \mathbf{f}^* \qquad in\ \Omega_f \qquad \text{(A.1)}$$

$$\boldsymbol{\nabla}\cdot\mathbf{v}_f = 0 \qquad in\ \Omega_f \qquad \text{(A.2)}$$

$$\boldsymbol{\nabla}\cdot\boldsymbol{\sigma_s} = 0 \qquad in\ \Omega_s \qquad \text{(A.3)}$$

$$det(\mathbf{F}) = 1 \qquad in\ \Omega_s \qquad \text{(A.4)}$$

$$\mathbf{v}_f = \mathbf{v}_s \qquad on\ \Gamma_i \qquad \text{(A.5)}$$

The weighted residuals method (Cuvelier *et al.*, 1986) is used to obtain approximations of the velocity and pressure fields in both the fluid and solid domain. The so-called weak form of the governing equations reads:

$$\int_{\Omega_f} \rho\mathbf{w}_f \cdot \left(\frac{\partial \mathbf{v}_f}{\partial t} + \mathbf{v}_f \cdot \boldsymbol{\nabla}\mathbf{v}_f\right) - \mathbf{w}_f \cdot \boldsymbol{\nabla}\cdot\boldsymbol{\sigma}_f\, d\Omega_f = \int_{\Omega_f} \mathbf{w}_f \cdot \mathbf{f}^*\, d\Omega_f in\ \Omega_f \qquad \text{(A.6)}$$

$$\int_{\Omega_f} q_f(\boldsymbol{\nabla}\cdot\mathbf{v}_f)d\Omega_f = \mathbf{0} \qquad in\ \Omega_f \qquad \text{(A.7)}$$

$$\int_{\Omega_s} \mathbf{w}_s \cdot (\boldsymbol{\nabla}\cdot\boldsymbol{\sigma}_s)d\Omega_s = \mathbf{0} \qquad \text{(A.8)}$$

$$\int_{\Omega_s} q_s(det(\mathbf{F}-1)\, d\Omega_s = 0 \qquad in\ \Omega_s \qquad \text{(A.9)}$$

$$\int_{\Gamma_i} \mathbf{w}_i \cdot (\mathbf{v}_f - \mathbf{v}_s)\, d\Gamma_i = 0 \qquad on\ \Gamma_i \qquad \text{(A.10)}$$

The product rule is applied to the stress terms in equations (A.6) and (A.8) which, making use of the symmetry of $\boldsymbol{\sigma}$, yields:

$$\int_\Omega \mathbf{w} \cdot \boldsymbol{\nabla} \cdot \boldsymbol{\sigma}\, d\Omega = \int_\Omega (\boldsymbol{\nabla} \cdot \boldsymbol{\sigma}) \cdot \mathbf{w}\, d\Omega = \int_\Omega \boldsymbol{\nabla} \cdot (\boldsymbol{\sigma} \cdot \mathbf{w})\, d\Omega - \int_\Omega (\boldsymbol{\nabla}\mathbf{w})^T : \boldsymbol{\sigma}\, d\Omega \qquad \text{(A.11)}$$

Next, the divergence theorem is applied to the first term of the righthandside of equation (A.11):

$$\int_\Omega \boldsymbol{\nabla} \cdot (\boldsymbol{\sigma} \cdot \mathbf{w})\, d\Omega = \int_\gamma (\boldsymbol{\sigma} \cdot \mathbf{n}) \cdot \mathbf{w}\, d\gamma \qquad \text{(A.12)}$$

Writing $\boldsymbol{\sigma} \cdot \mathbf{n} = \mathbf{t}$, the weak formulations of the governing equations become:

$$\int_{\Omega_f} \rho \mathbf{w}_f \cdot \left(\frac{\partial \mathbf{v}_f}{\partial t} + \mathbf{v}_f \cdot \boldsymbol{\nabla}\mathbf{v}_f \right) + (\boldsymbol{\nabla}\mathbf{w}_f)^T : \boldsymbol{\sigma}_f\, d\Omega_f = \int_{\gamma_f} \mathbf{w}_f \cdot \mathbf{t}_f\, d\gamma_f + \int_{\Omega_f} \mathbf{w}_f \cdot \mathbf{f}^*\, d\Omega_f \qquad in\ \Omega_f \qquad \text{(A.13)}$$

$$\int_{\Omega_f} q_f (\boldsymbol{\nabla} \cdot \mathbf{v}_f) d\Omega_f = \mathbf{0} \qquad in\ \Omega_f \qquad \text{(A.14)}$$

$$\int_{\Omega_s} (\boldsymbol{\nabla}\mathbf{w}_s)^T : \boldsymbol{\sigma}_s\, d\Omega_s = \int_{\gamma_s} \mathbf{w}_s \cdot \mathbf{t}_s\, d\gamma_s \qquad in\ \Omega_s \qquad \text{(A.15)}$$

$$\int_{\Omega_s} q_s (det(\mathbf{F} - 1)\, d\Omega_s = 0 \qquad in\ \Omega_s \qquad \text{(A.16)}$$

$$\int_{\Gamma_i} \mathbf{w}_i \cdot (\mathbf{v}_f - \mathbf{v}_s)\, d\Gamma_i = 0 \qquad on\ \Gamma_i \qquad \text{(A.17)}$$

The fluid structure interaction requires the coupling of fluid and solid velocity on the interaction boundary Γ_i, as well as the equilibrium of forces between the solid and the fluid. The force exerted on the solid by the fluid can be appointed in the boundary integral $\int_{\gamma_s} \mathbf{w}_s \cdot \mathbf{t}_s\, d\gamma_s$ in (equation A.15), since the fluid-structure interface Γ_i is a part of the boundary γ_s of the solid domain Ω_s. The force exerted on the fluid by the solid is appointed as a body force. Consider $\mathbf{f}$ a body force in the entire fluid domain Ω_f, then the force exerted on the fluid by the solid on the interface Γ_i can be written as:

$$\mathbf{f}^* = \mathbf{f} \cdot \delta(\mathbf{x} - \mathbf{x}_i) \qquad \text{(A.18)}$$

with δ the Dirac delta-function and neglecting any body forces other than the interaction force of the solid on the fluid. In this way, the body force $\mathbf{f}^*$ only has a value unequal to zero at the fluid-structure interaction interface Γ_i. Using the property of the delta function, the weak formulation of equation A.18 reads:

$$\int_{\Omega_f} \mathbf{w}_f \cdot \mathbf{f} \cdot \delta(\mathbf{x} - \mathbf{x}_i) d\Omega_f = \int_{\Gamma_i} \mathbf{w}_f \cdot \mathbf{f}\, d\Gamma_i \tag{A.19}$$

Equilibrium of forces on the fluid-structure interaction interface Γ_i then requires that the boundary integrals in equations (A.19) and (A.15) are equal, e.g.:

$$\int_{\Gamma_i} \mathbf{w}_s \cdot \mathbf{t}_s \; d\Gamma_i = \int_{\Gamma_i} \mathbf{w}_f \cdot \mathbf{f}\, d\Gamma_i \tag{A.20}$$

A.2 Linearization

The set of equations described in (A.13) to (A.17) is non-linear, requiring linearization and an iterative procedure to obtain an approximation of the solution. The balance equation for the fluid is non-linear due to the convection part, whereas the balance equation for the structure is non-linear with respect to the unknown current position field $\mathbf{x}_s$. This affects all the variables which are functions of the current position of the changing domain Ω_s, such as the stress tensor $\boldsymbol{\sigma}_s$ and the gradient operator $\boldsymbol{\nabla}$ which is taken with respect to the current configuration.

A.2.1 Fluid equations

Time discretization of the time-derivative of the fluid velocity in equation (A.13) is applied, using an implicit backward Euler scheme. The time-derivative of the fluid velocity in the time interval $t^n \rightarrow t^{n+1}$ is approximated by:

$$\frac{\partial \mathbf{v}_f}{\partial t} \approx \frac{\mathbf{v}_f - \mathbf{v}_f^n}{\Delta\, t} \tag{A.21}$$

with $\mathbf{v}_f = \mathbf{v}_f^{n+1}$. Next, linearization of the convective term is performed using Newton's method. Let $\mathbf{v}_f$ be the solution of (A.13), the solution is approximated by the sum of its estimation $\hat{\mathbf{v}}_f$ and its error $\delta\mathbf{v}_f$ according to:

$$\mathbf{v}_f = \hat{\mathbf{v}}_f + \boldsymbol{\delta}\mathbf{v}_f \tag{A.22}$$

Substituting expression (A.22) in the convective term of equation(A.13) yields:

$$(\hat{\mathbf{v}}_f + \delta\mathbf{v}_f) \cdot \boldsymbol{\nabla}(\hat{\mathbf{v}}_f + \delta\mathbf{v}_f) = \hat{\mathbf{v}}_f \cdot \boldsymbol{\nabla}\hat{\mathbf{v}}_f + \hat{\mathbf{v}}_f \cdot \boldsymbol{\nabla}\delta\mathbf{v}_f + \delta\mathbf{v}_f \cdot \boldsymbol{\nabla}\hat{\mathbf{v}}_f + \mathcal{O}(\delta^2) \tag{A.23}$$

Applying equations (A.21) and (A.23) to (A.13), while writing the stress tensor $\boldsymbol{\sigma}_s$ and the body force $\mathbf{f}$ in terms of their estimates and errors, reads:

$$\int_{\Omega_f} \rho \mathbf{w}_f \cdot \left(\frac{\hat{\mathbf{v}}_f + \delta\mathbf{v}_f - \mathbf{v}_f^n}{\Delta\, t} + \hat{\mathbf{v}}_f \cdot \boldsymbol{\nabla}\hat{\mathbf{v}}_f + \hat{\mathbf{v}}_f \cdot \boldsymbol{\nabla}\delta\mathbf{v}_f + \delta\mathbf{v}_f \cdot \boldsymbol{\nabla}\hat{\mathbf{v}}_f \right)\, d\Omega_f +$$
$$\int_{\Omega_f} (\boldsymbol{\nabla}\mathbf{w}_f)^T : (\hat{\boldsymbol{\sigma}}_f + \delta\boldsymbol{\sigma}_f) = \int_{\gamma_f} \mathbf{w}_f \cdot \mathbf{t}_f\, d\gamma_f + \int_{\Gamma_i} \mathbf{w}_f \cdot (\hat{\mathbf{f}} + \delta\mathbf{f})\, d\Gamma_i \qquad in\, \Omega_f \tag{A.24}$$

Reorganizing and substituting $\delta\boldsymbol{\sigma}_f = -\delta p_f \mathbf{I} + \delta\boldsymbol{\tau}_f$, the linearized weak form of the governing equations for the fluid read:

$$\int_{\Omega_f} \rho \mathbf{w}_f \cdot \left(\frac{\delta\mathbf{v}_f}{\Delta\, t} + \hat{\mathbf{v}}_f \cdot \boldsymbol{\nabla}\delta\mathbf{v}_f + \delta\mathbf{v}_f \cdot \boldsymbol{\nabla}\hat{\mathbf{v}}_f \right)\, d\Omega_f + \int_{\Omega_f} (\boldsymbol{\nabla}\mathbf{w}_f)^T : \delta\boldsymbol{\tau}_f\, d\Omega_f -$$
$$\int_{\Omega_f} (\boldsymbol{\nabla} \cdot \mathbf{w}_f) \delta p_f\, d\Omega_f - \int_{\Gamma_i} \mathbf{w}_f \cdot \delta\mathbf{f}\, d\Gamma_i =$$
$$\int_{\gamma_f} \mathbf{w}_f \cdot \mathbf{t}_f\, d\gamma_f + \int_{\Gamma_i} \mathbf{w}_f \cdot \hat{\mathbf{f}}\, d\Gamma_i - \int_{\Omega_f} \mathbf{w}_f \cdot \mathbf{r}_f\, d\Omega_f \tag{A.25}$$

$$\int_{\Omega_f} \mathbf{q}_f (\boldsymbol{\nabla} \cdot \delta\mathbf{v}_f)\, d\Omega_f = -\int_{\Omega_f} \mathbf{q}_f (\boldsymbol{\nabla} \cdot \mathbf{v}_f)\, d\Omega_f \tag{A.26}$$

with

$$\int_{\Omega_f} \mathbf{w}_f \cdot \mathbf{r}_f\, d\Omega_f = \int_{\Omega_f} \rho \mathbf{w}_f \cdot \left(\frac{\hat{\mathbf{v}}_f - \mathbf{v}^n}{\Delta\, t} + \hat{\mathbf{v}}_f \cdot \boldsymbol{\nabla}\hat{\mathbf{v}}_f \right) - (\boldsymbol{\nabla}\mathbf{w}_f)^T : \hat{\boldsymbol{\sigma}}_f\, d\Omega_f \tag{A.27}$$

A.2.2 Structure equations

The integrals in equations (A.15 - A.16) are taken in the current (unknown) position. Evaluation of the integrals requires a transformation to a known configuration. The transformation can be made to two configurations. In the total Lagrange approach, the transformation is made to the undeformed configuration denoted by Ω_0, while in the updated Lagrange approach the transformation to the last converged configuration denoted by Ω_n is made. In this work the updated Lagrange approach is applied, which is represented schematically in figure A.2.2. The transformation from the initial configuration Ω_0 at time t_0 to the last known configuration Ω_n at time $t = t_n$ is given by $\mathbf{F}_n$, while the transformation from the last known configuration to the current (unknown) configuration Ω at $t = t_{n+1}$ is denoted by $\mathbf{F}_\Delta$. In this way the total deformation $\mathbf{F}$ is given by

$$\mathbf{F} = \mathbf{F}_n \cdot \mathbf{F}_\Delta, \quad \text{with} \quad \mathbf{F}_n = (\boldsymbol{\nabla}_0 \mathbf{x}_n)^T; \mathbf{F}_\Delta = (\boldsymbol{\nabla}_n \mathbf{x})^T. \tag{A.28}$$

where $\boldsymbol{\nabla}_0$ represents the gradient operator with respect to the initial configuration and $\boldsymbol{\nabla}_n$ the gradient operator with respect to the last known configuration. In absence of any boundary load other than the fluid-structure interaction load **f** and writing $\boldsymbol{\nabla} = \mathbf{F}_\Delta^{-T} \cdot \boldsymbol{\nabla}_n$, the balance equations for the structure read:

$$\int_{\Omega_{s,n}} (\boldsymbol{\nabla}_n \mathbf{w}_s)^T : \mathbf{F}_\Delta^{-1} \cdot \boldsymbol{\sigma}_s \; d\Omega_{s,n} = \int_{\gamma_{s,n}} \mathbf{w}_s \cdot \mathbf{f} \, d\gamma_{s,n} \tag{A.29}$$

$$\int_{\Omega_{s,n}} q_s (J-1)) \; d\Omega_{s,n} = \mathbf{0} \tag{A.30}$$

with $J = det(\mathbf{F})$.

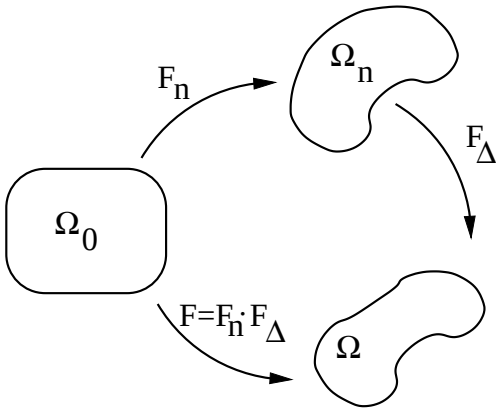

Figure A.1: Schematic representation of the configurations for the transformations in an updated Lagrange formulation.

Formally, the integral in $d\Omega$ is transformed into an integral in $J \; d\Omega_n$. Assuming incompressibility [1], $J = 1$ is substituted in equation (A.30). The non-linear equations (A.29-A.30) are solved using the Newton iteration process. To this end the solution **x** is approximated by the sum of its estimate $\hat{\mathbf{x}}$ and its error $\delta\mathbf{x}$. The other quantities are approximated in a similar way:

$$\boldsymbol{\sigma}_s = \hat{\boldsymbol{\sigma}}_s + \delta\boldsymbol{\sigma}_s; \mathbf{F}_\Delta = \hat{\mathbf{F}}_\Delta + \delta\mathbf{F}_\Delta; J = \hat{J} + \delta J; \mathbf{f} = \hat{\mathbf{f}} + \delta\mathbf{f} \tag{A.31}$$

Substitution in the balance equations (A.29,A.30) yields:

$$\int_{\Omega_{s,n}} (\boldsymbol{\nabla}_n \mathbf{w})^T : (\hat{\mathbf{F}}_\Delta + \delta\mathbf{F}_\Delta)^{-1} \cdot (\hat{\boldsymbol{\sigma}}_s + \delta\boldsymbol{\sigma}_s) \; d\Omega_{s,n} = \int_{\Gamma_i} \mathbf{w}_s \cdot (\hat{\mathbf{f}} + \delta\mathbf{f}) \; d\Gamma_i \tag{A.32}$$

[1] Note that this condition is not necessarily met during the iteration process. Using it here therefore introduces an approximation. However, since we use the same relation later to transform the linearized equation back to the current configuration, the equations to be solved remain correct, but a term is neglected in the linearization for the Newton process.

$$\int_{\Omega_{s,n}} \hat{J} + \delta J - 1 \; d\Omega_{s,n} = \mathbf{0} \tag{A.33}$$

The inverse of sum of the approximation of the deformation tensor and its error is elaborated as follows:

$$\begin{aligned}
(\hat{\mathbf{F}}_\Delta + \delta\mathbf{F}_\Delta)^{-1} &= \left(\hat{\mathbf{F}}_\Delta \cdot (\mathbf{I} + \hat{\mathbf{F}}_\Delta^{-1} \cdot \delta\mathbf{F}_\Delta)\right)^{-1} \\
&= (\mathbf{I} + \hat{\mathbf{F}}_\Delta^{-1} \cdot \delta\mathbf{F}_\Delta)^{-1} \cdot \hat{\mathbf{F}}_\Delta^{-1} \\
&\approx (\mathbf{I} - \hat{\mathbf{F}}_\Delta^{-1} \cdot \delta\mathbf{F}_\Delta) \cdot \hat{\mathbf{F}}_\Delta^{-1} \\
&= \hat{\mathbf{F}}_\Delta^{-1} - \hat{\mathbf{F}}_\Delta^{-1} \cdot \delta\mathbf{F}_\Delta \cdot \hat{\mathbf{F}}_\Delta^{-1} \\
&= \hat{\mathbf{F}}_\Delta^{-1} - \hat{\mathbf{F}}_\Delta^{-1} \cdot (\hat{\mathbf{F}}_\Delta^{-T} \cdot \delta\mathbf{F}_\Delta^{T})^{T} \\
&= \hat{\mathbf{F}}_\Delta^{-1} - \hat{\mathbf{F}}_\Delta^{-1} \cdot (\hat{\mathbf{F}}_\Delta^{-T} \cdot \boldsymbol{\nabla}_n \delta\mathbf{x})^{T} \\
&= \hat{\mathbf{F}}_\Delta^{-1} - \hat{\mathbf{F}}_\Delta^{-1} \cdot (\boldsymbol{\nabla}\delta\mathbf{x})^{T}
\end{aligned} \tag{A.34}$$

where for a sufficiently small $\delta\mathbf{F}_\Delta$, a Taylor expansion is allowed in the third line. Substituting in equation (A.32) yields:

$$\int_{\Omega_{s,n}} (\boldsymbol{\nabla}_n \mathbf{w}_s)^T : \left(\hat{\mathbf{F}}_\Delta^{-1} - \hat{\mathbf{F}}_\Delta^{-1} \cdot (\boldsymbol{\nabla}\delta\mathbf{x})^T\right) \cdot (\hat{\boldsymbol{\sigma}}_s + \delta\boldsymbol{\sigma}_s) \; d\Omega_{s,n} - \int_{\Gamma_i} \mathbf{w}_s \cdot \delta\mathbf{f} \; d\Gamma_i = \int_{\Gamma_i} \mathbf{w}_s \cdot \hat{\mathbf{f}} \; d\Gamma_i \tag{A.35}$$

Elaboration and neglecting higher order terms $(\delta \cdot \delta)$ yields:

$$\int_{\Omega_s} (\boldsymbol{\nabla}\mathbf{w}_s)^T : \left(\delta\boldsymbol{\sigma}_s - (\boldsymbol{\nabla}\delta\mathbf{x}_s)^T \cdot \hat{\boldsymbol{\sigma}}_s\right) \; d\Omega_s - \int_{\Gamma_i} \mathbf{w}_s \cdot \delta\mathbf{f} \; d\Gamma_i = \int_{\Omega_s/\Gamma_i} \mathbf{w}_s \cdot \mathbf{r}_s \; d\Omega_s/\Gamma_i \tag{A.36}$$

with

$$\int_{\Omega_s/\Gamma_i} \mathbf{w}_s \cdot \mathbf{r}_s \; d\Omega_s/\Gamma_i = \int_{\Gamma_i} \mathbf{w}_s \cdot \hat{\mathbf{f}} \; d\Gamma_i - \int_{\Omega_s} (\boldsymbol{\nabla}\mathbf{w}_s)^T : \hat{\boldsymbol{\sigma}}_s \; d\Omega_s \tag{A.37}$$

The continuity equation is linearized by writing $J = \hat{J} + \delta J$, with $\delta J = \hat{J}(\boldsymbol{\nabla} \cdot \delta\mathbf{x}_s)$ which is elaborated in equation (A.38)

$$
\begin{aligned}
J = det(\mathbf{F}) &= det(\hat{\mathbf{F}} + \delta\mathbf{F}) \\
&= det\left((\mathbf{I} + \delta\mathbf{F}\cdot\hat{\mathbf{F}}^{-1})\cdot\hat{\mathbf{F}}\right) \\
&= det\ (\mathbf{I} + \delta\mathbf{F}\cdot\hat{\mathbf{F}}^{-1})\ det\ (\hat{\mathbf{F}}) \\
&\approx \hat{J}\left(1 + tr(\delta\mathbf{F}\cdot\hat{\mathbf{F}}^{-1})\right) \\
&= \hat{J} + \hat{J}\ tr(\hat{\mathbf{F}}^{-T}\cdot\delta\mathbf{F}^{T})^{T} \\
&= \hat{J} + \hat{J}\ tr\left(\hat{\mathbf{F}}^{-T}\cdot\boldsymbol{\nabla}_0\delta\mathbf{x}_s\right)^{T} \\
&= \hat{J} + \hat{J}\ tr(\boldsymbol{\nabla}\delta\mathbf{x}_s)^{T} \\
&= \hat{J} + \hat{J}\ (\boldsymbol{\nabla}\cdot\delta\mathbf{x}_s) \qquad\qquad = \hat{J} + \delta J
\end{aligned}
\tag{A.38}
$$

Subsitution in equation (A.33) yields:

$$
\int_{\Omega_s} q_s\ \hat{J}(\boldsymbol{\nabla}\cdot\delta\mathbf{x}_s)\ d\Omega_s = -\int_{\Omega_s} q_s\ (\hat{J}-1)\ d\Omega_s \tag{A.39}
$$

Writing $\delta\boldsymbol{\sigma}_s = -\delta p\mathbf{I} + \delta\boldsymbol{\tau}_s$, the linearized weak form of the governing equations for the structure becomes:

$$
\begin{aligned}
&\int_{\Omega_s} (\boldsymbol{\nabla}\mathbf{w}_s)^T : \left(\delta\boldsymbol{\tau}_s - (\boldsymbol{\nabla}\delta\mathbf{x}_s)^T\cdot\hat{\boldsymbol{\sigma}}_s\right)\ d\Omega_s - \\
&\qquad\int_{\Omega_s} \delta p\boldsymbol{\nabla}\cdot\mathbf{w}_s\ d\Omega_s - \int_{\Gamma_i}\mathbf{w}_s\cdot\delta\mathbf{f}\ d\Gamma_i = \int_{\Omega_s/\Gamma_i}\mathbf{w}_s\cdot\mathbf{r}_s\ d\Omega_s/\Gamma_i
\end{aligned}
\tag{A.40}
$$

$$
\int_{\Omega_s} q_s\ (\boldsymbol{\nabla}\cdot\delta\mathbf{x}_s)\ d\Omega_s = -\int_{\Omega_s} q_s\ \frac{(\hat{J}-1)}{\hat{J}}\ d\Omega_s \tag{A.41}
$$

Solving the fluid and structure equations simultaneously, it is more convenient to consider structure velocities. To this end a first-order approximation is used according to: $\delta\mathbf{x}_s = \Delta t\ \delta\mathbf{v}_s$.

A.2.3 Coupling equation

Linearization of the equation coupling the fluid and solid velocity at interaction interface Γ_i (A.17) is straightforward, given by:

$$
\int_{\Gamma_i}\mathbf{w}_i\cdot(\delta\hat{\mathbf{v}}_f - \delta\hat{\mathbf{v}}_s)\ d\Gamma_i = -\int_{\Gamma_i}\mathbf{w}_i\cdot(\mathbf{v}_f - \mathbf{v}_s)\ d\Gamma_i \tag{A.42}
$$

A.3 Spatial discretization

Equations (A.25) to (A.27) and (A.40) to (A.42) are spatially discretized using the finite element method. In this method, the domains Ω_f, Ω_s and boundaries Γ_i,γ_s and γ_f are subdivided into non-overlapping subdomains, called elements, Ω_f^e,Ω_s^e,Γ_i^e,γ_f^e and γ_s^e. In each element the unknowns are defined in a number of nodal points. The unknowns $\delta\mathbf{v}_\alpha, \delta p_\alpha$ and $\delta\mathbf{f}_\alpha$ (α=f,s) at position $\mathbf{x}_\alpha$ in the corresponding domain or boundary at time t are approximated by $\delta\mathbf{v}_\alpha^h, \delta p_\alpha^h$ and $\delta\mathbf{f}_\alpha^h$ using interpolation functions based on the corresponding nodal values. The corresponding weighting functions $\mathbf{w}_\alpha, q_\alpha$ and $\mathbf{w}_i$ are discretized using the same interpolation functions (Galerkin). With respect to a Carthesian basis, the interpolation expressions read:

$$\delta\underset{\sim}{v}_\alpha(\underset{\sim}{x}_\alpha,t) = \sum_{i=1}^{N} \phi_\alpha^i(\underset{\sim}{x}_\alpha)\delta v_\alpha^i(t) = \underline{\Phi}_\alpha \delta\underset{\sim}{v}_\alpha^e \tag{A.43}$$

$$\delta p_\alpha(\underset{\sim}{x}_\alpha,t) = \sum_{i=1}^{M} \psi_\alpha^i(\underset{\sim}{x}_\alpha)\delta p_\alpha^i(t) = (\underset{\sim}{\Psi}_\alpha)^T \delta p_\alpha^e \tag{A.44}$$

$$\delta\underset{\sim}{f}(\underset{\sim}{x}_\alpha,t) = \sum_{i=1}^{L} \theta^i(\underset{\sim}{x}_\alpha)\delta\underset{\sim}{f}^i(t) = \underline{\Theta}\delta\underset{\sim}{f}^e \tag{A.45}$$

with N, M and L the number of nodal points for the velocity, pressure and interaction forces respectively. The weighting functions are discretized in a similar fashion as shown in equations (A.43) to (A.45). With respect to the gradient operators $\boldsymbol{\nabla}$ working on $\delta\mathbf{v}_\alpha$, the operator $\mathbf{B}$ is introduced which incorporates the derivatives of the interpolation functions:

$$\boldsymbol{\nabla}\delta\mathbf{v}_\alpha = \mathbf{B}\delta\mathbf{v}_\alpha \quad \rightarrow \quad \underline{B}\delta\underset{\sim}{v}_\alpha^e \tag{A.46}$$

Applying expressions (A.43) to (A.46) to the linearized weak form of the governing equations (A.25) to (A.27) leads to the discretized matrix-vector form of the governing equations:

$$\underset{\sim}{w}_f^{e\,T}(\underline{M}_f + \underline{N}_f + \underline{K}_f)\delta\underset{\sim}{v}_f^e + \underset{\sim}{w}_f^{e\,T}\underline{L}_f^T\delta\underset{\sim}{p}_f^e + \underset{\sim}{w}_f^{e\,T}\underline{C}_f^T\delta\underset{\sim}{f}_f^e = \underset{\sim}{w}_f^{e\,T}\underset{\sim}{r}_f \tag{A.47}$$

$$\underset{\sim}{q}_f^{e\,T}\underline{L}_f\delta\underset{\sim}{v}_f^e = -\underset{\sim}{q}_f^{e\,T}\underline{L}_f\underset{\sim}{v}_f^e \tag{A.48}$$

$$\underset{\sim}{w}_s^{e\,T}\Delta t\,\underline{K}_s\,\delta\underset{\sim}{v}_s^e + \underset{\sim}{w}_s^{e\,T}\underline{L}_s^T\delta\underset{\sim}{p}_s^e + \underset{\sim}{w}_s^{e\,T}\underline{C}_s^T\delta\underset{\sim}{f}_s^e = \underset{\sim}{w}_s^{e\,T}\underset{\sim}{r}_s \tag{A.49}$$

$$\underset{\sim}{q}_s^{e\,T}\Delta t\underline{L}_s\delta\underset{\sim}{v}_s^e = \underset{\sim}{q}_s^{e\,T}(\underset{\sim}{\Psi})^T(\frac{\hat{J}-1}{\hat{J}}) \tag{A.50}$$

$$\underset{\sim}{w}_i^{e\,T}(\underline{C}_f\delta\underset{\sim}{v}_f^e + \underline{C}_s\delta\underset{\sim}{v}_f^e) = -\underset{\sim}{w}_i^{e\,T}(\underline{C}_f\hat{\underset{\sim}{v}}_f^e + \underline{C}_s\hat{\underset{\sim}{v}}_f^e) \tag{A.51}$$

where $\underline{M}_f$ represents the fluid mass matrix, $\underline{N}_f$ is the convection matrix, $\underline{K}_f$ the diffusion matrix, $\underline{L}_f$ the divergence matrix, $\underline{C}_f$ the coupling matrix and $\underset{\sim}{f}^v_f$ the righthand-side column, which read:

$$\underline{M}_f = \int_{\Omega^e_f} \frac{\rho_f}{\Delta t} \underline{\Phi}^T_f \underline{\Phi}_f \; d\Omega^e_f; \quad \underline{N}^e_f = \int_{\Omega^e_f} \rho_f \underline{\Phi}^T_f (\hat{\underset{\sim}{v}}_f \underline{B}_f + \underline{B}_f \hat{\underset{\sim}{v}}^e_f) \; d\Omega^e_f; \tag{A.52}$$

$$\underline{K}_f = \int_{\Omega^e_f} \underline{B}^T_f \underline{D}_f \underline{B}_f \; d\Omega^e_f; \quad \underline{L}^T_f = -\int_{\Omega^e_f} \underline{B}^T_f \underline{I}\underset{\sim}{\Psi}^T_f \; d\Omega^e_f; \tag{A.53}$$

$$\begin{aligned} \underline{C}^T_f &= \int_{\Gamma^e_i} \underline{\Phi}^T_f \underline{\Theta} \; d\Gamma^e_i; \\ \underset{\sim}{f}^v_f &= \int_{\gamma^e_f} \underline{\Phi}^T_f \underset{\sim}{t}_f \; d\gamma^e_f + \int \Gamma^e_i \underline{\Phi}^t_f \underline{\Theta}^e \underset{\sim}{f}^e - \int \Omega^e_f \underline{\Phi}^t_f \underset{\sim}{r}_f \; d\Omega^e_f \end{aligned} \tag{A.54}$$

The matrices and columns for the structure equations are elaborated as:

$$\underline{L}^T_s = -\int_{\Omega^e_s} \underline{B}^T_s \underline{I}\underset{\sim}{\Psi}^T_s \; d\Omega^e_s; \quad \underline{K}_s = \int_{\Omega^e_s} \underline{B}^T_s (\underline{D}_s + \hat{\underline{D}}_s) \underline{B}_s \; d\Omega^e_s; \tag{A.55}$$

$$\underline{C}^T_s = \int_{\Gamma^e_i} \underline{\Phi}^T_s \underline{\Theta} \; d\Gamma^e_i; \qquad \underset{\sim}{f}^e_s = \int_{\Omega^e_s/\Gamma^e_i} \underline{\Phi}^T_s \underset{\sim}{r}_s \; d\Omega^e_s/\Gamma^e_i \tag{A.56}$$

The contribution of the Cauchy stress associated with the last known configuration is incorporated in matrix $\hat{\underline{D}}_s$. The matrix-column notation of the integral $\int_{\Omega_s} (\boldsymbol{\nabla}\mathbf{w})^T : (\boldsymbol{\nabla}\delta\mathbf{x}_s)^T \cdot \hat{\boldsymbol{\sigma}}_s \; d\Omega_s$ in equation (A.40) would result in $\underset{\sim}{w}_s \underline{B}^T_s \underline{B}_s \delta\underset{\sim}{x}_s \hat{\underline{\Sigma}}_s$. This matrix-column notation is rewritten to $\underset{\sim}{w}_s \underline{B}^T_s \hat{\underline{D}}_s \underline{B}_s \delta\underset{\sim}{x}_s$ such that $\hat{D}_s$ incorporates the components of $\hat{\Sigma}_s$ but in a different order such that the products in the tensor notation still hold. This is elaborated in Appendix A of van Oijen (2003).
Equations (A.47) to (A.51) must hold for all admissible weighting functions, these equations can be assembled over all elements which results in:

$$\begin{pmatrix} \begin{bmatrix} \underline{K}^*_f & \underline{L}^T_f \\ \underline{L}_f & \underline{0} \end{bmatrix} & \begin{bmatrix} \\ \underline{0} \\ \\ \end{bmatrix} & \begin{bmatrix} \underline{C}^T_f \\ \underline{0} \end{bmatrix} \\ \begin{bmatrix} \\ \underline{0} \\ \\ \end{bmatrix} & \begin{bmatrix} \underline{K}^*_s & \underline{L}^T_s \\ \underline{L}_s & \underline{0} \end{bmatrix} & \begin{bmatrix} \underline{C}^T_s \\ \underline{0} \end{bmatrix} \\ \begin{bmatrix} \underline{C}_f & \underline{0} \end{bmatrix} & \begin{bmatrix} \underline{C}_s & \underline{0} \end{bmatrix} & \begin{bmatrix} \underline{0} \end{bmatrix} \end{pmatrix} \cdot \begin{pmatrix} \delta\underset{\sim}{v}_f \\ \delta\underset{\sim}{p}_f \\ \delta\underset{\sim}{v}_s \\ \delta\underset{\sim}{p}_s \\ \delta\underset{\sim}{f}_c \end{pmatrix} = \begin{pmatrix} \underset{\sim}{f}^v_f \\ \underset{\sim}{f}^p_f \\ \underset{\sim}{f}^v_s \\ \underset{\sim}{f}^p_s \\ \underset{\sim}{f}_c \end{pmatrix} \tag{A.57}$$

with $\underline{K}^*_f = \underline{M}_f + \underline{N}_f + \underline{K}_f$, $\underline{K}^*_s = \Delta t \underline{K}_s$ and $\underline{L}^*_s = \Delta t \underline{L}_s$. It is straightforward to see from equations (A.48) and (A.50) that the righthandside vectors belonging to the

pressure degrees of freedom are given by $\underset{\sim}{f}^p_f = -\underline{L}_f \underset{\sim}{v}_f$ for the fluid and $\underset{\sim}{f}^p_s = (\underset{\sim}{\Psi})^T \frac{\dot{J}-1}{\dot{J}}$ for the structure. Similarly, the righthandside column for the fluid-structure velocity coupling equation (A.51) reads $\underset{\sim}{f}_i = -(\underline{C}_f \underset{\sim}{\hat{v}}_f + \underline{C}_s \underset{\sim}{\hat{v}}_s)$.

Bibliography

Cuvelier, C., Segal, A., and van Steenhoven, A. (1986). *Finite element methods and Navier-Stokes equations*. D. Reidel Publishing Company.

van Oijen, C. H. G. A. (2003). *Mechanics and design of fiber-reinforced vascular prostheses*. Ph-D thesis, Eindhoven University of Technology.